8-28-2012

Viscous flow past plates

Xu Ling

Xu, Ling

Candidate

Mathematics and Statistics

Department

This dissertation is approved, and it is acceptable in quality and form for publication:

Approved by the Dissertation Committee:

Nitsche, Monika , Chairperson

Sulsky, Deborah

Lau, Stephen

Vorobieff, Peter

Viscous Flow Past Plates

BY

Ling Xu

B.S., Applied Mathematics, Xiamen University, 2006
M.S., Applied Mathematics, University of New Mexico, 2008

DISSERTATION

Submitted in Partial Fulfillment of the
Requirements for the Degree of
Doctor of Philosophy
Mathematics

The University of New Mexico
Albuquerque, New Mexico
July, 2012

Acknowledgments

I would like to express my sincerest gratitude to my advisor Professor Monika Nitsche for her excellent guidance, support and motivation over the past four years, and for her extraordinary patience to read different versions of my dissertation. She has shared with me an unique perspective in the world of computational fluid dynamics.

I would also like to thank Professors Deborah Sulsky, Peter Vorobieff, and Stephen Lau for serving as members in my dissertation committee. In particular, I wish to thank Professors Deborah Sulsky and Howard Schreyer, for their guidance and caring. Further more, thanks to Professors Stephen Lau, Robert Krasny and Hans Johnston for their helpful suggestions.

To my husband Lang Zhou, thanks for his continued encouragement. He is always there standing by me through the good times and bad.

The work used partly the Extreme Science and Engineering Discovery Environment (XSEDE), which is supported by National Science Foundation grant number OCI-1053575, and systems at the UNM Center for Advanced Research Computing.

Viscous Flow Past Plates

by

Ling Xu

B. S. , Applied Mathematics, Xiamen University, 2006
M. S. , Applied Mathematics, University of New Mexico, 2008
Ph. D. , Mathematics, University of New Mexico, 2012

ABSTRACT

I devise a numerical method of high order in space (FDMHS) to simulate flow past a finite plate and a semi-infinite plate. The method solves the incompressible Navier-Stokes equation in the stream function-vorticity formulation. The focus is to study a fundamental problem in fluid dynamics, namely, flow past sharp edges. Resolving this flow structure is difficult, in particular at early times. The difficulty is due to the fact that large velocity gradients and vorticity are present in a very thin boundary layer attached to the plate initially. FDMHS is a splitting method, implicit in time and uses compact fourth order finite differences. FDMHS has demonstrated satisfactory performance in our numerical simulations.

For the finite plate case, three background flow are used: impulsively started, uniformly accelerated, and oscillating. Resolved computations show structure of the boundary layer separation and roll-up from very early times to relative large times. For the impulsively started, the details of vorticity structure at early times have been studied. We resolved the region of negative vorticity along the plate induced by and entrained into the leading vortex. A secondary entrainment of positive vorticity into the region of negative vorticity is also found. The maximum velocity decays as $t^{-1/4}$ over a large initial time interval. For the uniformly accelerated, we show evolution in the appropriate non-dimensional variables, and find agreement with scaling laws observed in experiments. For the oscillating, we compared the viscous simulation using FDMHS with an inviscid vortex sheet method. Both are in excellent agreement at early times. There are difference at later times most likely caused by wall vorticity which is not accounted for by the vortex sheet model. The shed circulation is independent of viscosity initially for all three background flows. The effect of viscosity on the vorticity evolution and on quantities such as the shed circulation, core trajectory and vorticity, vortex size and

width are also presented. For the semi-infinite plate case, we derived the scaling rule and verified it numerically.

Contents

List of Figures

List of Tables

1 Introduction

Viscous fluid flow past a bluff body is a fundamental problem that has been studied for more than ten decades, following Prandtl's (1904) experiments. In his work, Prandtl introduced the concept of a boundary layer, which is a layer of fluid in the immediate vicinity of a wall in which the effect of viscosity is significant. Because of viscosity, the fluid velocity equals the wall velocity at the boundary, while it approaches the far field velocity $\mathbf{U}_{\max}$ in a finite distance from the wall. This finite distance is the boundary layer thickness δ, and it depends on viscosity ν and time t in the form of $\delta \sim \sqrt{\nu t}$. For steady walls, velocity gradients in the boundary layer, and thus the vorticity, are proportional to $\mathbf{U}_{\max}/\sqrt{\nu t}$, and are especially large at early times when t is small. The boundary layer separates in regions of large curvature, or at corners, and rolls up forming a vortex, often referred to as the starting vortex. The starting vortex is important in many applications. For example, it is associated with the lift force that insects gain by flapping wings; with the force that acts on pillars in a wavy viscous flow and with air swirls that form around buildings exposed to large winds. Investigating the detailed structure and evolution of the starting vortex helps understand this fundamental phenomenon.

My thesis focuses on boundary layer separation at the sharp edges of plates of zero thickness. Vortex separation at edges is ubiquitous and has been the focus of several experimental and numerical studies. The experimental studies most closely related to this work are the following. Pierce [34] visualized flow past finite plates and studied the effect of varying plate profiles. Taneda and Honji [44] varied the background flow and found a scaling rule relating viscosity, time and vortex size. Pullin and Perry [36] considered flow past wedges. Lian and Huang [28] obtained data on the shed circulation. In all these experimental visualizations, one can see that the boundary layer separates at the sharp edge and rolls up, forming a spiral vortex. In many cases, the outer turn of the vortex spiral is observed to become unstable and breaks up into a group of secondary vortices. Careful direct numerical simulations of flow past bluff bodies have been performed by several researchers. For example, Wang [50] used a fourth order finite difference scheme to simulate flow past an elliptical wing undergoing heaving and pitching motion. Wang, Liu and Childress [47] studied the flow past an ellipse. Several other authors have used body-fitted grids or vortex particle methods to resolve flow past moving objects [49, 3, 10, 20]. These flows are more complex than the one of interest here, and the simulations are not focused on the detail we are looking for. The works most closely related to ours are Koumoutsakos and Shields [23] (hereafter referred as KS) and Luchini and Tognaccini [29] (hereafter referred as LT). KS used a particle method to resolve flow past a finite plate normal to the flow. he computed the

separated, rolled up shear layer at large times, computed the drag coefficient and recorded some large scale quantities. Flow past a zero thickness plate is difficult to compute, and KS was one of the first times that successfully implemented a particle method reproducing viscous diffusion between particles and viscous generation of vorticity at walls. LT considered flow past a semi-infinite plate of zero thickness. They used a finite difference method on a mesh growing self-similarly with the flow. This technique make it possible to compute the flow to relatively large times.

However, these earlier works focus on large scales of the flow dynamics. Not much detailed information is given, in particular at the early times of the formation process in which velocity gradients and vorticity near the wall are large. Much remains to be understood. The goal of my work is to use high resolution simulations of the Navier Stokes equations to better understand details of the vorticity dynamics, and details of characteristic properties of the flow, such as vortex core trajectory and vorticity, vortex size, shed circulation and circulation shedding rate. We also want to document the flow dependence on the fluid viscosity. This work is partly motivated by vortex sheet simulations of vortex separation. Inviscid vortex sheet and point vortex models have been used widely to simulate separation because of their simplicity and significant computational efficiency [6, 12, 30, 48, 19, 41, 40, 2]. Comparison with either experiments or viscous simulations show that they recover large scale aspects of the viscous flow surprisingly well [12, 37, 49, 46]. Nitsche and Krasny [31], however, performed vortex sheet simulations of axisymmetric shear layer separation and compared their results with laboratory experiments. They observed a discrepancy in the circulation shedding rate at early times which led to a 10% increase in the total shed circulation. They attributed this discrepancy to the effect of viscosity at early times, in which the model's assumption that a shear layer separates tangentially from the edge does not hold. The work in this thesis on planar separation will help elucidate details of the starting formation process and its dependence on viscosity, and this, in turn, may lead to improved separation models.

I will consider both oncoming flow past a finite plate normal to the flow, and flow past a semi-infinite plate. The finite plate problem is more physically relevant and more readily studied in laboratory experiments. Here we consider three types of background flows: impulsively started, uniformly accelerated and oscillatory motion. All these types of flows are important. The impulsive start mimics scenarios in which forces act suddenly on an object with often destructive consequences. Accelerated flows are easiest to reproduce, and the dependence of the solution on different power law behavior is of interest. Oscillatory flows occur commonly in biological systems such as swimming fish. Numerically, the finite plate has the advantage that the area containing the vorticity is finite and the flow can be captured in a finite computational domain. Semi-infinite case is of interest because a

scaling rule exists which relates the length scale, time and viscosity. According to the scaling rule, the solution of flow at one viscosity could be obtained, by a scale, from the results at any other viscosities. Therefore, computation at one viscosity is all that are needed. However, the semi-infinite case is numerically more difficult because the support of fluid vorticity is infinite. LT used an exponential decay function to approximate the incoming vorticity. They also observed instabilities in their solutions and it is not clear whether possibly inaccurate modelling of the infinite boundary layer can cause these instabilities.

Computing the impulsively started flow past plates is difficult for several reasons. The initial flow is singular at the tip with unbounded maximum velocities. The boundary layer is thin at an early time stage ($t << 1$) or for a large Reynolds number ($\nu << 1$). Large velocity gradients and large vorticity that are present in this thin layer would easily lead to numerical instability. The computational geometry is not trivial as well since the domain containing the fluid has a slit due to the presence of the plate. For the semi-infinite plate case, the physical domain is infinite. LT's method is very domain-specific and only applies to the semi-similar flow (e.g. the flow past a semi-infinite plate). The vortex particle methods used by KS is relatively low order, and does not reveal many details the flow dynamics at early times. I chose to develop a fourth order finite difference method, referred to as FDMHS (Finite Difference Method of High order in Space), to compute planar flow past edges. Following the work of E & Liu, the method uses compact finite differences and the Thomas formula to obtain vorticity at wall. It is a split method that treats convection using a semi-Lagrangian method and diffusion using an implicitly high order Crank-Nicolson method. These components were found to be necessary to avoid numerical instabilities and resolve the flow, particularly at the early times, of unbounded maximum velocities and very small length scales. FDMHS is implemented in parallel using the MPI interface, and its parallel performance shows to be quite efficient.

To validate the method we compare results with E & Liu for driven cavity flows and found equally well performance to their method, and better performance than a standard second order method. We tested order of convergence for driven cavity and found fourth order in space, first order in time. For the much more singular case of impulsively started flow past a finite plate, this method is between first and second order in space. We can't compare to other methods in literature since order of convergence for the more singular case were not reported. However we show that we can resolve the highly singular flow at very early times. We have implemented the method and have resolved detailed aspects of the flows considered. The impact of this work is the resolution in a regime not studied before, and complements other work to give a more comprehensive picture of the flow. We also studied flow quantities not looked at in detail before.

The thesis is organized as follows. Section 2 describes the problems to be solved. Section 3, 4, 5 describe the numerical method FDMHS and implementation details. Section 3 provides the development of FDMHS and performance of the parallel code. Some other methods that I have implemented in the thesis are also outlined. Section 4 presents how I determine necessary resolutions for the computation. Section 5 demonstrates the order of accuracy of FDMHS in space and time in the driven cavity problem and impulsively started flow past finite plate. Section 6 applies FDMHS to the problem of viscous flow past a finite plate using three different background flows, respectively. In the oscillatory case, results of FDMHS are compared with the vortex sheet method. Section 7 applies FDMHS to the problem of viscous flow past a semi-infinite plate. Finally, Section 8 summarizes my results and provides some concluding remarks.

2 Problem description

This section describes the three planar flows that are studied in this work: flow past a finite and a semi-infinite plate, and the driven cavity problem which is used as a test case. It includes all initial and boundary information on the stream function, velocity and incoming vorticity that are required by the numerical method. The problems are described in terms of Cartesian horizontal and vertical coordinates x, y. The fluid velocity is $\mathbf{u}(x, y, t) = \langle u(x, y, t), v(x, y, t)\rangle$, where t is time. In all cases, the fluid is assumed to be incompressible and governed by the Navier-Stokes equations (NSE). The stream function $\psi(x, y, t)$ is defined to be in a way such that $\mathbf{u} = \nabla^{\perp}\psi$, and $\omega(x, y, t) = v_x - u_y$ is the scalar fluid vorticity.

2.1 Driven cavity

Figure 2.1a is a schematic of driven cavity problem considered here. The fluid is contained in a square box open at the top. The velocity is zero at the three walls, and equal to a prescribed parallel driving velocity at the top

$$\mathbf{U}_{\text{top}} = \langle U_{\text{top}}, 0\rangle. \tag{2.1}$$

The computational domain is shown in figure 2.1b. The domain is a square box

$$D = \{(x, y), 0 \le x \le 1, 0 \le y \le 1\}. \tag{2.2}$$

In the classical driven cavity problem, the driving velocity is constant, $U_{\text{top}} =$ constant. However, this induces a jump in the velocity at the top two corners, and this singularity affects the accuracy of any numerical method. To better test the accuracy of our method, we follow E & Liu [8] and set

$$U_{\text{top}}(x) = Ux^2(1 - x)^2 \tag{2.3}$$

where $U = 1$. This driven velocity U_{top} is zeros actually at two top corners which yields a less singular flow. The initial values of the stream function at the interior grid points are

$$\psi_o : \psi(x, y, 0) = U_{\text{top}}(x)(y^2 - y^3) = x^2(1 - x)^2(y^2 - y^3). \tag{2.4}$$

Corresponding boundary values of the stream function are

$$\psi_{\text{bd}} = 0 \quad (x, y) \in \partial D. \tag{2.5}$$

There is no incoming vorticity. This flow was computed by E & Liu using a compact 4th order finite difference scheme. In this work we will implement both E & Liu's method and the new method proposed in the thesis and compare results for the purpose of validation of our method and to establish its order of accuracy.

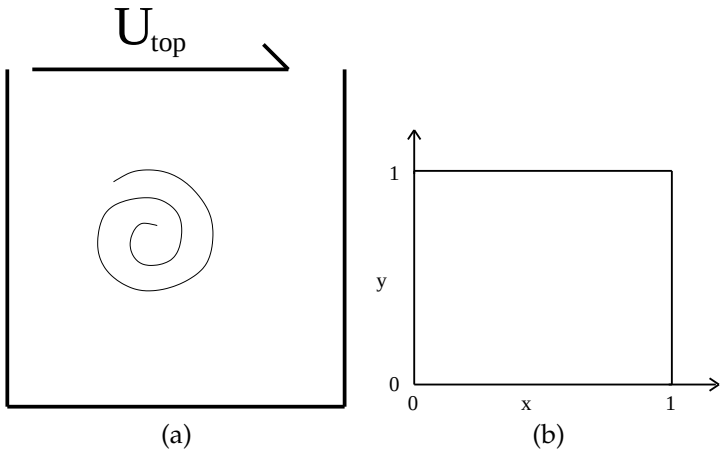

Figure 2.1: (a) A schematic of driven cavity flow and (b) the computational domain of the driven cavity problem.

2.2 Viscous flow past a finite plate

Figure 2.2a is a schematic of the viscous flow past a finite plate. The plate, of length L, is moving downwards with velocity $\langle 0, -U_\infty(t)\rangle$ in direction normal to itself. We will use a different frame in which the plate is stationary with zero velocity at the wall, and the far field flow is moving upward, $\langle 0, U_\infty(t)\rangle$.

It is assumed that the plate has zero thickness and the flow stays symmetric about the center line of the plate. Therefore, the flow is computed only in the half plane $x \geq 0$. The computational domain, shown in figure 2.2b, is a rectangular box

$$D = \{(x, y), 0 \leq x \leq x_{\max}, y_{\min} \leq y \leq y_{\max}\} \tag{2.6}$$

with a slit

$$S = \{(x, y), x \in [0, L/2], y = 0\}. \tag{2.7}$$

The center of the plate is at the origin $(0, 0)$. We consider three far-field flows: impulsively stated $U_\infty(t) = 1$, uniformly accelerated $U_\infty(t) = at$, where a is acceleration and oscillatory $U_\infty(t) = \sin(\frac{\pi t}{\mathrm{KC}})$, see figure 2.3.

The initial flow is given by the potential flow past a finite plate that matches the prescribed far-field velocity. The corresponding stream function $\psi_\infty(x, y, t)$ is the imaginary part of the complex potential

$$W_\infty(x, y, t) = iU_\infty \sqrt{\frac{z - L/2}{z + L/2}} = \phi_\infty + i\psi_\infty, \tag{2.8}$$

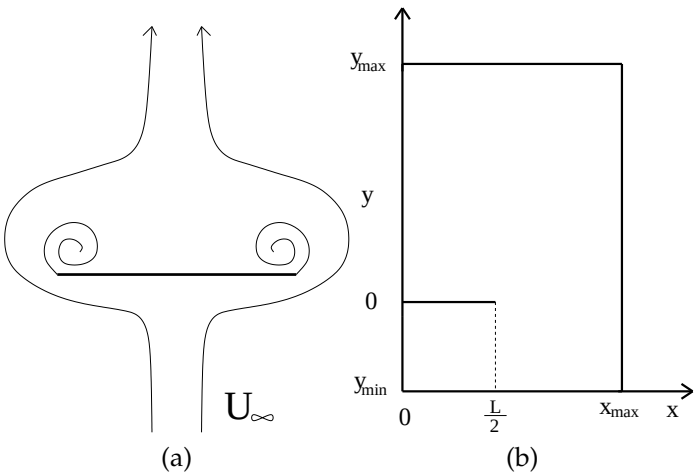

Figure 2.2: (a) A schematic of flow past a finite plate, and (b) the computational domain.

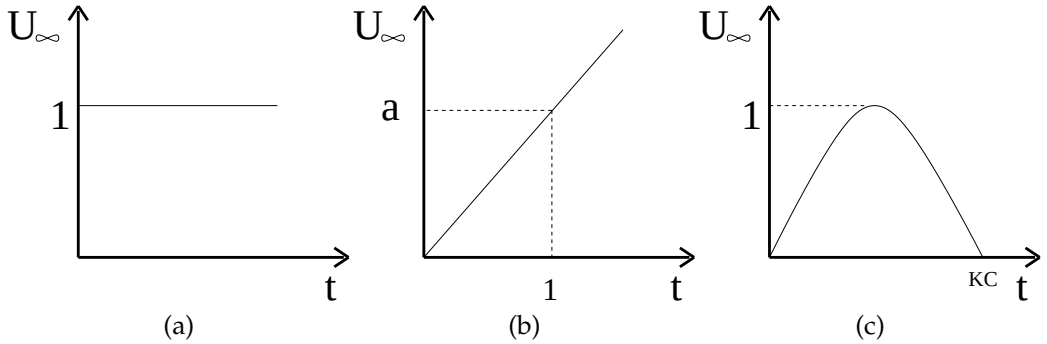

Figure 2.3: Three far-fields flows in simulations of flow past a finite plate. *(a)* Impulsively started, *(b)* Uniformly accelerated, *(c)* Oscillatory.

where $\mathbf{z} = \langle x, y \rangle$, and ϕ is the velocity potential. For simplicity, I compute ψ_∞ using an equivalent vortex sheet that induces U_∞. This procedure is described in Appendix *I*.

The boundary value of the stream function on the plate is zero,

$$\psi_{\text{bd}} : \psi(x, y, t) = 0, \quad (x, y) \in S \tag{2.9}$$

and the boundary values of the stream function on ∂D are computed using the integral formulation (2.10)[33]

$$\psi_{\text{bd}} : \psi(x, y, t) = \psi_\infty(\mathbf{z}, t) + \int\int_{D/S} \omega(\mathbf{z}_o, t) G(\mathbf{z}, \mathbf{z}_o) d\mathbf{z}_o, \quad (x, y) \in \partial D. \tag{2.10}$$

The geometry-specific Green's function $G(x, y, x_0, y_0)$ for the finite plate is

$$G(x, y, x_o, y_o) = \log \left| \frac{\sqrt{\frac{z-L/2}{z+L/2}} - \sqrt{\frac{z_o-L/2}{z_o+L/2}}}{\sqrt{\frac{z-L/2}{z+L/2}} - \left(\sqrt{\frac{z_o-L/2}{z_o+L/2}}\right)^*} \right| \tag{2.11}$$

where z is a complex number $z = x + iy$ and $*$ denotes the complex conjugate. Note that one only needs to compute the integral over the portion of the domain in which vorticity $\omega(\mathbf{z}_o)$ is non-zero to compute the integral of (2.10). In practice, I only integrate over the portion of domain where $|\omega(\mathbf{z}_o)| \geq 10^{-9}$.

The computations are performed using $L = 1$, the whole length of the plate, for the case of the impulsively started and the uniformly accelerated far field flows and $L = 1$ for the oscillatory far field flow. This is consistent with the geometry used in [23] and [18], respectively.

2.3 Viscous flow past a semi-infinite plate

The flow past a semi-infinite plate is considered here. Figure 2.4a is a schematic of viscous flow past a semi-infinite plate. The computational domain, shown in figure 2.4b, is a rectangular box with a slit D/S where

$$D = \{(x, y), x_{\min} \leq x \leq x_{\max}, y_{\min} \leq y \leq y_{\max}\}, \tag{2.12}$$

$$S = \{(x, y), x \in [x_{\min}, 0], y = 0\}. \tag{2.13}$$

In practice, the plate actually occupies the whole negative x-axis with the tip at the origin $(0, 0)$.

The initial flow is the potential flow past a semi-infinite plate with the stream function

$$\psi_\infty(x, y, t) = Ur^{1/2} \cos\left(\frac{\tan^{-1}(y/x)}{2}\right), \tag{2.14}$$

where $r = \sqrt{x^2 + y^2}$, and $U = 1$.

The boundary values of the stream function on the plate is zero,

$$\psi_{\text{bd}} : \psi(x, y, t) = 0, \quad (x, y) \in S \tag{2.15}$$

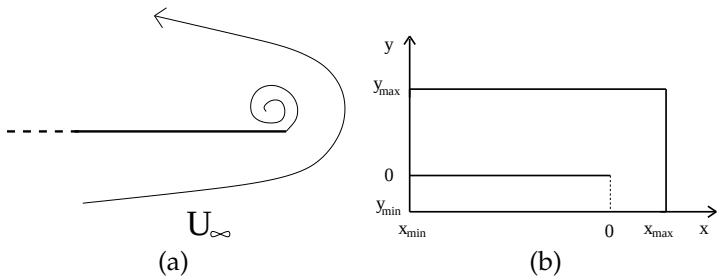

Figure 2.4: (a) A schematic of flow past a semi-infinite plate and (b) the computational domain.

and the boundary values of the stream function on ∂D are computed using (2.10) as well,

$$\psi_{\text{bd}} : \psi(x, y, t) = \psi_\infty(\mathbf{z}, t) + \int\int_{D/S} \omega(\mathbf{z}_0, t) G(\mathbf{z}, \mathbf{z}_0) d\mathbf{z}_0, \quad (x, y) \in \partial D. \tag{2.16}$$

The geometry-specific Green's function for the semi-infinite plate is

$$G(x, y, x_o, y_o) \quad = \quad \frac{1}{2\pi} \log \left| \frac{(iz)^{1/2} - (iz_o)^{1/2}}{(iz^*)^{1/2} - (iz_o)^{1/2}} \right|. \tag{2.17}$$

The computational domain is always finite, though the boundary layer is of infinite length. I will truncate the plate in the computation. The longer the terminal time, the longer the plate should be counted. This is handled as follows.

The vorticity to the left of a line $x = x_{\min}$ is ignored. That is, we set the incoming vorticity at $x = x_{\min}$ equal to zero. The value of $x_{\min}$ is chosen so that particles initially at $x = x_{\min}$ traveling in the potential background flow do not reach a region near the tip by the terminal time T. For example, using $T = 0.03$, $x_{\min}$ is chosen to be -1 such that at the terminal time, the particle has not passed x =-1. A sample trajectory of such a particle for $t \in [0, T]$ is shown in figure 2.5. The particle trajectories are computed by solving the ODE

$$\frac{dx}{dt} = u_\infty(x, y) \quad \frac{dy}{dt} = v_\infty(x, y) \tag{2.18}$$

$$\langle u_\infty(x, y), v_\infty(x, y) \rangle = \nabla^\perp \psi_\infty(x, y), \tag{2.19}$$

where $\langle u_\infty, v_\infty \rangle$ are velocities of the potential flow. The terminal positions of particles are provided.

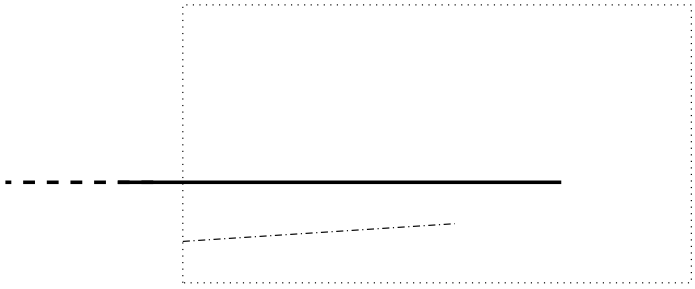

Figure 2.5: Determine the computational domain of flow past a semi-infinite plate.*Solid line*: the semi-infinite plate, *dotted line*: the computational domain, *dash-dotted line*: the path of a fluid particle.

To confirm that the error incurred by setting zero incoming vorticity does not affect the results, the flow is computed in domains with $x_{\min}$=-1,-2 and -3, shown in figure 2.6a for ν=0.002. The numerical method is going to be described in section 3. The size of the computational domain in y direction is chosen large enough such that it does not affect the result. These three computational domains are colored as *black*, *blue* and *red*. The dark thick line in the figure represents the semi-infinite plate. *Black* covers most of the plate while *red* contains the least. Figure 2.6b shows the maximum velocity $U_{\max}$ in $(x, y) \in D/S$ vs.t using these three domains. The fact that $U_{\max}$ overlap using all three domains confirms that the error made by imposing zero incoming vorticity in the smallest domain is negligible. In other words, $x_{\min}$ = -1 is enough for the terminal time T=0.03, and the rest of the plate could be truncated.

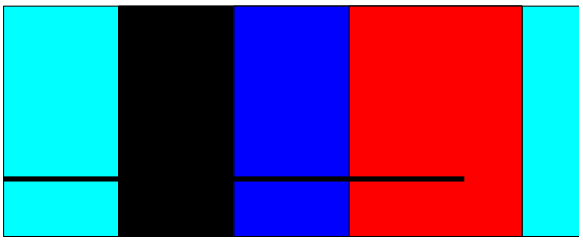

(a)

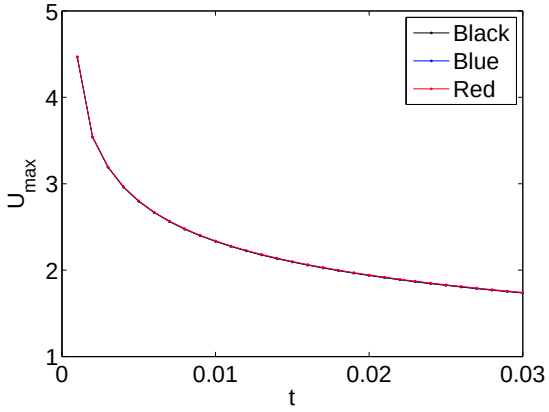

(b)

Figure 2.6: Domain independence verification of flow past a semi-finite plate. (*a*) Three domains are chosen, black, blue and red. (*b*) Plot of maximum velocity $U_{\max}$ vs.t using these three domains.

Table 2.1 shows a list of values of $|x_{\min}|$ for various terminal times T. For the

Terminal time T	$\lvert x_{\min}\rvert$
50	12.21
128	21.7
256	33.8

Table 2.1: Determination of the plate length that should be included, in the computation of flow past a semi-infinite plate, provided that the terminal time is given.

relatively large terminal times listed in this table, the value of $x_{\min}$ is so large in magnitude that solving the problem using sufficient resolution on such a rectangular domain is not feasible. We therefore break up the domain into two pieces as illustrated in figure 2.7. The sub-domain is the long-thin rectangular box below the plate and it contains the lower boundary layer; the main-domain is the rectangular box containing the plate tip and it contains the starting vortex of interest. We pre-compute the vorticity in the sub-domain, and use its result as the incoming boundary condition of vorticity for the main-domain. We thus do not account for the effect of the starting vortex on the vorticity boundary layer far from tip. The effect is expected to be small, but this still has to be confirmed numerically.

Figure 2.7: The domain decomposition of flow past a semi-infinite plate. The simulation in sub-domain (*cyan*) is pre-computed and its results provide the incoming vorticity boundary condition for the main domain (*red*), in which a following simulation is conducted. The overlap between the two regions is shown in *green*.

3 Numerical methods

3.1 Motivation

The governing equations are the 2D incompressible Navier-Stokes equations (NSE). In the stream function-vorticity formulation, they are given by (3.1).

$$\text{(a)} \quad \frac{D\omega}{Dt} = \nu\nabla^2\omega, \qquad \text{(b)} \quad \nabla^2\psi = \omega, \qquad \text{(c)} \quad \mathbf{u} = \nabla^\perp\psi = \langle -\frac{\partial\psi}{\partial y}, \frac{\partial\psi}{\partial x}\rangle, \tag{3.1}$$

where $\mathbf{u} = \langle u, v\rangle$ and $\frac{D}{Dt} = \frac{\partial}{\partial t} + \mathbf{u}\cdot\nabla$ is the material derivative. The initial vorticity $\omega(t = 0)$ is given. The velocity is zero at steady walls, and prescribed at infinity. The Reynolds number is defined as

$$Re = \frac{LU}{\nu} \tag{3.2}$$

where L and U are the characteristic length and velocity, ν is kinematic viscosity.

Flow past plates considered here has a range of space and time scales. The flow is initially singular with unbounded velocity at the tip of the plate. Large velocity gradients are present within thin boundary layers in the vicinity of the plate. Small length scales are given by the boundary layer thickness $\delta \sim \sqrt{\nu t}$ when t or ν are small. Numerical methods to simulate such flow require that these small length scales, as well as large scales at later times, be properly represented. To this effect, I consider several methods in the literature and list their advantages and disadvantages below.

E and Liu [8] presented an essentially compact fourth order scheme, referred to here as EC4, and applied it to the driven cavity problem. It is a finite difference method, fourth order in both space and time. It uses compact finite differences, that is using information on nearby grid points, at interior and for the boundary conditions. Vorticity generated at the walls is related to the stream function by a fourth order Thomas' formula. The fourth order Runge-Kutta method is used to advance in time. Details of EC4 are described in section 3.4. Johnston [17] implemented EC4 for the problem of viscous flow past a cylinder, and showed well-resolved results of the boundary layer. I have implemented EC4 for the driven cavity problem and reproduced E& Liu's results. I have also applied EC4 to simulate flow past the semi-infinite plate and found it to be unstable near the plate tip. The solution develops large extraneous oscillations that do not vanish as the mesh is refined. This is attributed to the fact that the method is explicit

in time and does not handle the large gradients near the wall. Some effort has been made to make EC4 implicit in time, unsuccessfully. It is hard to make the temporal derivative implicit while maintaining the compactness and the fourth order accuracy in time.

Koumoutsakos and Shields [23], referred to as KS, used a particle method to compute flow past a finite plate. These are Lagrangian methods that track particles which carry the fluid vorticity. They move with the fluid velocity, which is computed using the Biot-Savart law, as an integral over the region containing vorticity. Vorticity diffusion between particles is accounted for using the method of particle strength exchange, Degond & Mas-Gallic[7]. For a review, see Koumoutsakos [21]. Vorticity generation at the walls is based on the technique introduced by Koumoutsakos & Pepin [24] which embodies Lighthill's creation mechanism. High resolution can be achieved in local regions by placing a large number of vortex particles in those regions. This method was first applied to flow past a cylinder [22], and then extended to planar flow past a finite plate [23], and has also been applied to 3D flow [20]. Eldredge modified a vortex particle method with a simplified particle treatment near the boundary and applied it to simulate a flapping wing with hovering insect kinematics. Particle-based methods provide an alternative to grid-based method. However, the vortex particle method is of low order and the simulations in the literature do not resolve small scale features.

Luchini and Tognaccini [29], referred as LT, used a a highly domain-specific finite difference method to simulate flow past a semi-infinite plate. They used the scaling property of the flow (also see section 2), to derive an alternative formulation in which variables scale in time. They solved these scaled equation using a finite difference method, in essence resolving small scales initially and large scales at later times equally well. Their method uses an upwind scheme to treat vorticity convection, the Crank-Nicolson method to advance in time, and the Thomas formula to generate vorticity at the plate (see section 3.2.4). The method is formally second order in space and time. LT use an exponentially decaying analytical function to approximate the incoming vorticity from the boundary layers outside the computational domain. In the results, the outer spiral turn of the leading vortex becomes unstable. It is not clear whether their boundary layer approximation introduces the oscillations that leads to the unstable behavior. We will recompute this flow using an alternative method and a different approximation of the incoming boundary layer, computed numerically (see section 2.3), and use our results to resolve the early dynamics, which are not studied in LT.

I decided to develop a new method to fulfill the goal of resolving the initially singular flow. It is desired that this new method be suitable for problems with a

large range of space and time scales, be capable of unveiling details of the flow near the plate tip initially and be able to use large time steps while maintaining numerical stability. We use some of the ideas in the works discussed above and combine them with others. Based on our experience, the treatment of the temporal derivative has to be implicit; the compactness and fourth order approximations are preferred, since these properties yield lower truncation errors in the approximation; and high resolution at early times is necessary to better represent the small scales and large gradients near the plate. We denote this method as Finite Difference Method of High Order in Space, FDMHS. The method is described below.

3.2 Finite Difference Method of High Order in Space (FDMHS)

FDMHS is a compact fourth order finite difference method using a regular, rectangular grid to solve the 2D incompressible Navier-Stokes equations (NSE) in stream function-vorticity formulation, 3.1. It requires initial and boundary conditions on the stream function ψ and incoming vorticity at the boundary. Outgoing nonzero vorticity at the boundary is approximated using extrapolation along characteristics.

We establish the finite difference grid in the 2D computational domain as

$$x_{\min} = x_0, x_1, \cdots x_i, \cdots, x_{Nx-1}, x_{Nx} = x_{\max}, \qquad i = 0, \cdots, Nx \tag{3.3}$$

$$y_{\min} = y_0, y_1, \cdots y_j, \cdots, y_{Ny-1}, y_{Ny} = y_{\max}, \qquad j = 0, \cdots, Ny \tag{3.4}$$

where $x_i = x_{\min} + ih$, $y_j = y_{\min} + jh$, and $h = (x_{\max} - x_{\min})/Nx = (y_{\max} - y_{\min})/Ny$. Similarly, time is partitioned as

$$0 = t_0, t_1, \cdots t_n \cdots, t_{N-1}, t_N = T, \qquad n = 0, \cdots, N \tag{3.5}$$

where $t_n = n\Delta t$ and $T = N\Delta t$. $\psi^n_{i,j}$ approximates $\psi(x_i, y_j, t_n)$, the value of the stream function at the grid point (x_i, y_j) at time $t = t_n$. The interior grid points are given by $1 \le i \le Nx - 1$ and $1 \le j \le Ny - 1$. We now list some notation that will be used in the following contents. Δ_h is the five point stencil to approximate the Laplacian operator ∇^2; D^2_x is the second order central difference to approximate $\partial^2/\partial x^2$ and D^2_y is the second order central difference to approximate $\partial^2/\partial y^2$; $\tilde{D}_x$ is the second order central difference to approximate $\partial/\partial x$ and $\tilde{D}_y$ is the second order central difference to approximate $\partial/\partial y$; as follows,

$$\Delta_h f = \frac{f_{i+1,j} + f_{i-1,j} - 4f_{i,j} + f_{i,j+1} + f_{i,j-1}}{h^2} \tag{3.6}$$

$$D_x^2 f_{i,j} = \frac{f_{i+1,j} - 2f_{i,j} + f_{i-1,j}}{h^2} \tag{3.7}$$

$$D_y^2 f_{i,j} = \frac{f_{i,j+1} - 2f_{i,j} + f_{i,j-1}}{h^2} \tag{3.8}$$

$$\tilde{D}_x f_{i,j} = \frac{f_{i+1,j} - f_{i-1,j}}{2h} \tag{3.9}$$

$$\tilde{D}_x f_{i,j} = \frac{f_{i,j+1} - f_{i,j-1}}{2h}. \tag{3.10}$$

FDMHS is a split method which, in rough terms, first solves the inviscid portion of the transport equation (3.1)a,

$$\frac{\partial \omega^*}{\partial t} = -\mathbf{u} \cdot \nabla \omega^*, \quad \text{that is} \quad \frac{D\omega^*}{Dt} = 0, \tag{3.11}$$

and then solves the viscous portion

$$\frac{\partial \omega}{\partial t} = \nu \nabla^2 \omega^*. \tag{3.12}$$

Here, ω^* denotes an intermediate vorticity value. (3.11) is solved using a semi-Lagrangian scheme, which is second order in time and fourth order in space. (3.12) is solved using a Crank-Nicolson method which is second order in time and fourth order in space. Even though the scheme for each temporal step is relatively high order in space and time, the splitting scheme reduces the overall order of accuracy in time. In the next subsections, the whole algorithm is presented, followed by details for each step.

3.2.1 The algorithm

Initialization. Prescribe the initial conditions of the stream function ψ_o, and give the incoming vorticity condition if it is non-zero.

To advance from t_n to t_{n+1},

Step 1: Solve the vorticity convection in the interior

$$\frac{d\omega^*}{dt} = 0 \tag{3.13}$$

using a two-level semi-Lagrangian method. The method consists of three stages

1 For each interior grid point, assuming a particle sits here, find the location of the particle at t_n along the characteristic path. This is equivalent to solving

$$\frac{d\mathbf{z}}{dt} = \mathbf{u}(\mathbf{z}, t) \quad \mathbf{z}(t_{n+1}) = (x_i, y_j). \tag{3.14}$$

where $\mathbf{z} = \langle x, y \rangle$.

2 Obtain the vorticity $\omega(\mathbf{z}(t_n), t_n)$ of the particle from vorticity values at nearby grid points using a fourth order bi-cubic interpolation.

3 Set $\omega^*(x_i, y_j, t_{n+1}) = \omega(\mathbf{z}(t_n), t_n)$.

Step 2a: Compute ψ_{bd} using the integral formulation (2.10) for the finite plate, or the equivalent (2.16) for the semi-infinite plate. The integral is computed using the fourth order Simpson's method. We integrate only over that portion of the domain in which $|\omega| \geq 10^{-9}$. For the driven cavity problem, set $\psi_{\text{bd}} = 0$.

Step 2b: Find the stream function in the interior by solving the Poisson equation

$$\nabla^2 \psi = \omega^* \tag{3.15}$$

using a fourth order finite difference scheme [43]

$$(\Delta_h + \frac{h^2}{6} D_x^2 D_y^2)\psi^{n+1} = (1 + \frac{h^2}{12}\Delta_h)\omega^*. \tag{3.16}$$

The Conjugate Gradient method is used to invert the resulting linear system.

Step 3: Update the velocity

$$\mathbf{u} = \nabla^\perp \psi. \tag{3.17}$$

on the interior grid points using a fourth order central difference method

$$u^{n+1} = -\tilde{D}_y(1 - \frac{h^2}{6} D_y^2)\psi^{n+1} \tag{3.18}$$

$$v^{n+1} = \tilde{D}_x(1 - \frac{h^2}{6} D_x^2)\psi^{n+1}. \tag{3.19}$$

Step 4a: Compute the vorticity on the walls using Thomas' formula. For the finite plate problem, the vorticity on all four sides of the rectangular domain is

zero. Specify the incoming vorticity on incoming boundaries and set it using extrapolation on the outgoing boundaries.

Step 4b: Update ω^{n+1} on the interior grid points from

$$\frac{\partial \omega^{n+1}}{\partial t} = \nu \Delta \omega^{*} \tag{3.20}$$

using a three-level Crank-Nicolson method.

3.2.2 Two-level semi-Lagrangian method

The semi-Lagrangian method is widely used to solve the convection process for partial differential equations. It is derived from the Lagrangian nature of flow transport and allows computation on Cartesian grids. Traditional numerical techniques for convection equation are subject to the CFL stability condition, which imposes a restriction on the time steps in the computation. The semi-Lagrangian method traces particles along the characteristic curve and this allows for a larger time step.

Following [39][42][45], the two-level semi-Lagrangian technique basically uses the information on the current time stage and one time stage before. The convection equation in my method is

$$\frac{D\omega}{Dt} = 0. \tag{3.21}$$

Suppose a fluid particle resides at a given grid point (x_i, y_i) at time t_{n+1}. One obtains the vorticity value $\omega(x_i, y_i, t_{n+1})$ carried by this particle through three stages. First, find the particle's position at the previous time, t_n. This is equivalent to solving the ODE

$$\frac{d\mathbf{z}}{dt} = \mathbf{u}(\mathbf{z}, t), \quad \mathbf{z}(t_{n+1}) = (x_i, y_i). \tag{3.22}$$

Then, recover the vorticity value $\omega(\mathbf{z}(t_n), t_n)$ by values in its neighborhood. Last, assign $\omega(x_i, y_i, t_{n+1}) = \omega(\mathbf{z}(t_n), t_n)$. Repeat this process for all grid points (x_i, y_i). Next, details of the computation is presented.

Integrate the ODE (3.22) and write the solution as

$$\mathbf{z}(t_n) = \mathbf{z}(t_{n+1}) - \int_{t_n}^{t_{n+1}} \mathbf{u}(\mathbf{z}(t), t) dt. \tag{3.23}$$

This integration can be evaluated using a Runge-Kutta method. Here, I use the method proposed in [42] which is second order in time. Denoting $\Delta\mathbf{z} = \mathbf{z}(t_{n+1}) - \mathbf{z}(t_n) = \int_{t_n}^{t_{n+1}} \mathbf{u}(\mathbf{z}(t), t)dt$ and using the mid-point rule to approximate the integral in (3.23), yields

$$\begin{aligned}
\int_{t_n}^{t_{n+1}} \mathbf{u}(\mathbf{z}(t), t)dt &= \Delta t\mathbf{u}(\mathbf{z}(t_{n+\frac{1}{2}}), t_{n+\frac{1}{2}}) + O(\Delta t^3) && (3.24)\\
&= \Delta t\mathbf{u}(\mathbf{z}(t_{n+1}) - \frac{\Delta\mathbf{z}}{2} + O(\Delta t^2), t_{n+\frac{1}{2}}) + O(\Delta t^3) && (3.25)\\
&= \Delta t\mathbf{u}(\mathbf{z}(t_{n+1}) - \frac{\Delta\mathbf{z}}{2}, t_{n+\frac{1}{2}}) + O(\Delta t^3). && (3.26)
\end{aligned}$$

This is written as

$$\Delta\mathbf{z} = \Delta t\mathbf{u}(\mathbf{z}(t_{n+1}) - \frac{\Delta\mathbf{z}}{2}, t_{n+\frac{1}{2}}) + O(\Delta t^3). \tag{3.27}$$

(3.27) is an implicit formula for $\Delta\mathbf{z}$ in terms of known velocity field at two previous time stages. Using a second order extrapolation from two previous time stages to find the velocity at $t_{n+\frac{1}{2}}$

$$\mathbf{u}(\mathbf{z}, t_{n+\frac{1}{2}}) = \frac{3}{2}\,\mathbf{u}(\mathbf{z}, t_n) - \frac{1}{2}\,\mathbf{u}(\mathbf{z}, t_{n-1}) + O(\Delta t^2), \tag{3.28}$$

we obtain the following iterative scheme to compute $\Delta\mathbf{z}$,

$$\begin{aligned}
\Delta\mathbf{z}^0 &= \Delta t\left[\frac{3}{2}\mathbf{u}(\mathbf{z}, t_n) - \frac{1}{2}\mathbf{u}(\mathbf{z}, t_{n-1})\right], && (3.29)\\
\Delta\mathbf{z}^k &= \Delta t\left[\frac{3}{2}\mathbf{u}(\mathbf{z} - \frac{1}{2}\Delta\mathbf{z}^{k-1}, t_n) - \frac{1}{2}\mathbf{u}(\mathbf{z} - \frac{1}{2}\Delta\mathbf{z}^{k-1}, t_{n-1})\right], \qquad k = 1, 2, \ldots && (3.30)
\end{aligned}$$

Once $\Delta\mathbf{z}$ is known, the departure point along the characteristics path is

$$\mathbf{z} = \mathbf{z}(t_{n+1}) - \Delta\mathbf{z}. \tag{3.31}$$

Usually, $\mathbf{z}$ will not coincide with a grid point. Therefore, the velocity $\mathbf{u}$ and vorticity ω are obtained by interpolation from the known values in the neighborhood. The fourth order bi-cubic interpolation is used since it has smaller truncation errors than a lower order interpolation method, for example, the bilinear interpolation.

3.2.3 Solve the Poisson equation and compute the velocity near the boundary

In section 3.2.1, step 2, the boundary values of the stream function are required in order to solve the Poisson equation, expressions of ψ_{bd} are given in section 2.

Remember that for flow past plates, we use Biot-Savart formula to compute ψ_{bd}, and the formula is calculated using the 2D Simpson integration technique which is fourth order in space. Actually, the Biot-Savart formula can be used in the interior as well to compute ψ. The problem is that the computational time is too expensive, therefore, we solve for ψ using the Poisson equation instead.

The Poisson equation is solved by Conjugate Gradient (CG) (The tolerance is the residual is $\leq 10^{-9}$). CG is one of the optimal options if the linear system is positive definite and symmetric, other optimal options include methods based on FFT, Multigrid, etc.. Therefore, CG is suitable for the driven cavity problem. For the cases of flow past finite and semi-infinite plates, the linear system is positive-definite but slightly non-symmetric due to the presence of the plate. A comparison of the performance of CG, BiCGS (Bi-Conjugate Gradient Stabilize) and GMRES (General Minimum Residual Scheme)[15] is shown in table 3.1 for the driven cavity problem and the problem of flow past a finite plate. The computations are conducted on my laptop. The CPU time is the time elapsed for a fixed number of iterations. In the driven cavity problem, the number of grid points in the x and y directions is 100×100 and the CPU time is for 100 iterations. For the finite plate problem (FP), a second order finite difference method (FDM2) and FDMHS are used. The CPU time is for 40 iterations, and the number of grid points are 40×40. The Reynolds number is 20 for all. Apparently, CG converges in my problem for a slightly non-symmetric linear system, and it takes the least time.

Driven Cavity		FP FDM2		FP FDMH	
Method	CPU time(sec)	Method	CPU time	Method	CPU time
CG	29.936	CG	4.82	CG	61.64
BiCGS	49.728	BiCGS	5.94	BiCGS	63.96
GMRES	420.5970	GMRES	43.53	GMRES	100.174

Table 3.1: The Comparison of three Poisson solvers: CG, BiCGS and GMRES[15]. *FP* stands for the problem of flow past a finite plate. *FDM2* stands for a finite difference method that is second order in space and time. The computations are performed on my laptop.

In section 3.2.1, step 3, a fourth order one-sided finite difference method is used to compute the velocity on the grid points next to the plate. The Biot-Savart formula is used to compute the stream function ψ on ghost points just outside the computational domain, given by $i = Nx + 1, -1 \leq j \leq Ny + 1$, $i = -1, -1 \leq j \leq Ny + 1$, $j = Ny + 1, -1 \leq i \leq Nx + 1$ and $j = -1, -1 \leq i \leq Nx + 1$, so that the fourth order central difference method can be applied to interior grid points near the four sides of the domain.

3.2.4 Thomas' formula

Following [8], Thomas' formula is used to compute the vorticity generation from the plate. Recall that the horizontal velocity u and vorticity ω are calculated using

$$u = -\frac{\partial \psi}{\partial y}, \quad \omega = (\frac{\partial^2 \psi}{\partial x^2} + \frac{\partial^2 \psi}{\partial y^2}). \tag{3.32}$$

The spatial grid points near a solid boundary are depicted in figure 3.1, where the

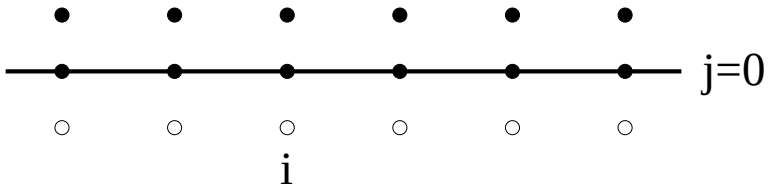

Figure 3.1: Spatial mesh grids near the solid boundary.

solid line is the plate, the solid dots are the actual grid points, and the empty dots are the ghost points located outside of the domain. For simplicity, $j = 0$ represents the plate. The horizontal velocity and the stream function, as well as the first and second derivatives of ψ are all zero at $j = 0$.

$$u_{i,0} = 0, \quad \psi_{i,0} = 0, \quad \left(\frac{\partial \psi}{\partial x}\right)_{i,0} = 0, \quad \left(\frac{\partial^2 \psi}{\partial x^2}\right)_{i,0} = 0. \tag{3.33}$$

Using the second order central difference method to approximate $u_{i,0}$

$$u_{i,0} = \frac{\psi_{i,1} - \psi_{i,-1}}{2\Delta y} = 0, \tag{3.34}$$

this yields

$$\psi_{i,-1} = \psi_{i,1}. \tag{3.35}$$

Using the second order central difference method to approximate vorticity on the boundary $\omega_{i,0}$, one gets

$$\omega_{i,0} = \left(\frac{\partial^2 \psi}{\partial y^2}\right)_{i,0} = -\frac{\psi_{i,1} - 2\psi_{i,0} + \psi_{i,-1}}{\Delta y^2} = \frac{2\psi_{i,1}}{\Delta y^2}. \tag{3.36}$$

Using (3.35) in (3.36), one gets

$$\omega_{i,0} = \frac{2\psi_{i,1}}{\Delta y^2}. \tag{3.37}$$

(3.37) concludes the second order Thomas' formula.

The fourth order Thomas' formula can be derived in a similar manner. Using two fourth order finite differences to approximate $u_{i,0}$, one writes

$$0 = \frac{1}{12}\psi_{i,-2} - \frac{2}{3}\psi_{i,-1} + \frac{2}{3}\psi_{i,1} - \frac{1}{12}\psi_{i,2} \tag{3.38}$$

$$0 = -\frac{1}{4}\psi_{i,-1} - \frac{3}{2}\psi_{i,1} - \frac{1}{2}\psi_{i,2} + \frac{1}{4}\psi_{i,3}. \tag{3.39}$$

Note that $\psi_{i,0}$ is erased from equations above since it is zero. Considering $\psi_{i,-1}$ and $\psi_{i,-2}$ as unknowns, one solves them to get

$$\psi_{i,-1} = 6\psi_{i,1} - 2\psi_{i,2} + \frac{1}{3}\psi_{i,3} \tag{3.40}$$

$$\psi_{i,-2} = 40\psi_{i,1} - 15\psi_{i,1} + \frac{8}{3}\psi_{i,3}. \tag{3.41}$$

Applying the fourth order central difference to the vorticity $\omega_{i,0}$, one has

$$\omega_{i,0} = \left(\frac{\partial^2\psi}{\partial y^2}\right)_{i,0} = \frac{-\frac{1}{12}\psi_{i,-2} + \frac{4}{3}\psi_{i,-1} - \frac{4}{3}\psi_{i,1} - \frac{1}{12}\psi_{i,2}}{\Delta y^2} = \frac{6\psi_{i,1} - \frac{3}{2}\psi_{i,2} + \frac{4}{9}\psi_{i,3}}{\Delta y^2}. \tag{3.42}$$

Using the expressions of $\psi_{i,-1}$ and $\psi_{i,-2}$ in $\omega_{i,0}$, one solves these two equations to get

$$\omega_{i,0} = \frac{6\psi_{i,1} - \frac{3}{2}\psi_{i,2} + \frac{4}{9}\psi_{i,3}}{\Delta y^2} \tag{3.43}$$

(3.43) concludes the fourth order Thomas' formula.

The fourth order central difference scheme is used to compute ω^* on the grid point of the plate tip.

3.2.5 Two-level and three-level Crank-Nicolson methods

Starting with the diffusion equation

$$\frac{\partial\omega}{\partial t} = \nu\nabla^2\omega \tag{3.44}$$

and using a fourth order approximation in space, one gets

$$(1 + \frac{h^2}{12}\Delta_h)\frac{\partial\omega}{\partial t} = \nu(\Delta_h + \frac{h^2}{6}D_x^2D_y^2)\omega. \tag{3.45}$$

The variable ω^{n+1} is the vorticity at the time stage t_{n+1}. Apply the Taylor expansion to ω^{n+1} in time,

$$\omega^{n+1} = \omega^n + \Delta t[\frac{\Delta\omega^n}{\Delta t}] + O(\Delta t^2) \tag{3.46}$$

where $\Delta\omega$ means a small increment of ω in time. Now one has

$$\left(\frac{\partial\omega}{\partial t}\right)^n \approx \frac{\Delta\omega^n}{\Delta t} + O(\Delta t). \tag{3.47}$$

The $\left(\frac{\partial\omega}{\partial t}\right)$ on the left hand side of (3.45) is approximated by $\frac{\Delta\omega^{n+1}}{\Delta t}$, and for the right hand side of (3.45), ω is split into two time stages, n and $n+1$, by a weight β

$$\omega \approx \beta\omega^n + (1-\beta)\omega^{n+1}, \tag{3.48}$$

where β is chosen to be 0.5 following a standard second order Crank-Nicolson method. Therefore, (3.45) becomes

$$(1 + \frac{h^2}{12}\Delta_h)\frac{\Delta\omega^{n+1}}{\Delta t} = \nu(1-\beta)(\Delta_h + \frac{h^2}{6}D_x^2D_y^2)\omega^n + \nu\beta(\Delta_h + \frac{h^2}{6}D_x^2D_y^2)\omega^{n+1}. \tag{3.49}$$

Rearranging the above equation and using

$$\omega^{n+1} = \omega^n + \Delta\omega^{n+1}, \tag{3.50}$$

one has

$$[1 + \frac{h^2}{12}\Delta_h - \beta\nu\Delta t(\Delta_h + \frac{h^2}{6}D_x^2D_y^2)]\Delta\omega^{n+1} = \nu\Delta t(\Delta_h + \frac{h^2}{6}D_x^2D_y^2)\omega^n. \tag{3.51}$$

(3.50) and (3.51) concludes the two-level Crank-Nicolson method. This method is first order in time, fourth order in space.

Similarly, one can derive a three-level Crank-Nicolson which has smaller errors in time, see [14]. I have modified the three-level Crank-Nicolson method to make it fourth order as well. This fourth order three level method is described next.

One starts with the difference equation (3.45) directly. A second order central difference method is used to approximate $\frac{\partial\omega}{\partial t}$ at the time stage n,

$$\frac{\partial\omega}{\partial t} \approx \frac{\omega^{n+1} - \omega^{n-1}}{2\Delta t} + O(\Delta t^2) \tag{3.52}$$

$$= \frac{\Delta\omega^{n+1}}{2\Delta t} + \frac{\Delta\omega^n}{2\Delta t} + O(\Delta t^2). \tag{3.53}$$

The weight α is introduced to make the expression of $\frac{\partial \omega}{\partial t}$ more general

$$\frac{\partial \omega}{\partial t} \approx (1+\alpha)\frac{\Delta \omega^{n+1}}{\Delta t} - \alpha \frac{\Delta \omega^{n}}{\Delta t}. \tag{3.54}$$

In my computation, α is chosen to be 0.5 following [14]. (3.54) is used to approximate the $\frac{\partial \omega}{\partial t}$ on the left hand side of (3.45). Similarly, ω is split as

$$\omega \approx \beta \omega^{n} + (1-\beta)\omega^{n+1}, \tag{3.55}$$

and used to replace ω on the right hand of (3.45). Therefore, one has

$$(1+\frac{h^2}{12}\Delta_h)[(1+\alpha)\frac{\Delta \omega^{n+1}}{\Delta t} - \alpha \frac{\Delta \omega^{n}}{\Delta t}] = \nu(1-\beta)(\Delta_h + \frac{h^2}{6}D_x^2 D_y^2)\omega^n + \nu\beta(\Delta_h + \frac{h^2}{6}D_x^2 D_y^2)\omega^{n+1} \tag{3.56}$$

Rearrange the above equation to yield

$$[1+\tfrac{h^2}{12}\Delta_h - \tfrac{\beta\nu\Delta t}{1+\alpha}(\Delta_h + \tfrac{h^2}{6}D_x^2 D_y^2)]\Delta\omega^{n+1} = \tfrac{\nu\Delta t}{1+\alpha}(\Delta_h + \tfrac{h^2}{6}D_x^2 D_y^2)\omega^n + \tfrac{\alpha}{1+\alpha}(1+\tfrac{h^2}{12}\Delta_h)\Delta\omega^n \tag{3.57}$$

The vorticity ω at time stage $n+1$ is then computed by

$$\omega^{n+1} = \omega^n + \Delta\omega^{n+1}. \tag{3.58}$$

(3.57) and (3.58) conclude the three-level Crank-Nicolson method. This method is a second order in time, fourth order in space approximation to ω^n on each grid point based on the Taylor expansion.

3.3 Efficient implementations

3.3.1 Parallel implementation and efficiency

FDMHS is a compact finite difference method and this property makes it ideal to exploit on modern multi-core clusters or supercomputers. I parallelized FDMHS using the MPI interface and implemented the code on clusters at CARC (Center for Advanced Research Computing) at UNM. Figure 3.2 illustrates the domain decomposition of parallel FDMHS using twelve processors in the finite plate case. The thin solid line around the rectangular box sets the size of the computational domain. The bold solid line is the plate, the bold dashed line is the center line of the plate. Black dots are interior grid points and empty dots are boundary grid points. The grid points around each subdomain from inside serve as the boundary grid points for its neighbors. At every time step, processors exchange information

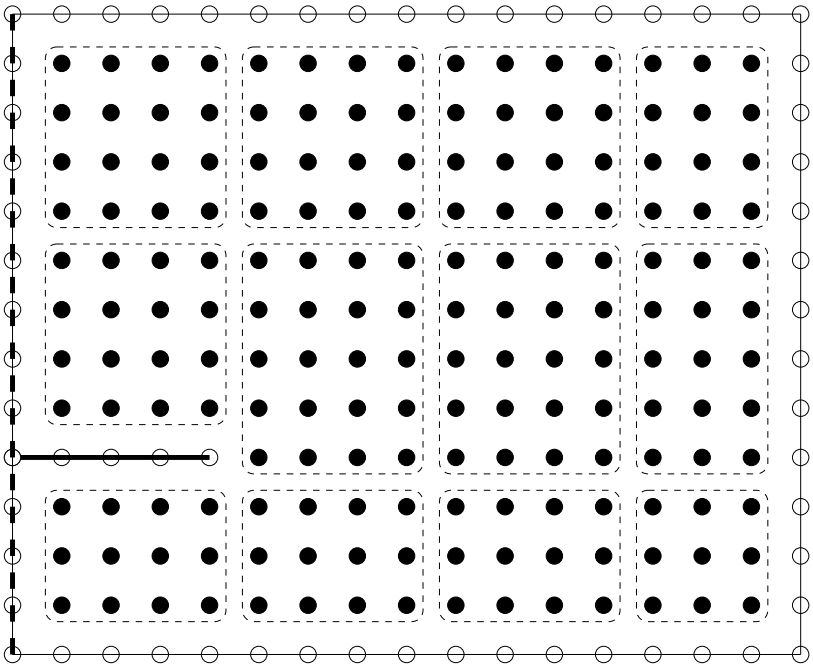

Figure 3.2: The application of parallel FDMHS using 12 processors. Bold solid line is the plate; bold dashed line is the center line of the plate; the solid line around four sides sets the computational domain; black dots are interior grid points; empty dots are boundary grid points.

of boundary values, and the time this process takes is called the communication cost.

The performance of a parallel program is a complex issue. The metrics that people measure can be execution time, parallel efficiency, memory requirement, latency, hardware requirement, etc.. The relative importance of these diverse metrics will vary according to the nature of the problem. In my problem, I am interested in the runtime of FDMHS in strong scaling and weak scaling. In strong scaling, the total size of the problem or data is fixed, and one adjusts the number of processors. Let t_P denote the runtime using P processors. Speed up S_P is the ratio t_1/t_P. Ideally, using P processors is P times faster than using one processor, as $t_1/t_P = P$. The speed up can be viewed as a normalization of the runtime, and it characterizes the scalability of the program. In weak scaling, the size of the problem or data on each processor is fixed, If more processors are used, the total size of the problem needed to be adjusted.

We test the strong scaling in the driven cavity problem. The degree of freedom, DOF, is the total number of grid points in the computation, it is 10^6. The compu-

tations are performed on the cluster *pequena* at CARC of UNM. This cluster uses InfiniBand interconnect and has 8 processors per node. Figure 3.3 shows the speed up in strong scaling, t_1 is the runtime of the serial code. This figure shows that for $P = 40$, the speedup almost lies on the linear line, corresponding to almost 100% efficiency. Table 3.2 gives corresponding the runtime per DOF, t_1 here is the runtime of the parallel FDMHS on one processor. In my computation, the runtime on one processor is greater than the runtime using the serial code.

We test the weak scaling in the problem of flow past a finite plate. A fixed number of DOF ($= 2.56 \times 10^4$) is assigned to each processor. Computations are performed on the cluster *nano* at CARC of UNM. The cluster uses Myrinet interconnect, and has 4 processors per node. Table 3.3 shows the average runtime per time step per processor. The runtime scales well, and is basically independent of the number of processors used.

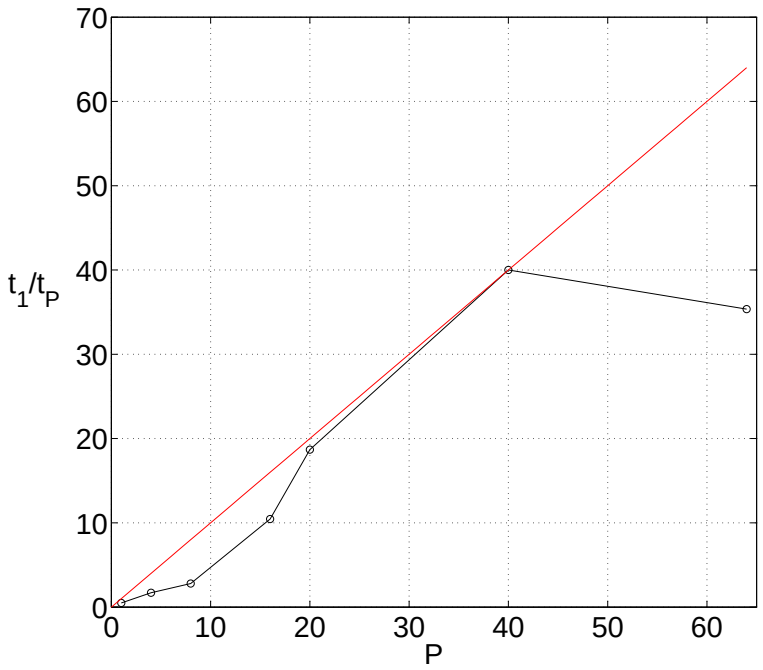

Figure 3.3: Strong scaling of FDMHS in the driven cavity problem. The figure plots the speed up (t_P/t_1)vs.P, where t_P is the runtime for a sample problem with a fixed number of degrees of freedom ($= 10^6$) computed on P processors. t_1 is the runtime of the serial code.

p	1	4	8	16	20	40	64
t_PP/DOF (μs)	3197	3663	4457	2389	1670	1560	2824

Table 3.2: Strong scaling of FDMHS in the problem of flow past a finite plate. Number of micro seconds per time step for a fixed number of degrees of freedom (DOF) (10^6). t_1 is the runtime of parallel FDMHS using one processor.

P	4	9	16	25
t_PP/DOF (μs)	1428	1418	1465	1481

Table 3.3: Weak scaling of FDMHS. Average number of micro second per time step for a fixed number of degrees of freedom ($= 2.56 \times 10^4$) per processor.

3.3.2 Domain decomposition and CG as the Poisson solver

The domain decomposition is employed for simulations of flow past a semi-infinite plate in order to count the vorticity along the plate at infinity, see section 2, and CG is used for the Poisson equation, see section 3.2.3. Both techniques are stressed here again is because that they are considered as efficient implementations as well.

3.3.3 Adaptive domain

For simulations of viscous flow past a semi-infinite (main domain) plates, the computations use a thin domain initially, when the support of the vorticity is small but the flow is highly singular, requiring small mesh sizes and time steps. At later times, the computational domain will be increased adaptively, as indicated in figure 3.4. This is still an on-going work.

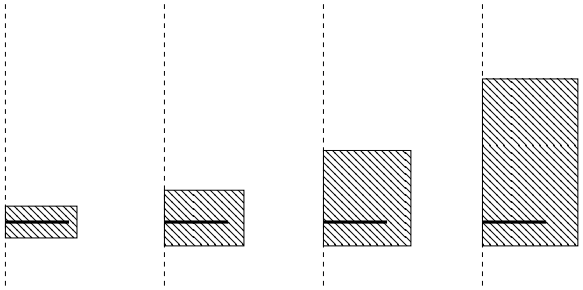

Figure 3.4: A adaptive domain is used in flow past a finite plate to save computational expense.

3.4 Other methods

The following sections give brief descriptions of a second order finite difference method (FDM2), the essentially compact scheme (EC4) and the vortex sheet method. The results of those methods are compared with that of FDMHS in the thesis.

3.4.1 FDM2

FDM2 solves the NSE (3.1) in the stream function vorticity formulation. The algorithm of FDM2 is listed below.

Initialization. Prescribe the initial and boundary conditions of the stream function ψ_o.

Advance the time from t_n to t_{n+1},
Step 1: Obtain the stream function by solving the Poisson equation

$$\nabla^2\psi = \omega. \tag{3.59}$$

on the interior grid points using the standard central differentiation

$$\Delta_h\psi^{n+1} = \omega^n. \tag{3.60}$$

Step 2: Compute the velocity

$$\mathbf{u} = \nabla^\perp\psi. \tag{3.61}$$

on the interior grid points using a standard central difference method

$$u^{n+1} = -\tilde{D}_y\psi^{n+1} \tag{3.62}$$
$$v^{n+1} = \tilde{D}_x\psi^{n+1}. \tag{3.63}$$

Step 3a: Compute the vorticity on walls using a second order Thomas' formula.

Step 3b: Update ω^{n+1} on the interior grid points

$$\frac{\partial\omega^{n+1}}{\partial t} + \mathbf{u}^{n+1} \nabla \omega^n = \nu\Delta\omega^n \tag{3.64}$$

using a standard Crank-Nicolson method which is of second order accuracy in space and time. The convective derivative $\mathbf{u} \bigtriangledown \omega$ is approximated using a upwind scheme. Taking $u\partial\omega/\partial x$ for example,

$$u_{i,j} > 0, \qquad \frac{\partial \omega}{\partial x} = \frac{\omega_{i+1,j} - \omega_{i-1,j}}{2h} + \frac{\omega_{i-2,j} - 3\omega_{i-1,j} + 3\omega_{i,j} - \omega_{i+1,j}}{6h} + O(h^3) \quad (3.65)$$

$$u_{i,j} < 0, \qquad \frac{\partial \omega}{\partial x} = \frac{\omega_{i+1,j} - \omega_{i-1,j}}{2h} + \frac{\omega_{i-1,j} - 3\omega_{i,j} + 3\omega_{i+1,j} - \omega_{i+2,j}}{6h} + O(h^3). \quad (3.66)$$

Note that the above finite difference approximations are of order h^3, they provide a more stable scheme than the three-point upwind scheme, for example,

$$u_{i,j} > 0, \qquad \frac{\partial \omega}{\partial x} = \frac{-\omega_{i+2,j} + 4\omega_{i+1,j} - 3\omega_{i,j}}{2h}. \quad (3.67)$$

3.4.2 EC4

The contents mainly follows E & Liu [8]. EC4 is an efficient numerical scheme to solve the NSE (3.1) for the driven cavity problem. This method is coupled with Runge Kutta method, and is fourth order in both space and time.

EC4 is based a reconstruction of the NSE. Using a fourth order operator on the transport equation (3.1)a, one has

$$\left(1 + \frac{h^2}{12}\Delta_h\right)\frac{\partial \omega}{\partial t} + \left(1 + \frac{h^2}{12}\Delta_h\right)(\mathbf{u} \cdot \bigtriangledown)\omega = \nu\left(\Delta_h + \frac{h^2}{6}D_x^2 D_y^2\right)\bigtriangledown^2 \omega + O(h^4) \quad (3.68)$$

with

$$\left(1 + \frac{h^2}{12}\Delta_h\right)(\mathbf{u}\cdot\bigtriangledown)\omega = \tilde{D}_x(1+\frac{h^2}{6}D_y^2)(u\omega)+\tilde{D}_y(1+\frac{h^2}{6}D_x^2)(v\omega)-\frac{h^2}{12}\Delta_h(u\tilde{D}_x\omega+v\tilde{D}_y\omega)+O(h^4). \quad (3.69)$$

Let $(1 + \frac{h^2}{12}\Delta_h)\omega = \bar{\omega}$, the algorithm of EC4 is listed as below

Initialization : Given ω^0, compute

$$(1 + \frac{h^2}{12}\Delta_h)\omega^0 = \bar{\omega}^0. \quad (3.70)$$

Advance the time from t_n to t_{n+1}

Step 1: Given ω^n, compute ω^{n+1} by

$$\frac{\bar{\omega}^{n+1}-\bar{\omega}^n}{\Delta t}+\bar{D}_x(1+\frac{h^2}{6}D_y^2)(u\omega)+\bar{D}_y(1+\frac{h^2}{6}D_x^2)(v\omega)-\frac{h^2}{12}\Delta_h(u\tilde{D}_x\omega+v\tilde{D}_y\omega)=\nu\left(1+\frac{h^2}{12}\Delta_h\right)\nabla^2\omega. \tag{3.71}$$

Step 2: Solve for ψ^{n+1} interior using

$$(\Delta_h+\frac{h^2}{6}D_x^2D_y^2)\psi^{n+1}=\bar{\omega}^{n+1}. \tag{3.72}$$

Step 3: Solve for ω^{n+1} interior using

$$(1+\frac{h^2}{12}\Delta_h)\omega^{n+1}=\bar{\omega}^{n+1}. \tag{3.73}$$

Step 4: Update velocity using

$$u^{n+1}=-\tilde{D}_y(1-\frac{h^2}{6}D_y^2)\psi^{n+1} \tag{3.74}$$

$$v^{n+1}=\tilde{D}_x(1-\frac{h^2}{6}D_x^2)\psi^{n+1}. \tag{3.75}$$

The order of accuracy of EC4 is checked for the driven cavity problem described in section 2. Figure 3.5a plots the maximum error at $t = 1$ in the stream function ψ, the velocity components u and v, and the vorticity ω, computed with various values of h=0.125, 0.0625, 0.03125, 0.015625, 0.0078125, and 0.00390625. The error is computed using the results with h=0.001953125 as the 'exact' solution. For reference, the time step used throughout is Δt=0.0025. The figure also plots a line of slope 4. Therefore, this figure shows that all four quantities converge to fourth order in space, as predicted theoretically by E & Liu.

Figure 3.5b shows the order of accuracy in time. It plots the maximum error at $t = 1$ in the same quantities, computed with Δt = 0.01, 0.005, 0.0025, 0.00125, 0.000625 and 0.0003125, where h=0.0078125. Here, the result with Δt = 0.000078125 is used as the 'exact' solution. The straight line has slope 4. Thus the figure shows that the method is fourth order accurate in time. Note that the curves in figure 3.5b level up when Δt is less than 0.00125, this is because either the spatial error dominates.

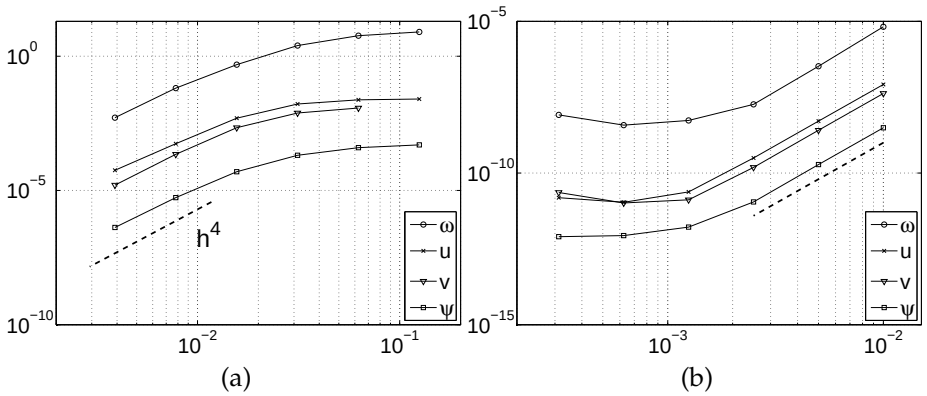

Figure 3.5: *(a)* Order of accuracy in space and *(b)* in time, using EC4. The y axis for both figures are the maximum errors over the whole domain. The x axis for *(a)* is h and for textit(b) is Δt.

3.4.3 Vortex sheet method

In the vortex sheet model the fluid is treated as a purely inviscid one. The plate is modeled as a bound vortex sheet that satisfies zero normal flow through the plate. A point vortex is released at each time step from the edges of the plate and the shed vorticity is modeled as a regularized free sheet [27]. A key component is the algorithm used to determine the shed circulation $\Gamma(t)$. Here, we follow [31] and impose the Kutta condition

$$\frac{d\Gamma}{dt} = -\frac{1}{2}(u_+^2 - u_-^2) \,, \tag{3.76}$$

where $u_\pm$ are the tangential velocities left and right of the plate, at the edge. An alternative method introduced by Jones [18] is based on representing the flow in the complex plane (see also [19, 41, 40, 2]). The vortex sheet model depends on the regularization parameter δ for the free sheet. For more details, see [31].

4 Determine the necessary resolution using FDMHS

For cases of the impulsively started flow past a plate, and flow past a semi-infinite plate, the initial flow is singular with unbounded velocity. It is difficult to accurately resolve these flows at small times. However, my results show that with sufficient resolutions in space and time, one actually can resolve the flow at any possible time. The earlier the time is, the higher resolutions are required; the larger the Reynolds number is, the higher resolutions are required. In this section, we are going to determine what are necessary resolutions in space and time for the flow at a given time of interest.

4.1 Effects of the resolution

Note that the thickness of the boundary layer is proportional to $\sqrt{vt}$. For a certain v, a necessary mesh size is required to represent the flow's structure. This is analogous to imposing a certain number of grid points per wavelength in Fourier analysis, in order to represent the wave.

Figure 4.1 shows vorticity contours for Re= 500 at t=0.05 using three different time steps Δt=0.0001, 0.0002, 0.0004, and four mesh sizes h = 0.0015625, 0.003125, 0.00625, 0.0125, for the problem of flow past a semi-infinite plate. Figure 4.1a shows the best result of all, it uses h = 0.0015625 and Δt=0.0002. The figures at the second row of figure 4.1 use the same h = 0.003125. There is a kink on the outer spiral, and this kink is getting worse with Δt becoming larger. The middle column of figure 4.1 show a comparison of results using a fixed Δt and increasing h (from top to bottom). At h=0.00625, a negative region appears along the outer turn and the profile of the outer vortex looks oscillatory. The negative region between the positive starting vortex and the plate has an irregular shape. h=0.0125 gives the worst result. The region of negative vorticity right above the plate disappears.

Figure 4.2 shows vorticity contours for Re=500 at t=0.05 for the problem of impulsively started flow past a finite plate. Four mesh sizes are used, and the time step is chosen small enough such that vorticity contours do not get a lot better by eye (in terms of the smoothness of the contours). It occurred to me that the computation for a fixed h is stable for a certain range of Δt. Too large Δt yields instability and too small Δt yields incorrect flow behavior. Figure 4.2ab seem to represent the vorticity well and show no apparent difference. The instability appears in figure 4.2c with a mesh size h=0.003125, and the instability gets worse in figure 4.2d with a mesh

size h=0.00625. Therefore, one can say that a necessary mesh size of h=0.0015625 is needed to resolve the vorticity at t=0.05 for Re=500. An example about the effect of time step is shown in figure 4.3. This figure plots vorticity contours for Re=500 at t=0.05 as well, the mesh size is fixed at h=0.003125. Three time steps are chosen, $\Delta t = 1 \times 10^{-4}$, $\Delta t = 2 \times 10^{-4}$ and Δt=2.5×10^{-4}. All three figures have instabilities, as Δt gets bigger, the instability gets worse.

Therefore, our approach to determine if the flow is well resolved or not in the computation is that if h is further refined, there are no visible changes. More concisely, we will use enough number of grid points such that the flow looks like resolved as shown in figure4.1a and figure 4.2ab for the given time of interest.

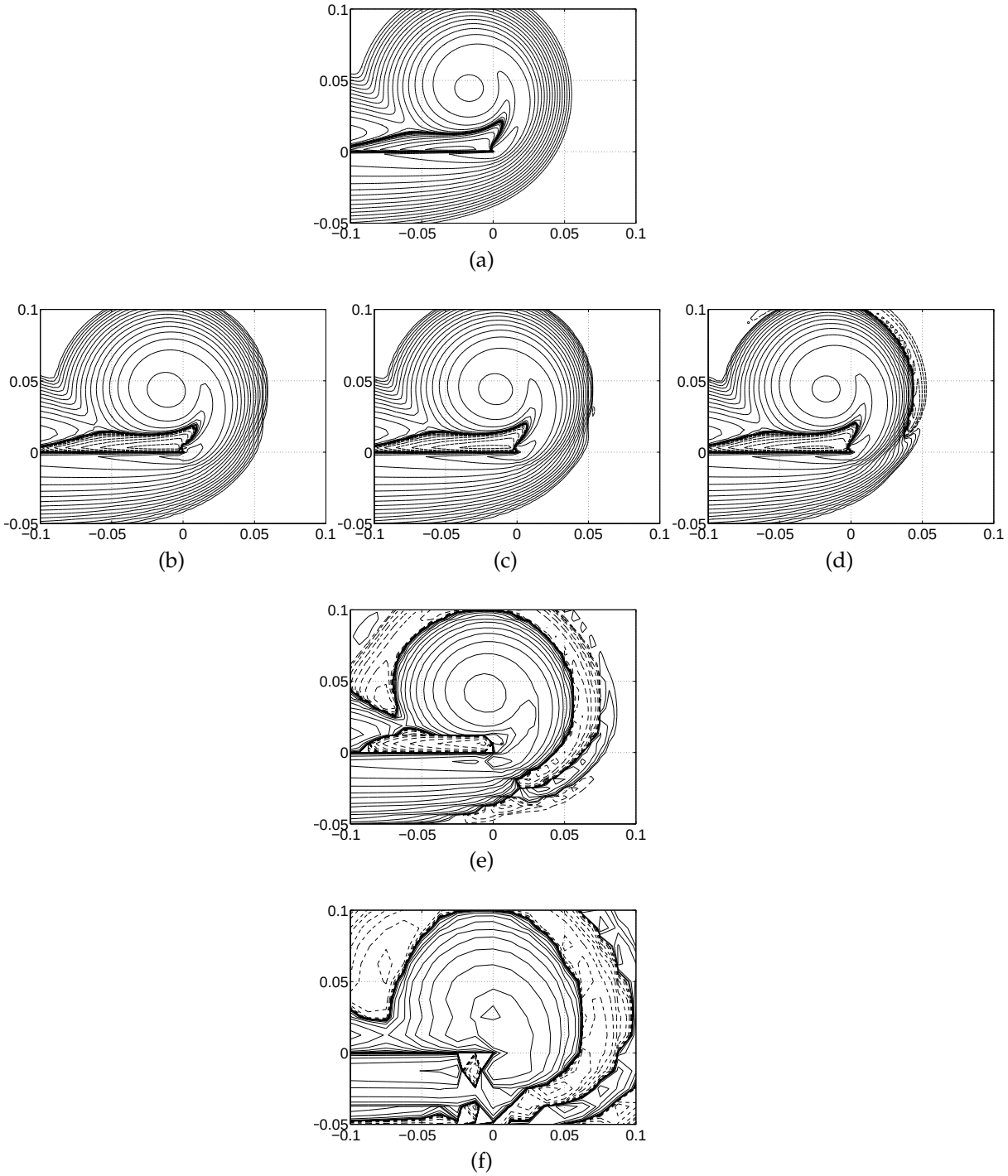

Figure 4.1: Vorticity contours for Re=500 at t =0.05 for the problem of flow past a semi-infinite plate. The spatial mesh size and temporal step are (a) h=0.0015625, Δt=0.0001, (b) h=0.003125, Δt=0.0001, (c) h=0.003125, Δt=0.0002, (d) h=0.003125, Δt=0.0004, (e) h=0.00625, Δt=0.0002, (f) h=0.0125, Δt=0.0002, (g) h=0.0015625, Δt=0.0001. The contour levels of the vorticity are $\pm 2^{[-8:8]}$. The vorticity is negative in dashed lines and the positive in solid line.

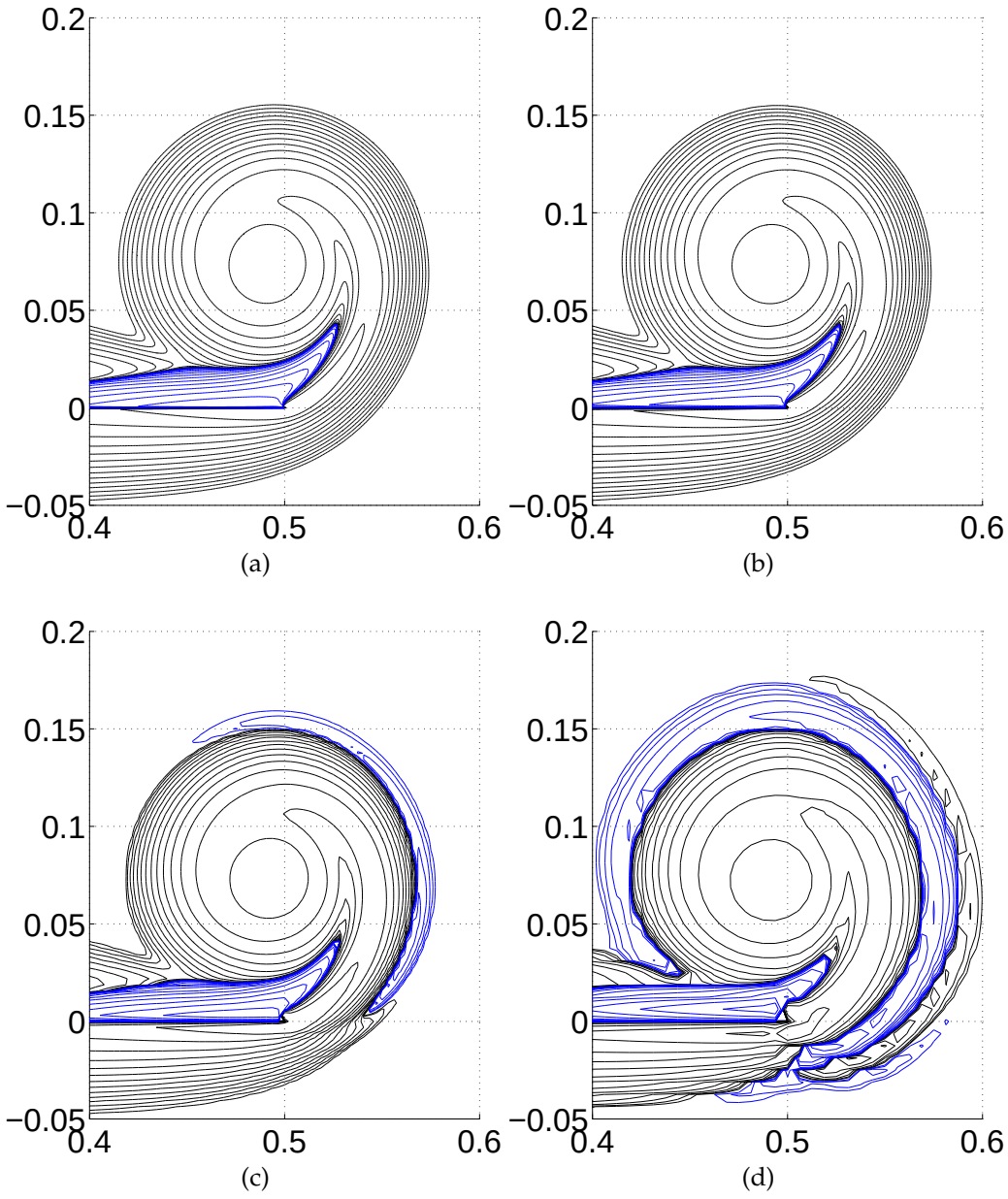

Figure 4.2: Vorticity contours at t=0.05 for Re=500 for the problem of impulsively started flow past a finite plate. The mesh size and time step is *(a)* h=0.00078125, $\Delta t = 5\times10^{-5}$, *(b)* h =0.0015625, $\Delta t = 1\times10^{-4}$, *(c)* h =0.003125, Δt=2×10^{-4}, *(d)* h =0.00625, Δt=4×10^{-4}. $\omega = \pm 2^{[-5:12]}$.

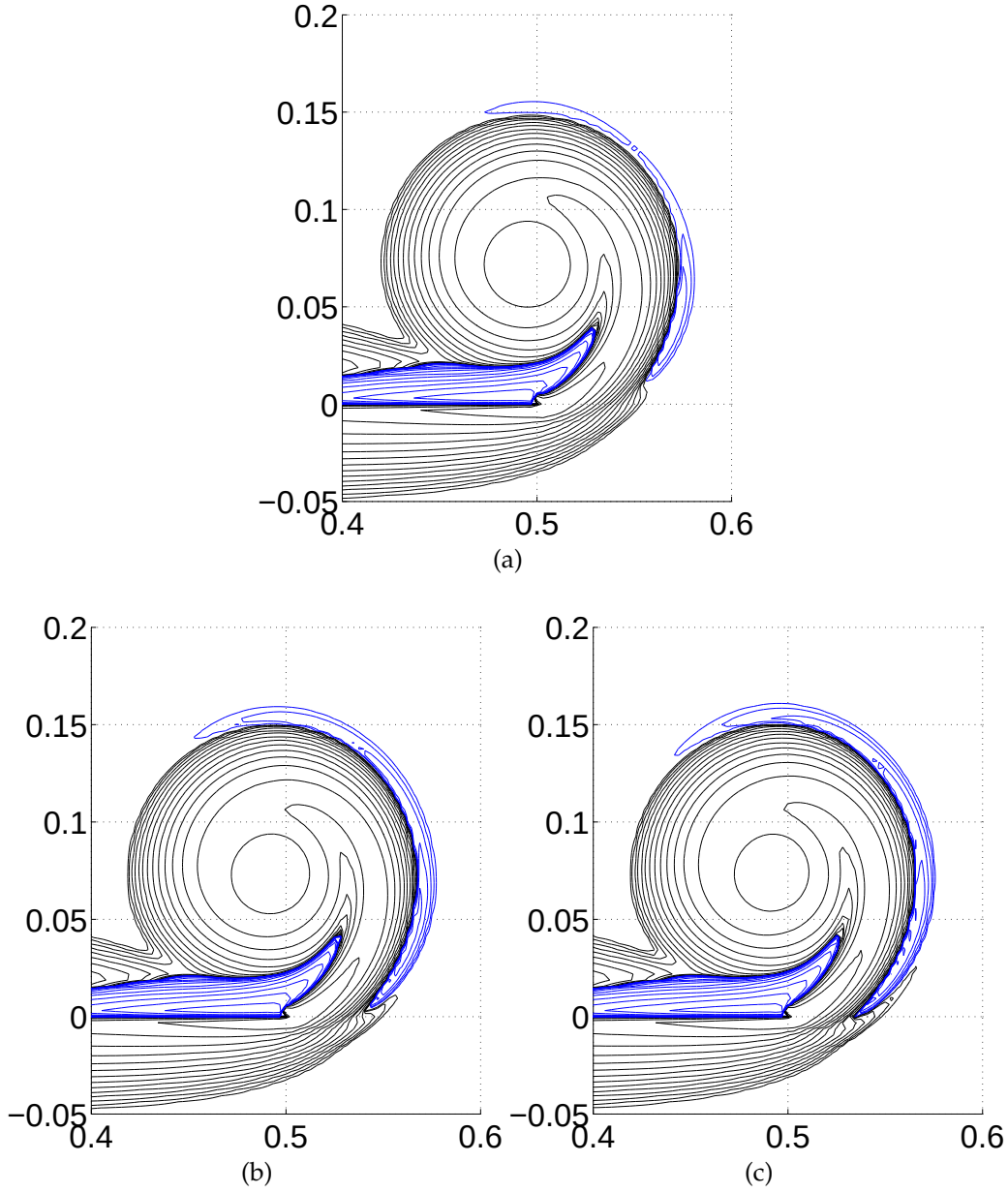

Figure 4.3: Vorticity contours at t=0.05 for Re=500, h = 0.003125 for the problem of impulsively started flow past a finite plate. The time step is *(a)* $\Delta t = 1 \times 10^{-4}$, *(b)* $\Delta t = 2 \times 10^{-4}$, *(c)* Δt=2.5×10^{-4}. $\omega = \pm 2^{[-5:12]}$.

4.2 The resolution for Re=500

The computations show that in order to resolve the flow for a larger Reynolds number than Re=500 or at a smaller time than t=0.05, the mesh size h and time step Δt are required to be smaller than h=0.0015625 and $\Delta t = 1 \times 10^{-4}$. In other words, the requirement on h and Δt can be lessened if one is interested in results for a small Reynolds number or at a large time. One numerical evidence is shown in figure 4.4. This figure plots the maximum velocity U_{max} vs.t for Re=500 using four mesh sizes, h=0.00078125, h=0.0015625, h=0.003125 and h=0.00625. The time period is from 0 to 0.04. Plots of figure 4.4bcd are closeups of figure 4.4a at three different time intervals. In figure 4.4a, the U_{max} at all h's are not smooth initially, that is the 'early time stage' at which the flow can not be resolved using these h's. As t increases, the U_{max} using these h's start to converge (overlap), and the convergence is at different times for different h's. Taking the result of h=0.00078125 as the 'exact' solution, the solution of h=0.0015625 overlaps the 'exact' solution around $t = 1 \times 10^{-3}$ as shown in figure 4.4b, the time is around $t = 2 \times 10^{-3}$ for h=0.003125 as shown in figure 4.4c and around $t = 4 \times 10^{-3}$ for h=0.00625 as shown in figure 4.4d. To be more precise, the relative errors at h=0.0015625, h=0.003125 and h=0.00625 are computed as below

$$\text{relative error} = \frac{U_{max} - U_{max}^{ex}}{U_{max}} \tag{4.1}$$

and results are listed in table 4.1. For each row, h is fixed and t varies, the relative error decreases as t increases. In each column, t is fixed and h varies, a small h has a small relative error.

	t= 0.01	t=0.02	t=0.04
h= 0.0015625	0.0084	0.0031	0.0001
h= 0.003125	0.1424	0.0125	0.0034
h=0.00625	0.1582	0.0898	0.0231

Table 4.1: Relative errors in U_{max} using (4.1).

Two other h's are used in computations as well, they are h=0.0001953125 and h=0.000390625. Figure 4.5 plots the corresponding U_{max} vs. t. Since the runtime is expensive for these two h's, the time period is from 0 to 0.0025 for h=0.0001953125 and from 0 to 0.0005 for h=0.000390625. Taking the result of h=0.00078125 as the 'exact' solution again, the solution of h=0.0001953125 overlaps the 'exact' solution at around $t = 2 \times 10^{-4}$ as shown in figure 4.5a and for h=0.000390625, the error seems quite small after the time $t = 2.5 \times 10^{-3}$ as shown in figure 4.5b.

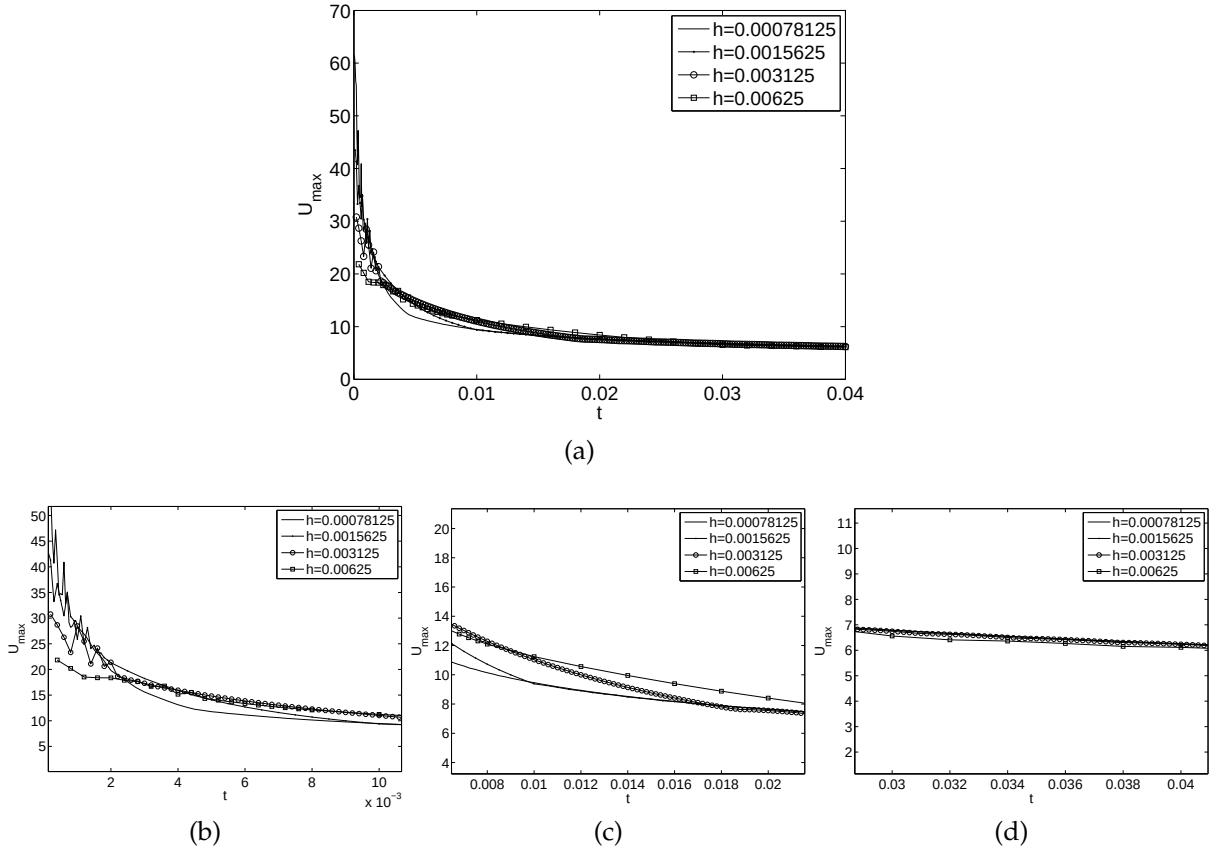

Figure 4.4: Maximum velocity U_{max} vs. t for Re =500 using four mesh sizes, h=0.00078125, h=0.0015625, h=0.003125 and h=0.00625. The time steps are $\Delta t = 5\times10^{-5}$, $\Delta t = 1\times10^{-4}$, $\Delta t = 2\times10^{-4}$ and $\Delta t = 4\times10^{-4}$, respectively. Plots of *(b)(c)(d)* are closeups of *(a)* over three different time intervals.

The singular behavior of the flow can be seen in U_{max} as well. Table 4.2 gives the maximum velocity using six mesh sizes. Note that the time step Δt is generally different for each h, for some h's, two Δt's are used. These computations are stable. It is stressed that U_{max} is as large as 396 at t=1 $\times$ 10^{-}6 using h=0.0001953125. For a large h or Δt, the solution is more dissipative, which results in a relatively smaller U_{max}. Therefore, the conditions on h and Δt are more severe if one wants to resolve the flow at an early time.

Both velocity and vorticity have large gradients in the neighborhood of the plate tip, the maximum vorticity, in the absolute value, is found near the tip for all Reynolds numbers at all time. Figure 4.6 is a closeup of vorticity contours near the plate tip for Re=500 at t=0.01. Results at three resolutions are plotted, h = 0.003125, 0.0015625 and 0.00078125. These figures show that vorticity of zero level (the thick

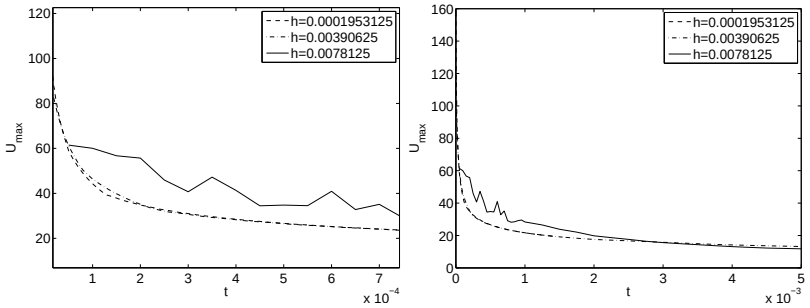

(a) (b)

Figure 4.5: Maximum velocity U_{max} vs.t for Re =500 using three mesh sizes, h=0.0001953125, h=0.000390625 and h=0.00078125. The time steps are $\Delta t = 2\times10^{-6}$, $\Delta t = 4 \times 10^{-6}$ and $\Delta t = 5 \times 10^{-5}$, respectively. Plots of *(b)* is a closeup of *(a)* in a smaller time interval.

h	Δt	U_{max}
0.0001953125	1×10^{-6}	396
0.0001953125	2×10^{-6}	157
0.000390625	4×10^{-6}	111
0.00078125	1×10^{-5}	61
0.00078125	5×10^{-5}	61
0.0015625	2×10^{-5}	43
0.0015625	1×10^{-4}	43
0.003125	2×10^{-4}	30
0.00625	4×10^{-4}	21

Table 4.2: U_{max} at Δt for different h's.

line) converges to a curve, this curve divides the positive and negative vorticity. It is stressed that the region of positive vorticity is being entrained by the negative one, and the region of negative vorticity is being entrained by the positive one as well. Such a flow feature has not been reported before, and more details about it will be discussed in section 6.

The plate emanates vorticity, The amount of vorticity entering the flow differs at different locations on the plate. The vorticity values on the plate are different from above and below the plate. Figure 4.7 shows the vorticity values along the plate, both from above and below. Three resolutions are used, h = 0.003125, 0.0015625 and 0.0078125, and their results converge in general except for a region near the plate tip. It is stressed that the vorticity value goes extremely large near the tip.

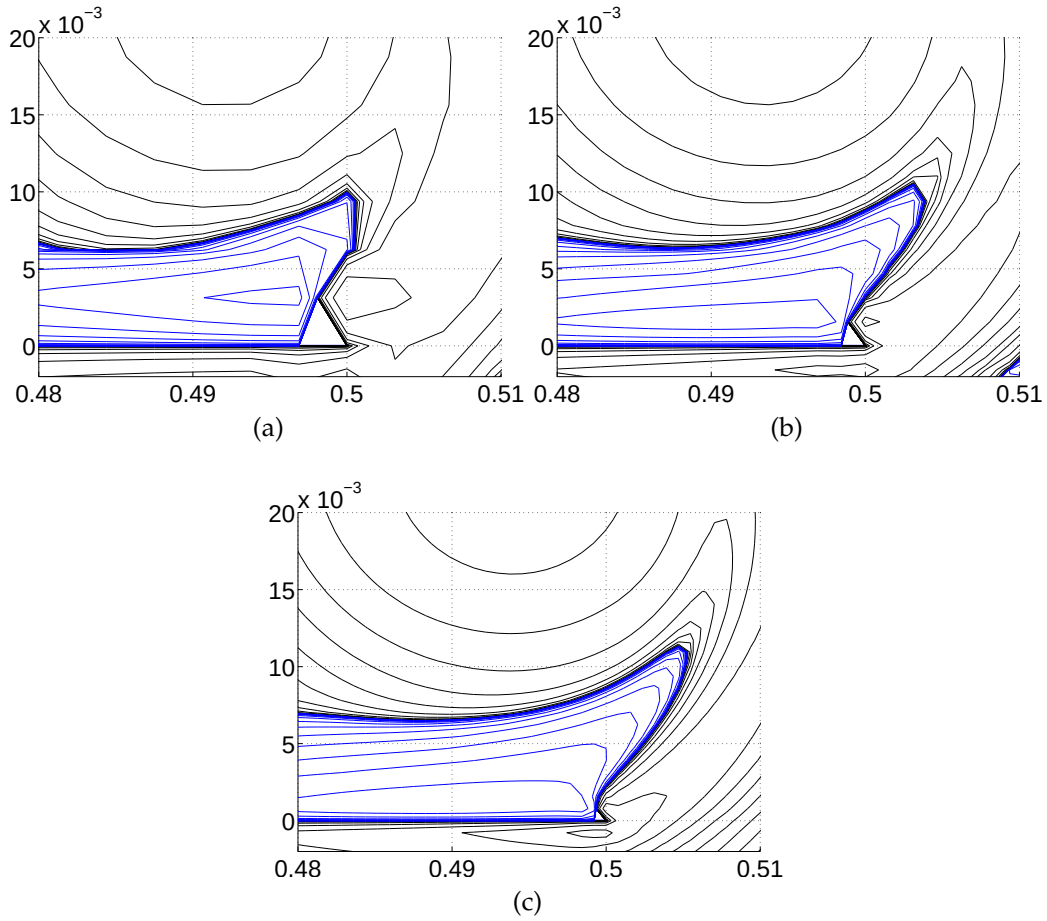

Figure 4.6: vorticity contours near the tip for Re=500 at t=0.01. Three resolutions are used with *(a)* h=0.003125, *(a)* h=0.0015625 and *(a)* h=0.00078125. $\omega = \pm 2^{[-5:12]}$.

The conclusion for this section is that impulsively started flow past a finite plate is the most difficult one in computation, compared to the uniformly accelerated flow where the flow velocity is continuous at t=0. The velocity for the impulsively started flow is a heavy-side function with the discontinuity at t=0. The background flow velocity is zero at t=0, and the velocity is a nonzero constant when $t \neq 0$. One can resolve the flow outside a time neighborhood of t=0 and a space neighborhood of the plate tip for a given time-space resolution.

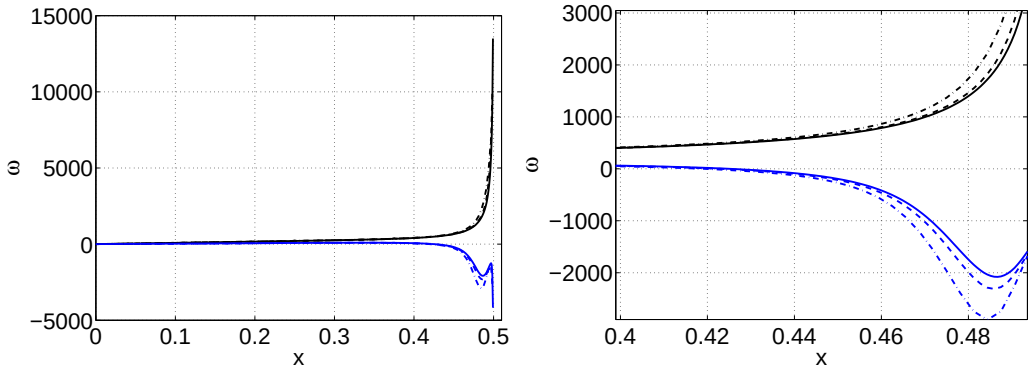

(a) (b)

Figure 4.7: Vorticity values along the plate for Re=500 at t=0.01. *(b)* is a closeup of *(a)* near the plate tip. These curves that have negative values are from above the plate, the other ones are from below the plate. h=0.003125 (dot-dashed line), h=0.0015625 (dashed line) and h=0.00078125 (solid line)

4.3 The resolution for other Reynolds numbers

Based on the relation of boundary layer thickness $\delta \sim \sqrt{\nu t}$, one fixes t and reduces ν by four times to $\nu' = \nu/4$, the layer thickness is reduced by a half, reaches to $\delta' \sim \delta/2$. Keeping the same the number of grid points across the boundary layer, the mesh size for ν' at t halves, which gets to $h' = h/2$. We take plots of the stream function for Re=500 and 2000 for example, t=1. Note that for the finite plate case, ν=0.002 corresponds to Re=500 and ν=0.0005 corresponds to Re=2000. Figure 4.8ab plot the stream function along the line x=0.5, $y \in [-0.2, 0.2]$ for Re=500 and 2000. Three mesh sizes are used, h=0.00625, h=0.003125 and h=0.0015625. Using the solution at h=0.0015625 as the 'exact' one, figure 4.8cd plot the maximum errors along the line for Re=500 and 2000, respectively. The maximum errors for Re=2000 using h=0.003125 is comparable to that for Re=500 using h=0.00625. Therefore, one can say that a necessary mesh size of h=0.003125 is required to resolve the flow for Re=500 at t=0.01.

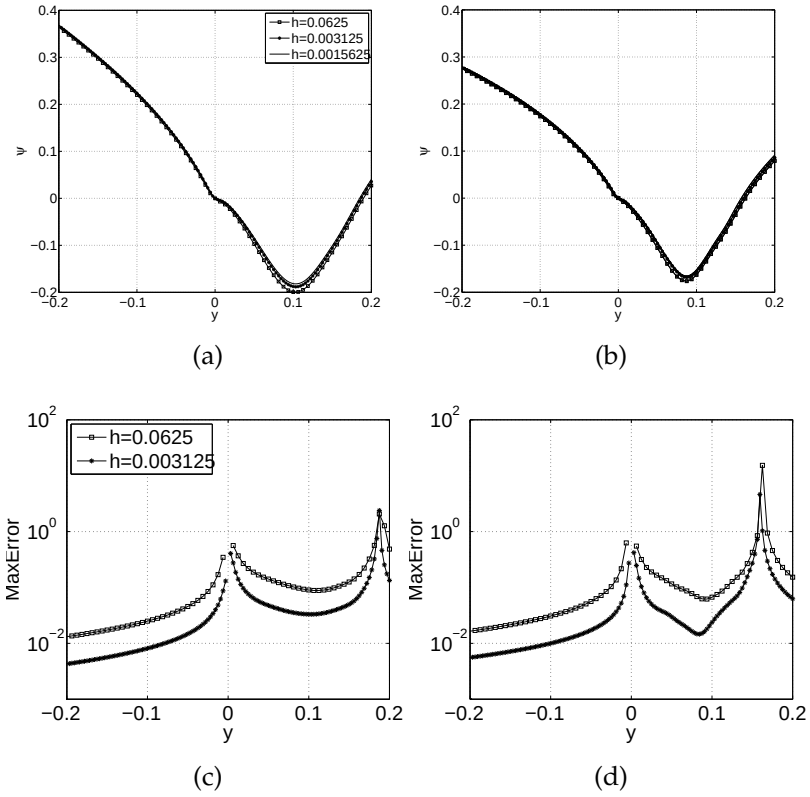

Figure 4.8: Plots of the stream function along the line $x = 0.5$, $y \in [-0.2, 0.2]$ for (a) Re=500 and (b) Re=2000. Three different mesh sizes are used, $h = 0.00625$, $h = 0.003125$ and $h = 0.0015625$. Using results of h=0.0015625 as the 'exact' solution, the maximum errors in the stream function along the line $x = 0.5$,$y \in [-0.2, 0.2]$ for (c) Re=500 and (d) Re=2000. t=0.1.

5 Determine the order of accuracy of FDMHS

This section presents the order of accuracy of FDMHS for both the driven cavity problem and the flow past a finite plate. We plotted the maximum norm of errors in the stream function, velocity and vorticity. In particular, we compare results of vorticity contours between FDMHS, EC4 and FDM2. For the problem of flow past a finite plate, since the flow is singular at the plate tip, the convergence rate is not expected to be the same as that in the driven cavity problem. We plotted the values of stream function along a line crossing the plate, as well as its maximum norm of errors to test the order of accuracy. We also compute the relative errors in the vortex core trajectory and vorticity.

5.1 Driven Cavity

Here we present results for driven cavity problem with smooth driving velocity, section 2, for various Reynolds numbers, where the characteristic length L is the length of one side of the cavity wall, the characteristic velocity is given by the driving velocity, see (2.3).

5.1.1 Order of accuracy

Figure 5.1 shows the convergence in time for Re=100. Nine time steps are used, Δt = 0.0025 0.002 0.00125 0.001 0.0008 0.0005 0.0004 0.0002 and 0.0001. The mesh size is h = 0.015625. The computation for each Δt ends at t = 1. The result of Δt=0.0001 is used as the 'exact' solution. In figure5.1, the y axis is the maximum norm of errors in the computational domain, x axis is the time step Δt. The dashed line is a straight line of slope 1. Note that FDMHS is formally second order in time. However, all four flow quantities, vorticity, horizontal velocity, vertical velocity and stream function here show first order of accuracy in time. The slope of at the very left line segment for each quantity is about 1.5. This is caused by the simple splitting scheme, and the semi-Lagrangian method. Typical examples about the order of accuracy in time for semi-Lagrangian methods are provided by Falcone and Ferretti [13]. In their work, they examined the convergence, stability and accuracy for a class of high-order semi-Lagrangian advection schemes. The reason why I use a second order semi-Lagrangian scheme in time though the convergence study shows a first order is because that, the second order method allows a larger

time step and the accuracy can be better in solutions compared with that using a first order method.

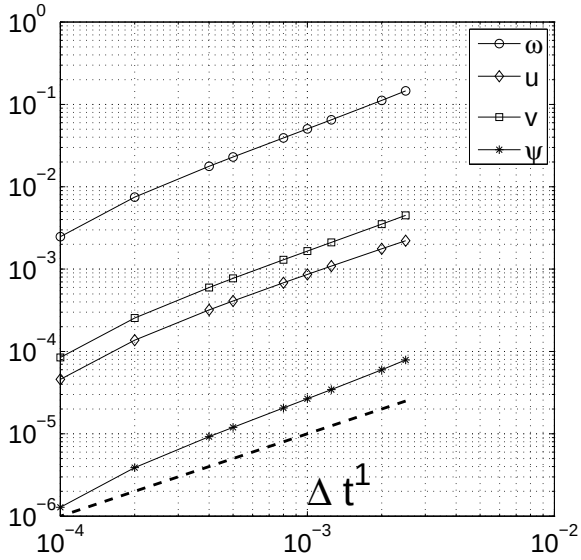

Figure 5.1: Order of accuracy in time of FDMHS in driven cavity problem. Nine time steps are used, Δt = 0.0025 0.002 0.00125 0.001 0.0008 0.0005 0.0004 0.0002 and 0.0001. The mesh size is h = 0.015625. The computation for each Δt ends at t = 1. The result of Δt=0.0001 is used as the 'exact' solution. The horizontal axis is the time step Δt, and the vertical axis is the error which is measured in the maximum norm over the whole domain.

Figure 5.2 examines the order of accuracy in space. Five mesh sizes are used, h = 0.125, 0.0625, 0.03125, 0.015625, 0.0078125 and 0.00390625, t=0.004. The time step is $\Delta t = 10^{-6}$. The time step is small enough that the error in space dominates. The results of h=0.00390625 are used as the 'exact' solution. Figure 5.2a shows results of FDM2. The dashed line is a straight line of slope 2. In this figure, the stream function, velocity and vorticity all show second order convergence. Figure 5.2b uses FDMHS. The dashed lines are straight lines of slope 3 and 4, respectively. In this figure, the stream function and velocity show fourth order convergence. But the vorticity is close to third order (the slope is about 3.2 in the last line segment for vorticity). Figure 5.2c uses FDMHS as well. The curves of ψ, u and v are identical in figure 5.2b and figure 5.2c, but curves for ω are different. In figure 5.2c the order of accuracy in vorticity is close to fourth order (the slope is about 3.6 in the last line segment for vorticity). The region over which the errors are computed is different between figure 5.2b and figure 5.2c. The errors over the whole computational domain are considered in figure 5.2b while the errors in small regions on the top left and right corners are excluded, in figure 5.2c. The flow on the top two corners has large velocity gradients and a large amount of vorticity is concentrated there.

ψ	u	v	ω	$\omega*$
0.76	-0.12	0.33	0.56	0.70
1.09	0.17	0.51	2.81	2.18
2.63	1.51	1.72	-0.23	0.20
5.46	4.09	4.06	3.36	3.63

Table 5.1: The slopes of line segments in figure 5.2bc. Vorticity ω is for figure 5.2b and vorticity $\omega*$ is for figure 5.2c.

Table 5.1 lists the order of convergence for figure 5.2bc. Note the truncation errors using FDMHS is generally smaller than that using FDM2.

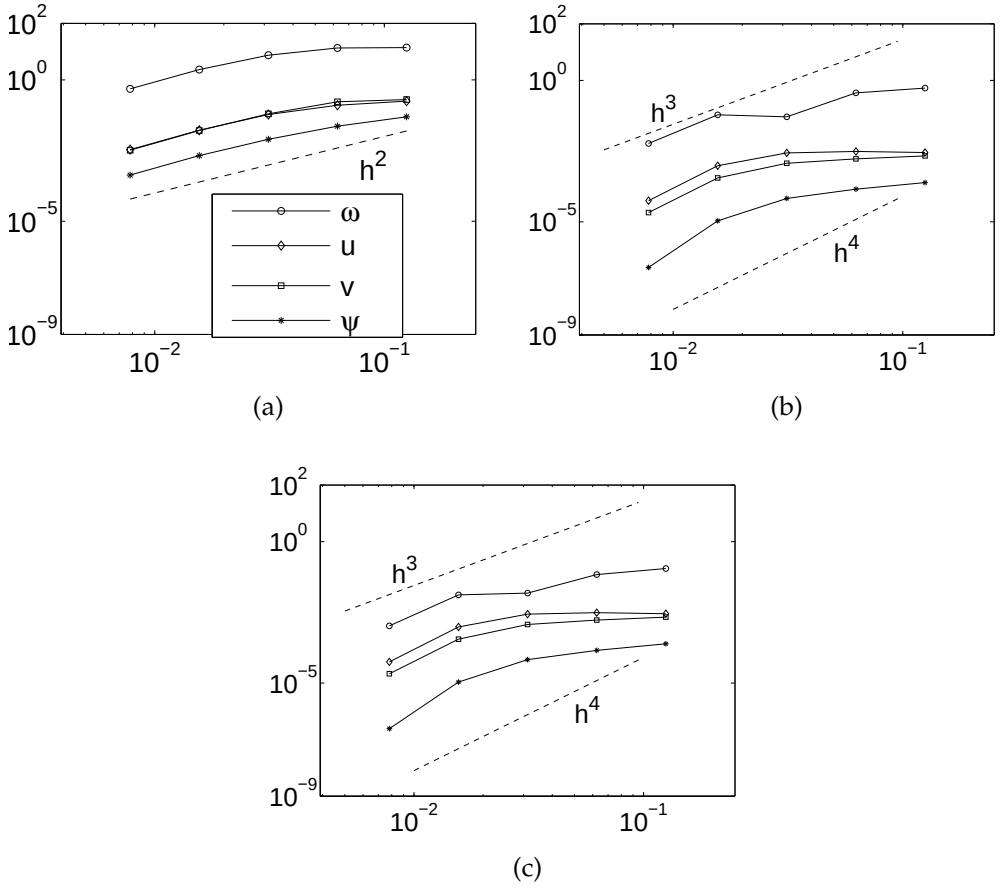

Figure 5.2: Order of accuracy of FDM2 and FDMHS in the driven cavity problem. The computation uses *(a)* FDM2, *(b)* FDMHS, and *(c)* FDMHS. Six mesh sizes are h = 0.125, 0.0625, 0.03125, 0.015625, 0.0078125 and 0.00390625. The results of h=0.00390625 are used as the 'exact' solution. The horizontal axis is the mesh size h, and the vertical axis is the error which is measured in the maximum norm. The curves of ψ, u and v are identical in*(b)* and *(c)*, but curves for ω are different. In *(b)*, the errors over the whole computational domain are considered, and in *(c)*, errors over the whole domain but excluding the regions of two top corners, are considered.

5.1.2 Comparisons with other methods

Figure 5.3 compares FDM2 and FDMHS in vorticity contours for Re=10,000 at t=1. Both methods use the same coarse mesh sizes h=1/96, and the time step Δt is sufficiently small that the errors in space dominate. Figure 5.3a shows vorticity contours using FDM2, and figure 5.3b uses FDMHS. Figure 5.3cd are closeup of figure 5.3ab, respectively. It is stressed that, on the top right corner of the cavity, FDM2 shows jagged contours , while FDMHS does not. Therefore, one can say that FDMHS resolves the boundary layers better that of FDM2. Note, I am not not looking at the convergent results of FDMHS and FDM2 here. I also implemented EC4 [8] in the driven cavity problem. Figure 5.4 shows the comparison in vorticity contours and instantaneous streamlines between EC4 and FDMHS for Re=1000 at $t = 1$. The mesh size is h=1/512, and the time step Δt is small enough that the figures will not change if using a finer Δt. Figure 5.4ab show vorticity contours and instantaneous streamlines using FDMHS, respectively. Figure 5.4cd show vorticity contours and instantaneous streamlines using EC4, respectively. These two methods, FDMHS and EC4, show great agreement.

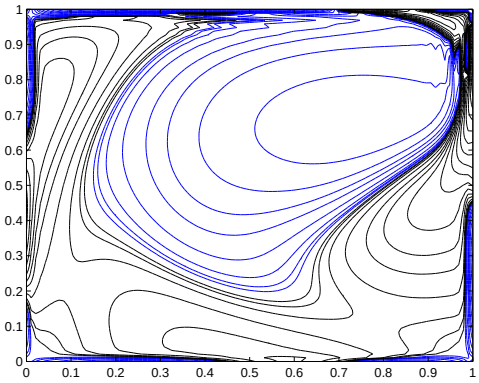

(a) FDM2

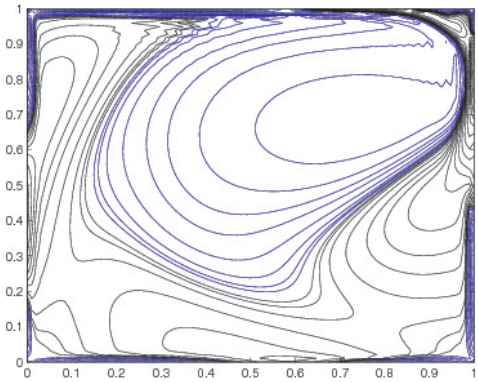

(b) FDMHS

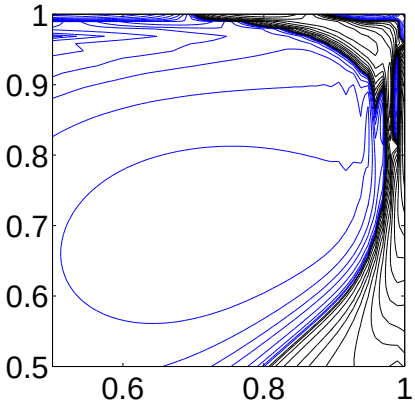

(c) FDM2 zoom in

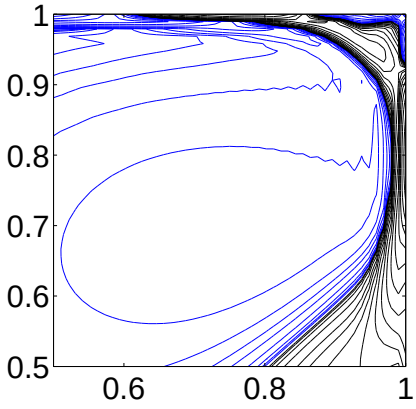

(d) FDMHS zoom in

Figure 5.3: The comparison between FDMHS and FDM2 in vorticity contours for Re=10,000 at t=1. *(a)* Vorticity contours using FDM2, *(b)* Vorticity contours using FDMHS. *(c)(d)* are closeup for *(a)(b)*, respectively. Both methods use the same coarse mesh sizes h=1/96, and the time step Δt is sufficiently small that the errors in space dominate.

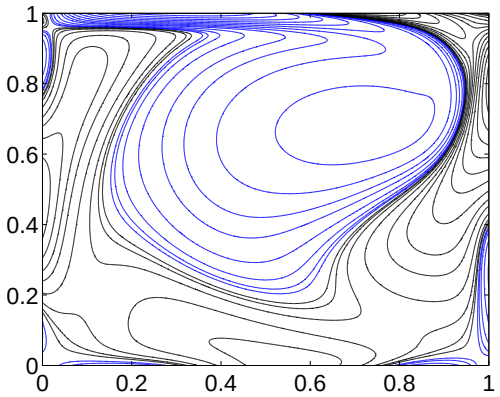

(a) FDMHS ω

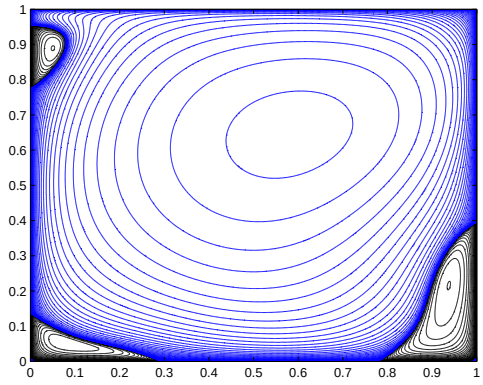

(b) FDMHS ψ

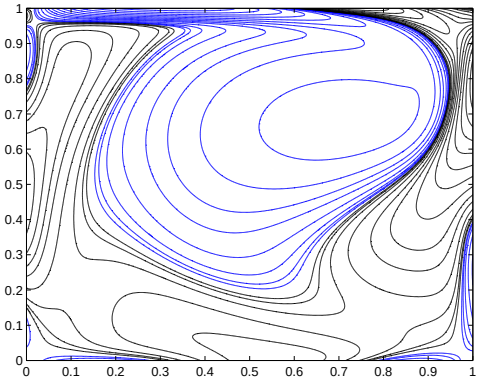

(c) EC4 ω

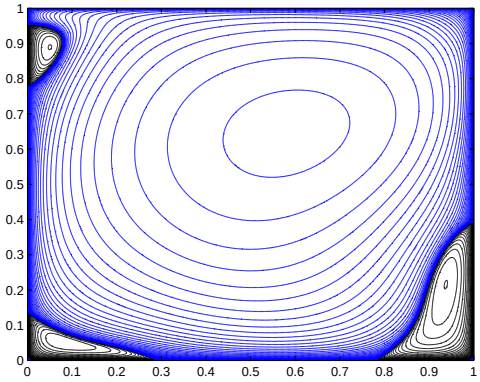

(d) EC4 ψ

Figure 5.4: The comparison between FDMHS and EC4 in vorticity contours and instantaneous streamlines for Re=1000 at t=1. *(a)* Vorticity contours and *(b)* instantaneous streamline using FDMHS. *(c)* vorticity contours and *(d)* instantaneous streamline using EC4. The mesh size is h=1/512, and the time step Δt is small enough that the figures will not change if using a finer Δt.

5.2 Finite Plate

5.2.1 Order of accuracy in space

The order of accuracy of FDMHS in space is examined here for the problem of impulsively started flow past a finite plate. The Reynolds number is 500 for all the results in this section.

Figure 5.5 shows the instantaneous streamlines at t=0.04. We try to establish the order of accuracy by looking at values of stream function in a region nearby the plate tip. Figure 5.6a shows the values of the stream function along a line crossing the plate tip, x=0.5, $y \in [-0.25, 0.25]$. Four different mesh sizes are used h=0.00625, h=0.003125, h=0.0015625 and h=0.00078125. At the scale shown in this figure, it is hard to see any difference for various h's. Using the result of $h = 0.00078125$ as the 'exact' solution ψ_{ex}, the errors in the other three mesh sizes are computed as below,

$$\text{error} = |\psi(0.5, y) - \psi_{\text{ex}}(0.5, y)|, \quad -0.25 \le y \le 0.25. \tag{5.1}$$

and plotted in figure 5.6b. One can see that the errors decrease as the mesh size decreases, and the errors are largest near the plate tip at $y = 0$. Table 5.2 gives the maximum errors $\text{error}_{\text{max}}$ over y of figure 5.6b. It shows that the order of accuracy in space is between one and two.

$$\text{error}_{\text{max}} = \max|\psi(0.5, y) - \psi_{\text{ex}}(0.5, y)|, \quad -0.25 \le y \le 0.25. \tag{5.2}$$

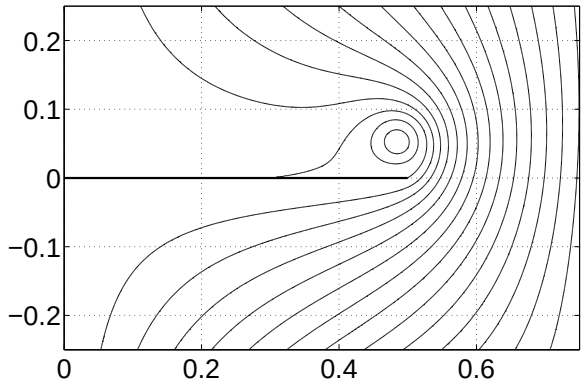

Figure 5.5: Instantaneous streamlines for Re=500 at t=0.04.

Figure 5.7 shows vorticity contours at t=0.04. We also try to establish the order of accuracy by looking at the vortex core trajectory and vorticity. In the figure, a large vortex spiral has formed above the plate tip. The thick curve is actually composed

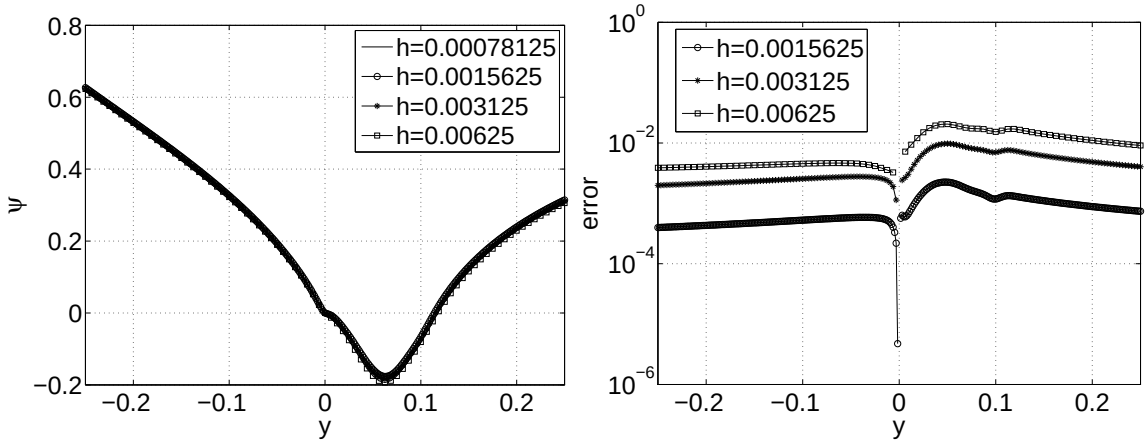

Figure 5.6: *(a)* The values of the stream function along the line $x = 0.5$, $y \in [-0.25, 0.25]$. Four different mesh sizes are used, h=0.00625, h=0.003125, h=0.0015625 and h=0.00078125. *(b)* absolute errors in the stream function along the same line. Using h=0.00078125 as the 'exact' solution. Re=500, t=0.04.

h	$\text{error}_{\max}$
0.00625	0.0206
0.003125	0.0098
0.0015625	0.0022

Table 5.2: Maximum errors in the stream function along the line $x = 0.5$, $y \in [-0.25, 0.25]$ for Re=500. The result at $h = 0.00078125$ is used as the 'exact' solution.

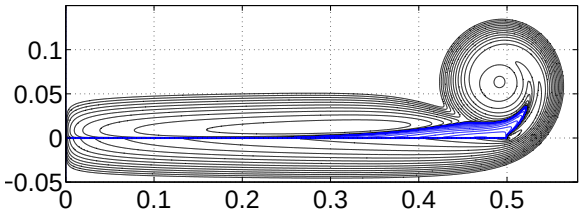

Figure 5.7: Vorticity contours for Re=500 at $t = 0.04$.

of vorticity contours with contour levels close to 0. The thick curve divides regions of positive and negative vorticity. The vorticity is negative in the a region bounded by the curve and the plate, and positive elsewhere. The vortex core is defined to be the point of maximum vorticity above the region of negative vorticity. Note that the vortex core is not the point of maximum vorticity globally. There are two other large local maxima near the tip, one positive and one negative. Table 5.3 gives

the coordinates of the vortex core (x_c, y_c), as well as the vorticity ω_c at the vortex core at t=0.04. Four mesh sizes are used, h=0.00625, h=0.003125, h=0.0015625 and h=0.00078125. The locations of the vortex core have good agreement. Using the solution at h=0.00078125 as 'exact' solution, define the relative error in vorticity e_ω and locations of core e_{core} as as

$$e_\omega = \frac{|\omega_c - \omega_{\text{ex}}|}{|\omega_{\text{ex}}|}, \qquad e_{\text{core}} = \frac{||\mathbf{z}_c - \mathbf{z}_{\text{ex}}||_2}{||\mathbf{z}_{\text{ex}}||_2} \tag{5.3}$$

where $\mathbf{z}_c = \langle x_c, y_c \rangle$. The last two columns of table 5.3 shows the relative errors of e_ω and e_{core} at h=0.00625, h=0.003125 and h=0.0015625. The relative errors in ω is roughly halved each time when h is halved. Therefore, a first order accuracy is achieved in the values of the vortex core, thought errors in the locations of vortex core hardly changes using h=0.003125 and 0.0015625.

h	(x_c, y_c)	ω_c	e_{core}	e_ω
0.00625	(0.4937, 0.0625)	527	0.0046	0.0645
0.003125	(0.4906, 0.0625)	548	0.0016	0.0237
0.0015625	(0.4921, 0.0625)	557	0.0014	0.0072
0.00078125	(0.4914, 0.0625)	561		

Table 5.3: Trajectory (x_c, y_c) and values ω_c of the vortex core for Re=500 at t=0.04. Using the solution at h = 0.00078125 to be the 'exact' value.

At the end of this section, I conclude that the order of accuracy of FDMHS is formally in fourth in space and two in time. According to results shown in the driven cavity test, FDMHS is fourth order accuracy in space and first order accuracy in time. In the problem of flow past a finite plate, FDMHS is between first and second order in space. FDMHS is an enhancement of FDM2, and resolves the flow as well as EC4.

6 Viscous flow past a finite plate

This section presents numerical simulations of the viscous flow past a finite plate, computed using FDMHS. In all cases, the parameters h and Δt are chosen according to the criterion presented in section 4.

6.1 Impulsive start

Impulsively started flow have applications in real life situations, for example, the sudden occurrence of force exerted on an object, a gust of wind blowing a tree. In some cases, the force or wind that come on a sudden are particularly destructive. This section presents results of the viscous flow past a finite plate with an impulsively started velocity

$$U_\infty(t) = 1. \tag{6.1}$$

The Reynolds number $Re = LU/\nu$ is obtained using the length of the plate as the characteristic length, and the far-field velocity U_∞ as the characteristic velocity. Sections 6.1.1 and 6.1.2 show the evolution of flow, from a very early time t=.0002 to a relatively large time t=5, and presents the dependence of the flow on Re. For Re=4000, an instability is observed in the form of secondary vorticies along the outer spiral turn. These are presented in section 6.1.3. The last sections, from 6.1.4 to 6.1.6 present global quantities such as characteristic width and height of the vortical region, the core trajectory and maximum vorticity, and the circulation and circulation shedding rate.

6.1.1 Evolution at an early time

Figure 6.1 shows the vorticity contours for Re=500 at a sequence of times at t = 0.0002, 0.0004, 0.001, 0.002, 0.004, 0.005, 0.01 and 0.02. The mesh size $h = 0.000390625$ for results at t = 0.0002, 0.0004, 0.001 and h = 0.00078125 for results at t = 0.002, 0.004, 0.005, 0.01, 0.02. The vorticity on the plate is not zero, but I make it zero for the plot purpose.

As the background flow moves from bottom to top, a boundary layer of positive vorticity forms on either side of the plate. This boundary layer is clearly visible already at the first time shown, t=0.0002. However, immediately after the beginning

of the motion the boundary layer loses its symmetry. Boundary vorticity from the bottom layer moves around the tip of the plate and concentrates near the edge above plate. This region of concentrated vorticity, referred to here as the starting vortex, grows in time, as does the boundary layer thickness. The figure shows positive and negative vorticity contour levels, $\omega = \pm 2^{[-5:12]}$. At the later times shown in figure 6.1, one observes what appears to be a thick contour level beginning at the tip and attaching back to the plate somewhere downstream of the tip. This thick curve consists in reality of large number of contours of near zero vorticity, and separates a region of negative vorticity, between the zero-level contour and the plate, and positive vorticity, everywhere else. A closeup at the earliest times computed shows that the region of negative vorticity appears immediately, for any $t > 0$, and is visible in our results at Δt, independent of the time step. Figure 6.1 shows that as time evolves, the region of negative vorticity grows. It becomes thicker and longer. It is also stretched and entrained by the leading vortex.

Near the tip of the plate, the zero level contour appears to have a small dimple. As was shown in the closeups in figure 4.6, this dimple is well resolved and a true feature of the flow. It consists of positive vorticity that is entrained by the growing region of negative vorticity. As opposed to the region of negative vorticity, this secondarily entrained region of positive vorticity is not attached to the plate and does not grow in time.

Figure 6.2 shows a closeup of the flow near the tip of the plate for various Reynolds numbers, Re = 200, 500, 1000 and 2000, computed using h=0.00078125, 0.00078125, 0.00078125, 0.000390625 and $\Delta t = 5\times10^{-5}, 1\times10^{-5}, 2.5\times10^{-5}, 6.25\times10^{-6}$, respectively. One can see that the region of negative vorticity is stretched and entrained more strongly for larger Re, and that the size of the dimple of entrained positive vorticity decreases with increasing Re.

Details of the vorticity near the plate are shown in figure 6.3, 6.4. Figure 6.3b plots the vorticity along four line segments x=0.4,0.425, 0.45 and 0.475, shown in figure 6.3a, for the solution with Re=500 at t=0.04. It shows that the vorticity has large gradients near the plate, and that the maximal plate vorticity increases as the tip is approached. The maximum absolute vorticity is found near the tip of the plate.

Figure 6.4 shows the size of the region of negative vorticity attached to the plate, as a function of time, for the simulation with Re=500 at t=0.04. Figure 6.4a plots the region of negative vorticity and the streamlines of the flow. The zero streamline contour encloses a recirculating region of fluid. It leaves the tip of the plate and reattaches to the plate downstream. Note that the point of reattachment of the

zero streamline contour coincides approximately with the point of reattachment of the zero vorticity contour. The distance s between the plate tip and the point of reattachment of zero streamline is a measure of the length of the region of negative vorticity. Figure 6.4b plots the migration of s vs. t. The data is obtained at discrete times, shown by $*$. The dashed line is a least square fit of the data using a cubic polynomial. By extrapolation, it is found that s=0.5 at t=0.0945. In other words, the negative vorticity is expected to reach the plate center at t=0.0945.

Figure 6.5 plots the maximum velocity vs. time, computed with the indicated values of h on a logarithmic scale. The data with the three largest values of h is the same as the one shown in figure 4.4 on a linear scale. On the logarithmic scale, one can see that the maximum velocity decays like

$$U_{\max} \sim t^{-1/4}. \tag{6.2}$$

The data for the smallest two values of h is somewhat vertically displaced from the other three data sets. This may have to do with the time steps used, which range from 10^{-6} to 10^{-4}. This needs to be studied further. However, the slope in the logarithmic scale is close to $-1/4$ as well.

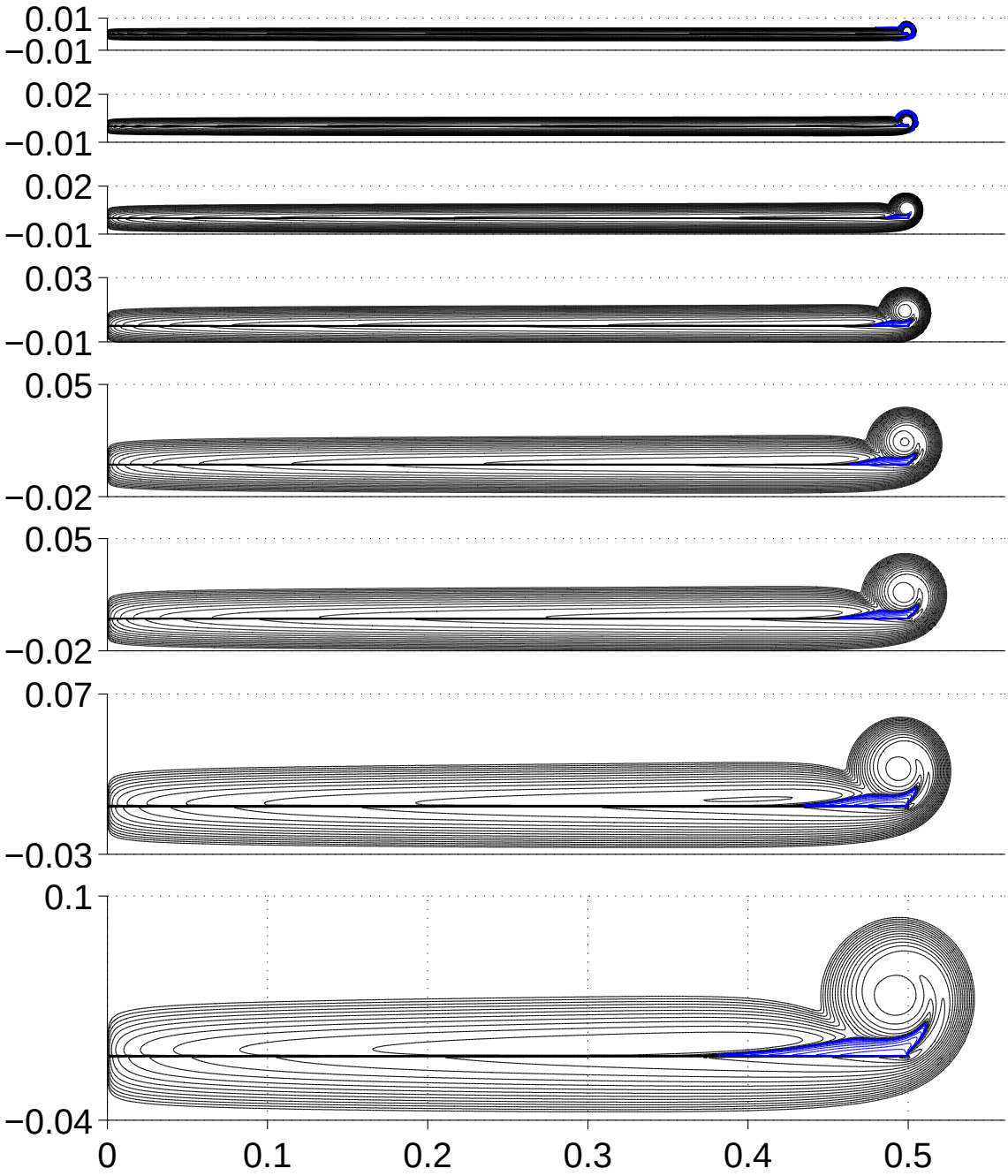

Figure 6.1: Vorticity contours for Re=500 at t = 0.0002, 0.0004, 0.001, 0.002, 0.004, 0.005, 0.01 and 0.02. For results at t = 0.0002, 0.0004 and 0.001, h = 0.000390625, Δt = 2×10^{-6}; for results at t = 0.002, 0.004, 0.005, 0.01 and 0.02, h = 0.00078125, Δt = 1×10^{-5}. $\omega = \pm 2^{[-5:12]}$.

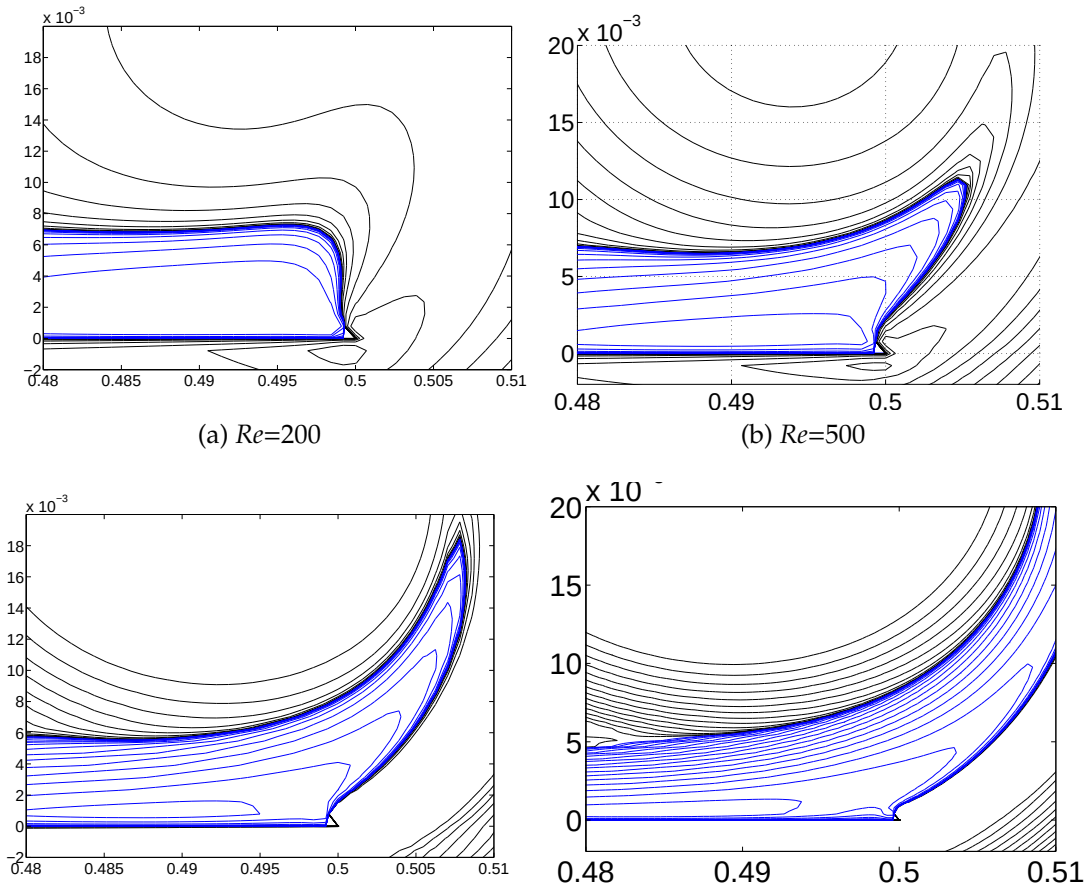

(a) *Re*=200 (b) *Re*=500

(c) *Re*=1000 (d) *Re*=2000

Figure 6.2: Vorticity contours near the plate tip at time t=0.01 for Re=250, 500, 1000 and 2000. The contour levels are $-2^{[-3:8]}$ and $2^{[-3:12]}$ for Re=200, 500, 1000 and $-2^{[-5:8]}$ and $2^{[-5:12]}$ for Re=2000.

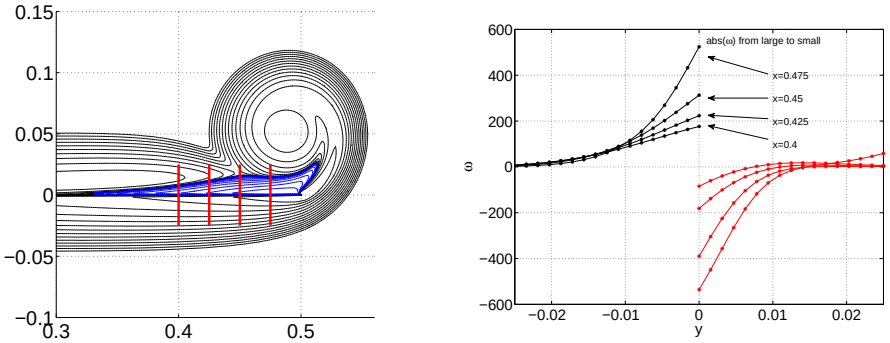

(a) (b)

Figure 6.3: *(a)*Vorticity contours for Re=500 at t=0.04. four line segments are depicted, x=0.4, 0.425, 0.45 and 0.475. *(b)* shows the values of vorticity along these lines segments.

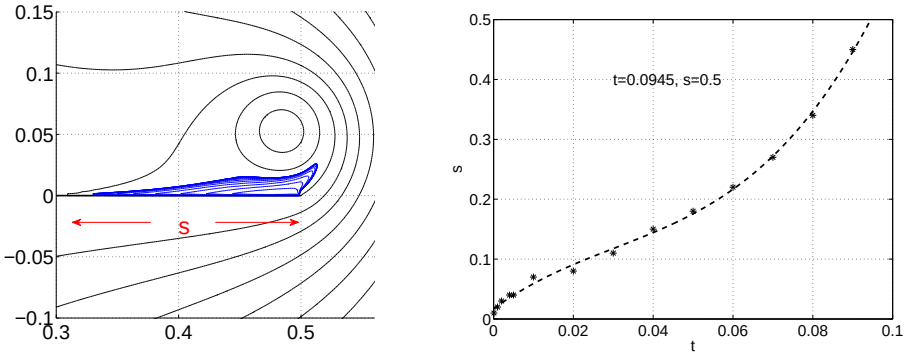

(a) (b)

Figure 6.4: Migration of the negative vorticity region towards the plate center by tracking the intersection of zero level streamline and the plate. *(a)* Negative vorticity contours and instantaneous streamlines for Re=500 at t=0.04. s measures the distance between the plate tip and the intersection of zero level streamline and the plate. *(b)* The evolution of s at discrete times is plotted in asterisks, the dashed line is a least square fit of the data using the cubic interpolation. s is 0.5 at t = 0.0945.

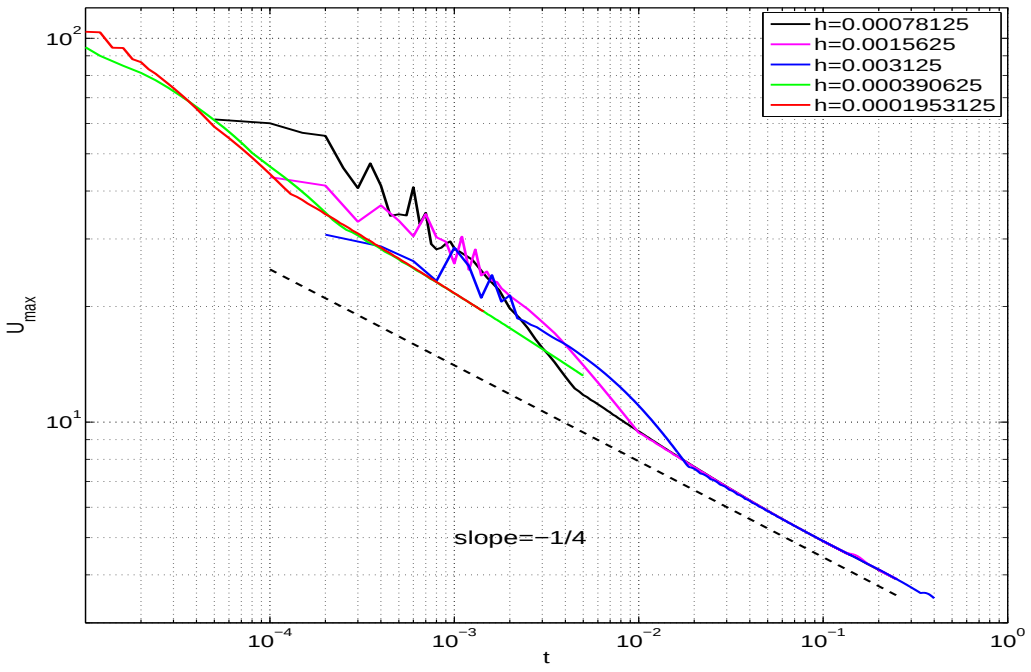

Figure 6.5: The maximum velocity $U_{\max}$ vs. t on a loglog scale, computed with the indicated values of h.

6.1.2 Evolution at a long time

Figure 6.6 and figure 6.7 show vorticity contours and instantaneous streamlines for fixed Re=500 at relatively large times, t =0.1, 0.2, 0.5,1,2, 3 and 5. The starting vortex continues to increase in size with time. This region of negative vorticity has extended all the way to the center of the plate $(0, 0)$. The shape of vorticity contours stays symmetric all the time. The vorticity boundary layer on the other side of the plate is positive, and its thickness looks unchanged. The recirculation region increases in length and the vortex width expands in the x direction.

The negative vorticity region is not uniform along the plate, and the thickness H of the region changes with time as well. Figure 6.8a shows the vorticity contours for Re=500 at t = 0.04. One picks a line at x=0.4, and figure 6.8b shows the evolution of H for Re=500. H increases initially and then decreases. The maximum thickness is 0.156 around t=1.5. The decrease in H is attributed to the expansion of the starting vortex. The size of the starting vortex is growing in all directions with time due to effect of diffusion. The negative vorticity keeps being entrained and stretched by the starting vortex.

Figure 6.9 and figure 6.10 show vorticity contours and instantaneous streamlines at a fixed time t=1 for a sequence of Reynolds numbers, Re =20, 40, 126, 200, 500, 1000, 2000 and 4000. The flow topology does not vary a lot for different Reynolds numbers. A single vortex spiral forms, and grows with time. For large Reynolds number, for example Re=1000, there is a visible separated shear layer that rolls up in spiral, and I will call it vortex band. Or in another word, the vortex band is the region of vorticity that connects the major vortex spiral and the plate tip. Vorticity has large diffusion for low Reynolds numbers. As the Reynolds number becomes larger, the vortex band is tighter and the support of the whole vorticity is smaller. The thickness of the negative vorticity region is smaller for a large Reynolds number as well. These results show good agreement with results in the literature [23][28][44].

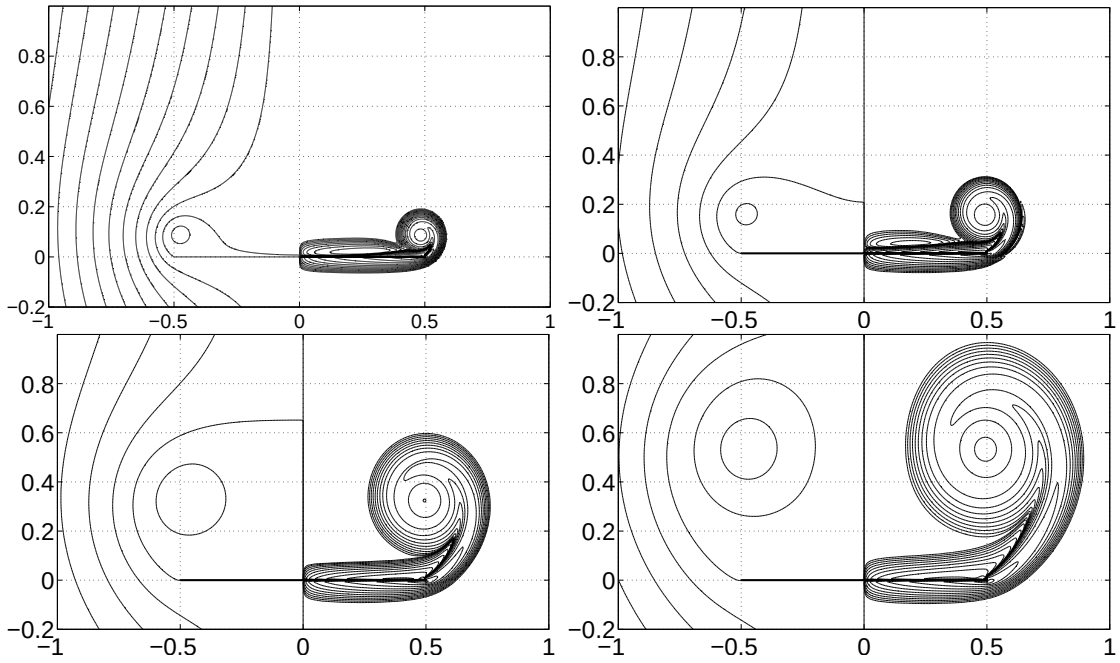

Figure 6.6: Vorticity contours and instantaneous streamlines for Re=500 at t = 0.1, 0.2, 0.5 and 1. The contour levels of vorticity are $\pm 2^{[-5:8]}$ and the contour levels of the stream function ψ are $[-1 : 0.1 : 1]$.

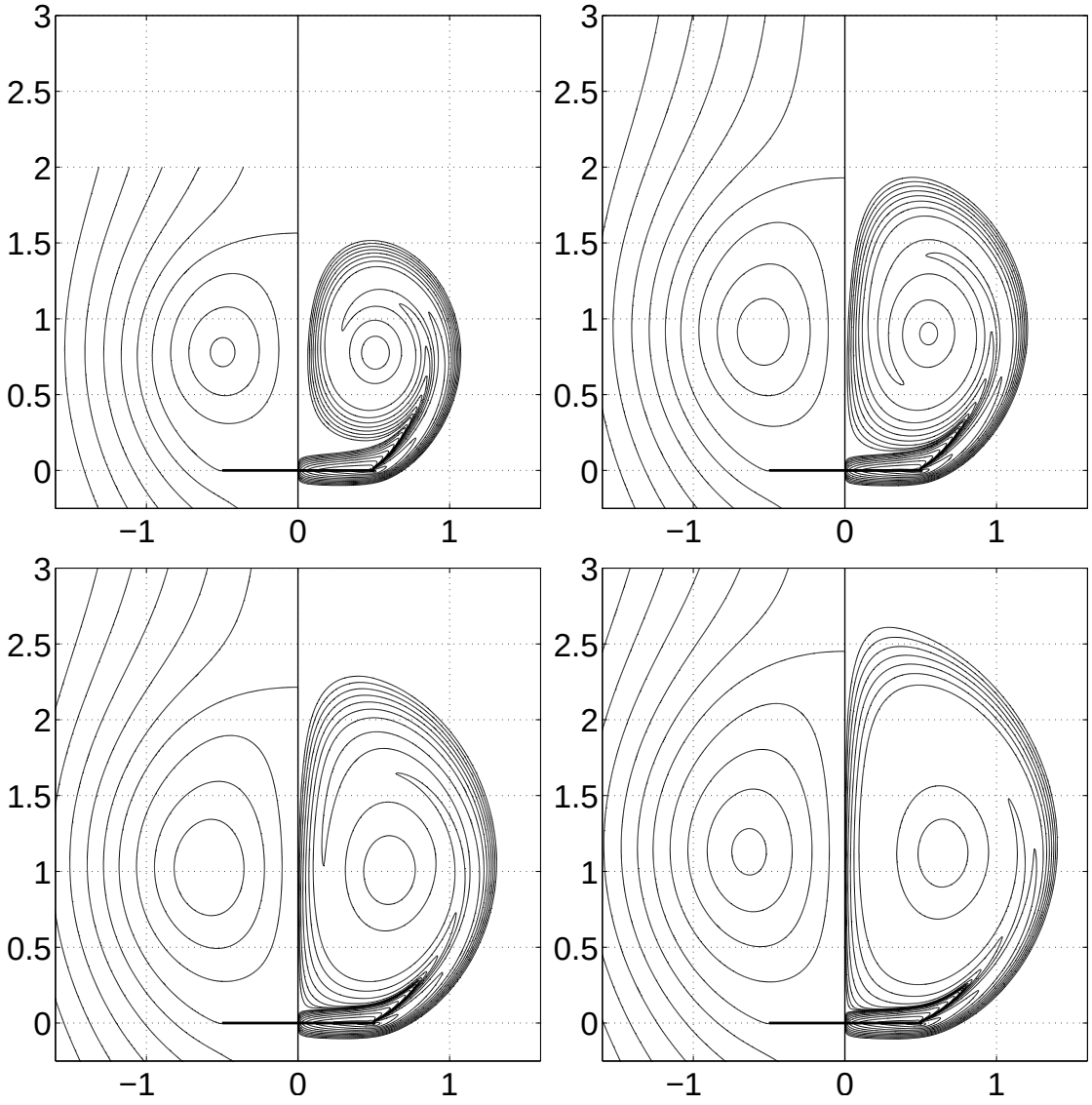

Figure 6.7: Continuation of figure 6.6. Vorticity contours and instantaneous streamlines for Re=500 at t = 2, 3, 4 and 5.

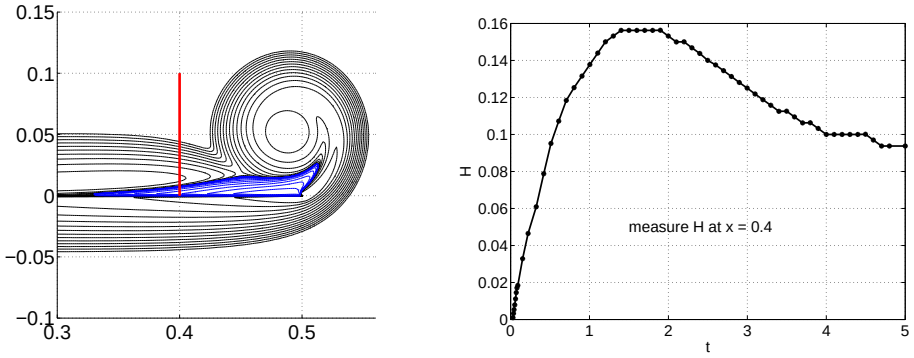

Figure 6.8: The thickness of the negative vorticity region H at $x = 0.4$ vs.t for Re=500.

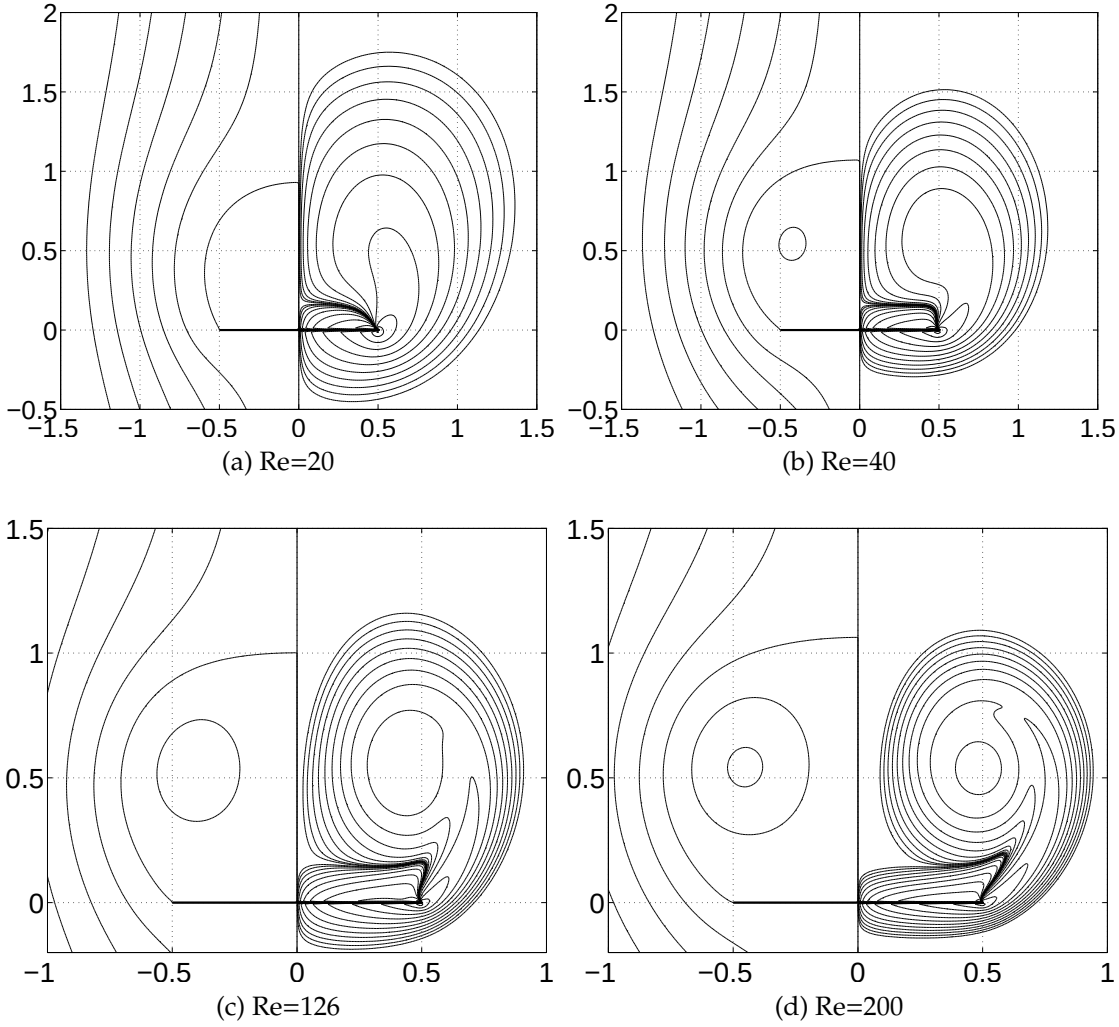

Figure 6.9: Vorticity contours and instantaneous streamlines at t=1 for Re=20, 40, 126 and 200. The contour levels of the vorticity ω are $\pm 2^{[-5:8]}$ and the contour levels of the stream function ψ are $[-1 : 0.1 : 1]$.

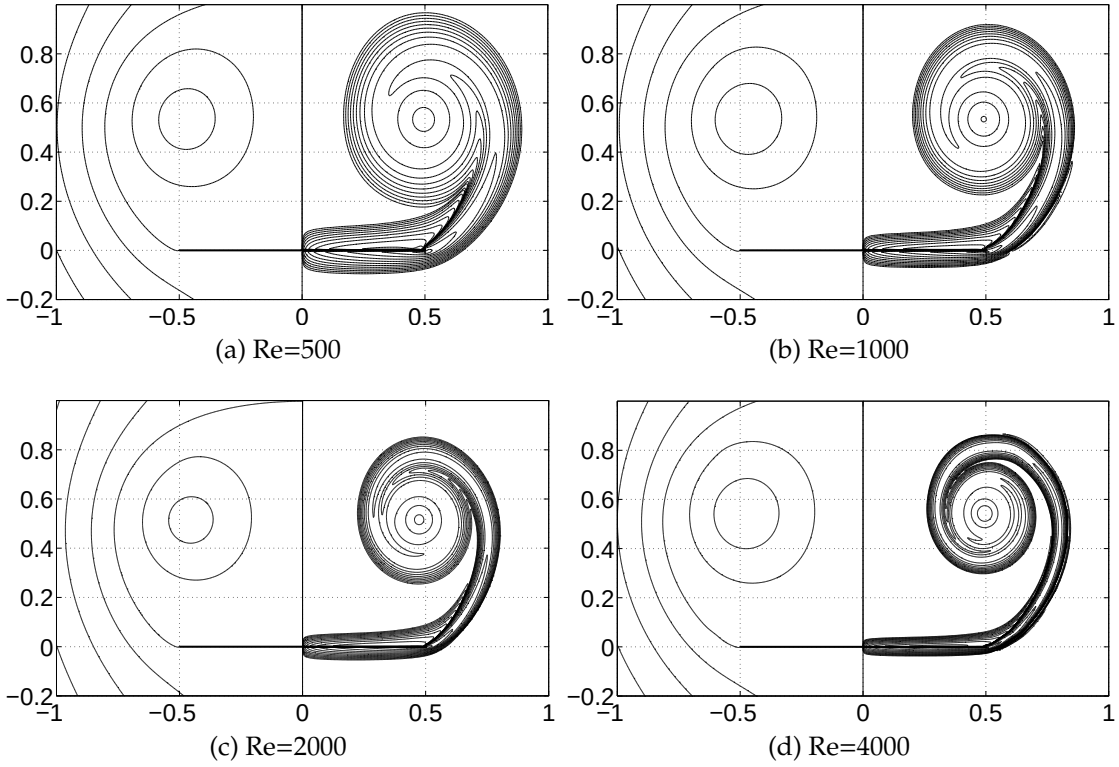

(a) Re=500 (b) Re=1000

(c) Re=2000 (d) Re=4000

Figure 6.10: Continuation of figure 6.9. Vorticity contours and instantaneous streamlines at t=1 for Re=500, 1000, 2000 and 4000. The contour levels of the vorticity ω are $\pm 2^{[-5:8]}$ and the contour levels of the stream function ψ are $[-1 : 0.1 : 1]$.

6.1.3 Instability

The instability of the outer spiral turn that has been observed in experiments and computations, are observed in my computation at Re = 4000 around t=1.5 . The instability does not vanish if the mesh size is halved. The vorticity is smooth initially. The secondary vortices first appear in the middle of the vortex band and the instability tends to migrate toward the main spiral core. In the literature, the instability is categorized as a Kevin-Helmholtz type instability. Remember that Kevin-Helmholtz instability occurs when a vorticity shear layer is perturbed and unstable modes keep growing. In my computations, however, it is still not clear what the mechanism is to trigger the unstable modes in the numerical computation.

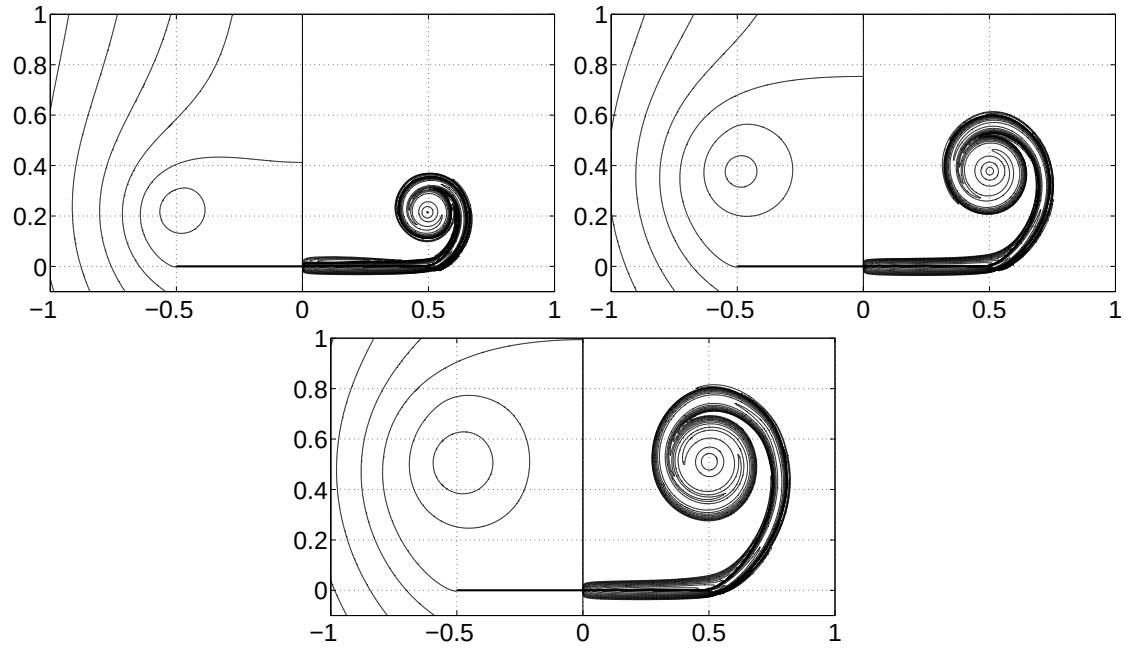

Figure 6.11: Vorticity contours and instantaneous streamlines for Re=4000 at t = 0.3, 0.6 and 0.9. The contour level of the vorticity ω is $\pm 2^{[-5:8]}$ and the contour level of the stream function ψ is $[-1 : 0.1 : 1]$.

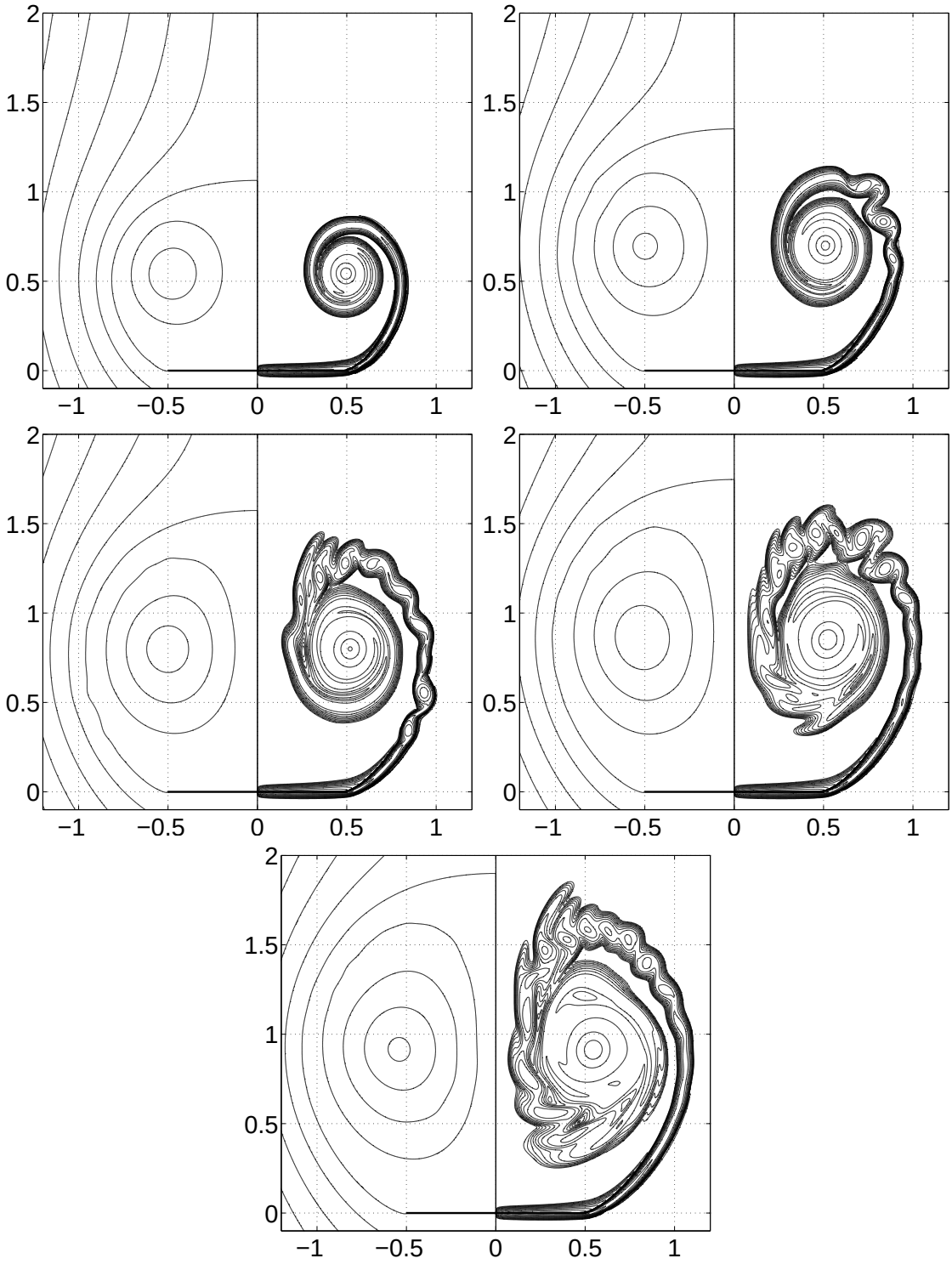

Figure 6.12: Continuation of figure 6.11. Vorticity contours and instantaneous streamlines for Re=4000 at t = 1, 1.5, 2, 2.5 and 3.

6.1.4 Vortex size and width

After a time around 0.1, zero level streamline encloses a region of recirculation downstream of the plate, which is referred to as the vortex size. The plate is always a part of the vortex size boundary since the stream function is zero on the plate. The stream function changes sign from the inner side of the vortex bubble to the outer side. The vortex size s is defined as the y-coordinate of the intersection between zero level streamline and the y-axis, see figure 6.13. The size s is growing with time. A closer study of vortex size is shown later.

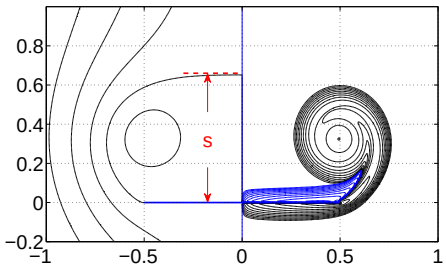

Figure 6.13: Vorticity contours and streamlines for Re=500 at t=0.5. s measures the length of the vortex size which is the y-coordinate of the intersection between the y-axis and the zero level streamline

Taneda and Honji (1970) [44] conducted a series of laboratory experiments to study the development of the separated flow past a finite plate. They found relations that connect the vortex size s, time t and the kinematic viscosity ν. According to [44], the length of the scaled vortex size s/L is nearly proportional to $(Ut/L)^{2/3}$ and $\tau = \nu t/L^2$,

$$s/L \propto (Ut/L)^{2/3} \quad \text{and} \quad s/L \propto \tau, \quad \text{where} \quad \tau = \nu t/L^2 \tag{6.3}$$

at small values of t such that $(\nu t/L^2) \leq 1$. Here U is the plate speed, and L is the plate length. Figure 6.14 shows loglog plots of the scaled vortex size s/L vs.τ and s/Lvs.(Ut/L), respectively, using results of my computations. One can see that the scaled vortex size follows the 2/3 scaling rule generally while the growth rate slows down near the tail of each curve. The scaled vortex size s/L is a function of τ taking the form of

$$s/L = k(\nu)\tau^{2/3} \tag{6.4}$$

where $k(\nu)$ is a function of the kinematic viscosity and the value of $k(\nu)$ is inversely proportional in ν. In figure 6.14b, the curves at different Reynolds numbers seem

to overlap each other. This indicates that the vortex size is not affected by viscosity. Using a radical function of order 2/3 to fit the data of Re=40 (excluding the first three points) in the least square sense, the relation between s/L and Ut/L in figure 6.14b is close to

$$s/L = 0.91(Ut/L)^{2/3}. \tag{6.5}$$

The results of other Reynolds numbers are below the line of equation (6.5) near the tail. The equation (6.5) is very close to the relation of $s/L = 0.89(Ut/L)^{2/3}$ in [44]. Table 6.1 summarizes the results of vortex size measurements at $Re = 40$ and $Re = 126$.

Re=40				Re=126			
τ	Ut/L	s/L	$(s/L)\tau^{-2/3}$	τ	Ut/L	s/L	$(s/L)\tau^{-2/3}$
0.0200	0.40	0.52	7.1	0.0032	0.40	0.49	22.7
0.0300	0.60	0.73	7.6	0.0048	0.60	0.70	24.7
0.0400	0.80	0.91	7.8	0.0063	0.80	0.86	25.1
0.0500	1.00	1.07	7.9	0.0079	1.00	1.00	25.1
0.0600	1.20	1.21	7.9	0.0095	1.20	1.13	25.1
0.0700	1.40	1.33	7.8	0.0111	1.40	1.24	24.9
0.0800	1.60	1.45	7.8	0.0127	1.60	1.35	24.8
0.0900	1.80	1.56	7.8	0.0143	1.80	1.45	24.6
0.1000	2.00	1.67	7.8	0.0159	2.00	1.54	24.4
0.1100	2.20	1.77	7.7	0.0175	2.20	1.63	24.2
0.1200	2.40	1.87	7.7	0.0190	2.40	1.71	24.0
0.1300	2.60	1.97	7.7	0.0206	2.60	1.80	23.9
0.1400	2.80	2.07	7.7	0.0222	2.80	1.87	23.7
0.1500	3.00	2.16	7.7	0.0238	3.00	1.95	23.6
0.1600	3.20	2.26	7.7	0.0254	3.20	2.02	23.4
0.1700	3.40	2.33	7.6	0.0270	3.40	2.10	23.3
0.1800	3.60	2.42	7.6	0.0286	3.60	2.16	23.1
0.1900	3.80	2.50	7.6	0.0302	3.80	2.23	23.0
0.2000	4.00	2.57	7.5	0.0317	4.00	2.30	22.9
0.2100	4.20	2.65	7.5	0.0333	4.20	2.36	22.8
0.2200	4.40	2.73	7.5	0.0349	4.40	2.41	22.6
0.2300	4.60	2.81	7.5	0.0365	4.60	2.48	22.5

Table 6.1: A summary of vortex size information for Re=40 and Re=126.

The vortex width is defined to be the large extent of ω=1 contour in the x direction, see figure 6.15. The width will be larger or smaller than L if the contour level of ω is greater or smaller than 1. Figure 6.16 shows the band width ($\omega = 1$)vs.t at Re=200, 500, 1000 and 2000 . The width grows with time. All curves seem to overlap each other, and this indicates that the width is independent of the Reynolds number.

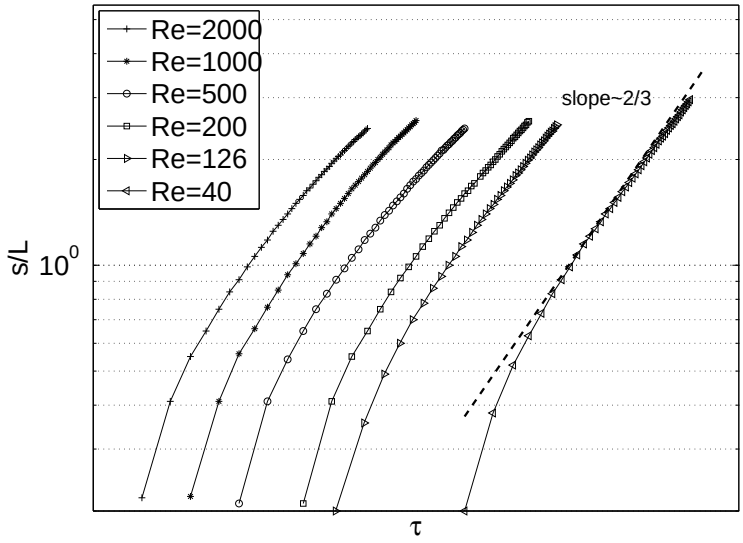

(a)

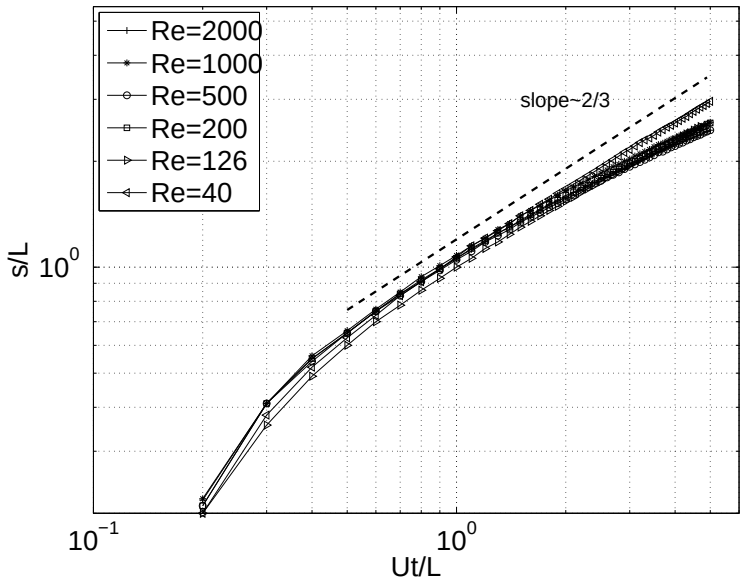

(b)

Figure 6.14: The loglog plots of (a) the scaled vortex size s/L vs.τ and (b) the scaled vortex size s/L vs.Ut/L. The length of the plate is $L = 1$ and $\tau = \frac{vt}{L^2}$.

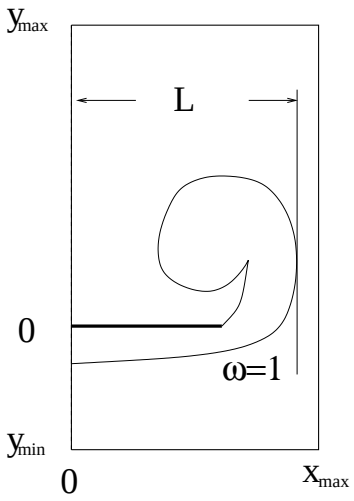

Figure 6.15: A schematic of the vortex width L of the contour level $\omega = 1$.

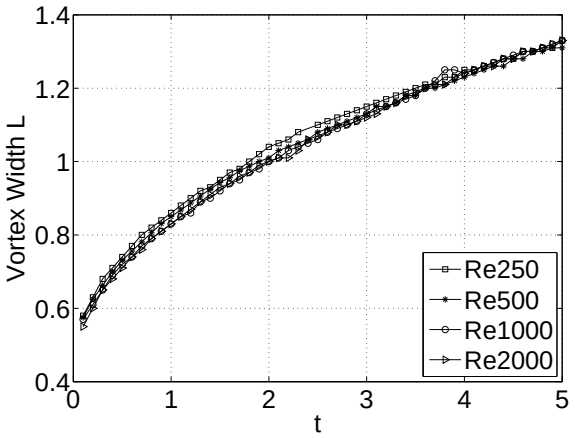

Figure 6.16: The vortex width L ($\omega = 1$)vs.t for four Reynolds numbers Re = 250, 500, 1000 and 2000.

6.1.5 Vortex core

Table 6.2 gives the trajectory of the vortex core at Re=200, 500, 1000 and 2000. The coordinate of the core is (x_c, y_c), and the vorticity value at the core is ω_c. One can see that the core moves vertically since x_c rarely changes with time, and the value x_c is almost the same for all Reynolds numbers. In the vertical direction, the core moves faster at a large Reynolds number. At a fixed time, the core value ω_c increases as the Reynolds number increases. This implies that more vorticity is carried by the core at larger Reynolds numbers.

Re=200

t	x_c	y_c	ω
0.5	0.48	0.33	42.77
1	0.48	0.54	22.06
1.5	0.48	0.68	16.59
2	0.49	0.78	13.60
2.5	0.49	0.85	11.55
3	0.49	0.91	10.06
3.5	0.49	0.96	8.85
4	0.49	1.02	7.79
4.5	0.49	1.09	6.95
5	0.49	1.16	6.33

Re=500

t	x_c	y_c	ω
0.5	0.48	0.32	64.52
1	0.48	0.53	38.63
1.5	0.48	0.67	28.76
2	0.49	0.77	23.23
2.5	0.49	0.84	19.28
3	0.49	0.90	16.05
3.5	0.49	0.95	13.39
4	0.49	1.00	11.27
4.5	0.49	1.06	8.11
5	0.49	1.11	8.48

Re=1000

t	x_c	y_c	ω
0.5	0.49	0.32	111.06
1	0.49	0.53	65.49
1.5	0.49	0.67	47.55
2	0.49	0.78	36.19
2.5	0.49	0.85	28.86
3	0.49	0.91	16.49
3.5	0.49	0.95	13.39
4	0.49	0.99	12.04
4.5	0.49	1.06	9.98
5	0.49	1.11	8.66

Re=2000

t	x_c	y_c	ω
0.5	0.48	0.30	123.70
1	0.48	0.51	73.24
1.5	0.48	0.65	54.52
2.1	0.48	0.76	43.21
2.5	0.49	0.81	38.49
3	0.49	0.85	33.68
3.5	0.49	0.90	28.41
4	0.49	0.94	23.05
4.5	0.49	0.97	17.86
5	0.49	1.03	14.23

Table 6.2: The trajectory (x_c, y_c) and values ω_c of the vortex core for Re = 200, 500, 1000 and 2000.

6.1.6 Circulation

The circulation shed from the plate is calculated as an integration over an area Ω

$$\Gamma(t) = \int \int_{\Omega} \omega(\mathbf{z}, t) d\mathbf{z}. \tag{6.6}$$

Vorticity is generated everywhere from the plate, but we want to count vorticity shed from the tip only. The shaded area of figure 6.17 illustrates how the area Ω is chosen. The computational domain is $[0, x_{\max}] \times [y_{\min}, y_{\max}]$, and the plate tip is at $(\frac{L}{2}, 0)$. x_ϵ is on left of the tip, and x_ϵ, y_s is on the zero level vorticity. A small triangle area between zero level vorticity and the plate is included to count a small region of entrainment near the tip. The curve between x_ϵ, y_s and x_ϵ, y_e is part of the vorticity contour of level $\omega = 0.1$

Figure 6.18 shows shed circulation Γ vs.t for Re=200, 500, 1000 and 2000. Figure 6.18a uses a linear scale. Initially, Γ does not depend on Reynolds numbers, at a large time period, more circulation is shed from the tip for a larger Reynolds number. From the logarithmic scale, shown in figure 6.18b, one can see that the circulation scales as $t^{1/3}$ initially, and $t^{1/2}$ later. The initial scaling follows the scaling for the semi-infinite plate, section 7. At early times, these two flows are expected to scale similarly.

Figure 6.19 shows the shedding rate $d\Gamma/dt$vs.t. The circulation shedding rate $d\Gamma/dt$ is computed using a second order central difference method in time. The shedding rate is large initially and then slows down with time. The rate is big for a large Reynolds number, and has no apparent dependence on Reynolds numbers.

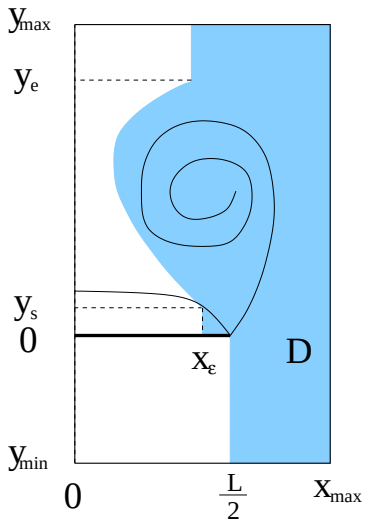

Figure 6.17: A Schematic of the integral region Ω (shadow) to compute the circulation shed from the plate tip.

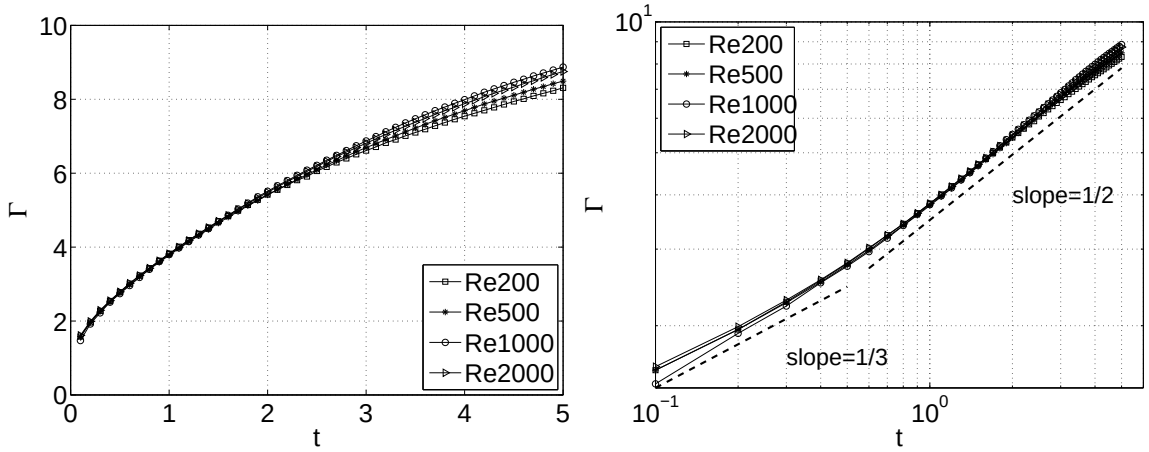

Figure 6.18: The circulation shed from the tip Γ vs.t for four different Reynolds numbers Re = 200, 500, 1000 and 2000 on *(a)* a linear scale, *(b)* a logarithmic scale.

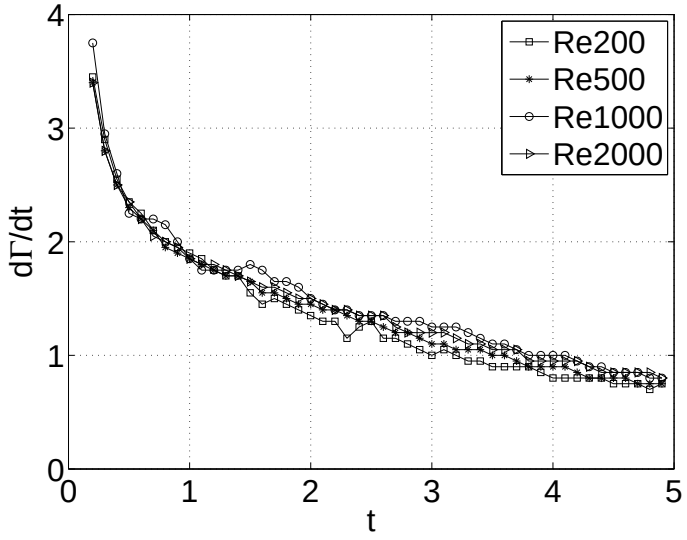

Figure 6.19: The circulation shedding rate $d\Gamma/dt$ vs. t for four different Reynolds numbers Re = 200, 500, 1000 and 2000.

6.2 Uniform acceleration

The problem of accelerated background flow past a finite is not extensively studied in numerical computations, though it seems to be a natural problem in the experimental aspect. The few results available, by KS, are much under-resolved and inconsistent within the paper. Careful documentation of the dynamics of this fundamental flow still needs to be done. This section presents the results for flow past a finite plate with a uniformly accelerated flow

$$U_\infty(t) = at \tag{6.7}$$

where a is the acceleration. The characteristic length L is the length of the plate. However, it is not clear what characteristic velocity is. Therefore, results of sections 6.2.1, 6.2.2, 6.2.3 and 6.2.4 are presented in terms of viscosity, acceleration and time. All the computations in this section are at ν=0.025. Six different values of acceleration are chosen, a=10, 25, 50, 75, 100 and 125. Section 6.2.1 presents the evolution of the vorticity contours. Section 6.2.2 concerns the dependence on a of vorticity contours. Section 6.2.3 presents the trajectory and vorticity of the vortex core. Section 6.2.4 concerns about the recirculation region. Section 6.2.5 presents the dimensional analysis using a characteristic time $T = \sqrt{L/a}$, and introduces a dimensionless parameter Re_a. Section 6.2.6 shows dependence of vorticity contours on Re_a. Section 6.2.7 dependence of circulation on Re_a.

6.2.1 Evolution

Figure 6.20 and figure 6.21 show the evolution of the vorticity for ν=0.025 at a = 100. h=0.00625 in the computation, Δt starts with 5×10^{-4} and decreases to 1×10^{-5} after t=0.2. The flow structures are similar to that of the uniform background flow. The starting vortex forms and rolls up. The region of negative vorticity is present and extends towards the center of the plate.

These results were also presented by KS [23] using the vortex particle method, (figure 25, figure 26 in their paper). The geometry, viscosity and the time of these snapshots are the same in both theirs and my computations. The mesh size in KS is unknown. However, our results are not quite in agreement. In their plots, the region of negative vorticity is absent at t=0.02 and there is inconsistency in the vortex size transition from t= 0.08 to 0.1 . The vorticity contours look noisy from the very beginning, and they observed instability at t = 0.3 and 0.4 while my results look stable.

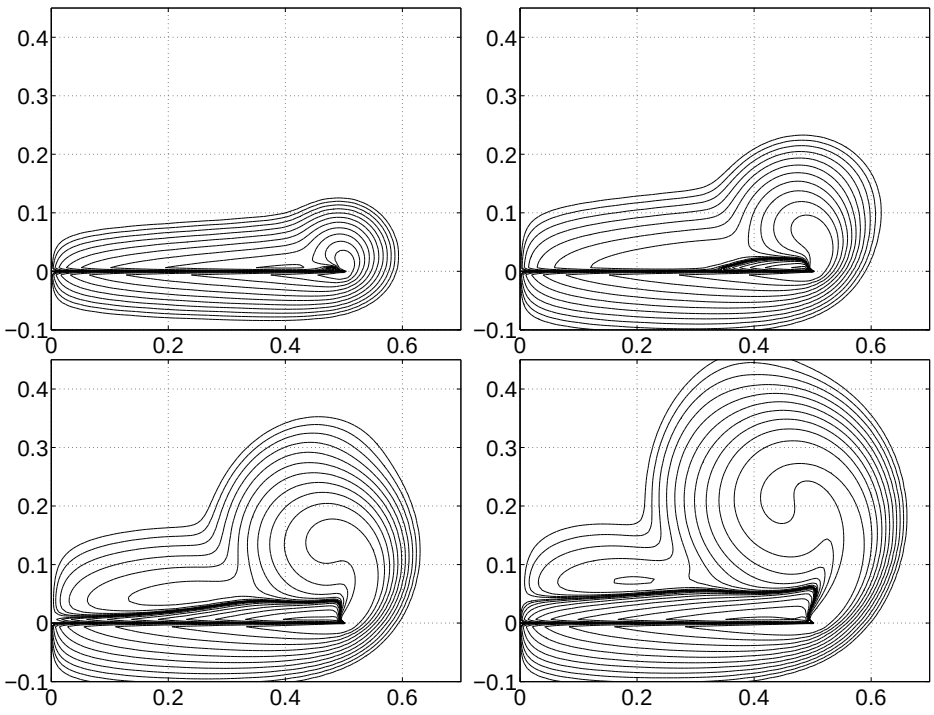

Figure 6.20: Vorticity contours for a=100 at t = 0.02, 0.04, 0.06 and 0.08, ν=0.025. The contours levels are $\pm 2^{[-2:8]}$.

6.2.2 Dependence on the acceleration

Figure 6.22 compares the vorticity contours for a sequence of accelerations, a = 10, 25, 50, 75, 100 and 125, at t = 0.3. The time step should be bigger for a small acceleration a due to a small maximum velocity, but I used the same Δt as that for a=100. For a large acceleration, the support of the vorticity is bigger, the region of negative vorticity is more entrained by the positive vorticity region. There are dimples above the tip of the plate for all a.

6.2.3 Vortex core

Results at five accelerations are compared in the trajectory and values of the vortex core, a = 10, 25, 50, 75 and 100. Table 6.3 gives the coordinates of the vortex core (x_c, y_c) and ω_c for a sequence of times, t = 0.1, 0.15, 0.2, 0.25, 0.3, 0.35 and 0.4. One can see that, at a fixed acceleration a, the core moves vertically since x_c rarely changes with time. The values of x_c are almost the same for all accelerations. In

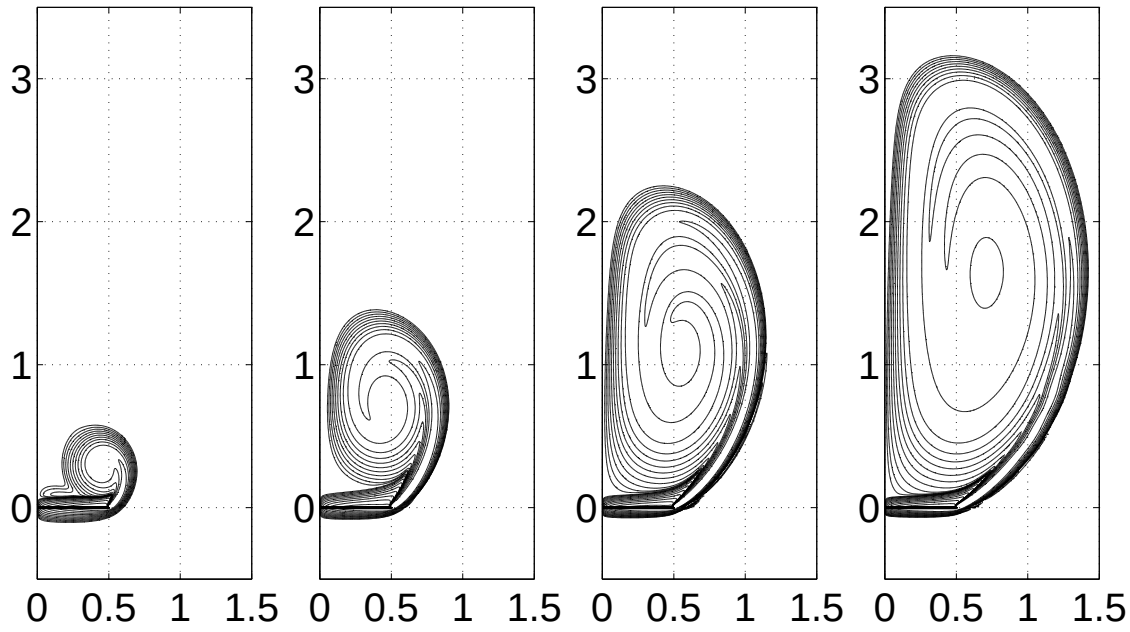

Figure 6.21: Continuation of figure 6.20. Vorticity contours for a=100 at t = 0.1, 0.2, 0.3 and 0.4, ν=0.025. The contour levels are $\pm 2^{[-2:8]}$.

the vertical direction, the core moves faster for a large acceleration.

The flow with ν=0.025 has large diffusion. If the velocity of the background flow is constant, the vorticity at the vortex core would decrease with time, which has been shown in section 6. My plausible explanation is that, the background flow keeps feeding energy into the flow, and this energy input rate is constant with time if the background velocity is constant. The effect of diffusion conquers the effect of energy feeding in the uniform background flow case, therefore, ω_c decreases with time. There is an increasing amount of energy feeding into the flow if the background velocity is accelerated. For a small value of the acceleration a, the effect of diffusion dominates. Therefore, ω_c still decreases with time, for example, a=10 in table 6.3. If the acceleration a is large enough, one can see an increasing value of the vortex core with the time, for example, a=25, 50, 75 and 100 in table 6.3.

a=10, $U_\infty = at$

t	x_c	y_c	ω
0.10	0.49	0.012	85.50
0.15	0.49	0.031	69.66
0.20	0.49	0.106	61.98
0.25	0.49	0.181	59.71
0.30	0.49	0.268	58.10
0.35	0.49	0.368	55.69
0.40	0.49	0.487	52.17

a=25, $U_\infty = at$

t	x_c	y_c	ω
0.10	0.49	0.075	131.81
0.15	0.49	0.193	121.84
0.20	0.46	0.337	104.37
0.25	0.40	0.412	91.25
0.30	0.49	0.481	83.04
0.35	0.49	0.937	81.95
0.40	0.49	1.137	83.68

a=50, $U_\infty = at$

t	x_c	y_c	ω
0.10	0.49	0.181	196.03
0.15	0.49	0.312	154.03
0.20	0.49	0.437	133.78
0.25	0.49	0.918	125.88
0.30	0.49	1.187	131.56
0.35	0.49	1.456	138.96
0.40	0.49	1.725	145.39

a=75, $U_\infty = at$

t	x_c	y_c	ω
0.10	0.43	0.237	223.31
0.15	0.45	0.393	180.60
0.20	0.49	0.931	171.56
0.25	0.49	1.275	184.27
0.30	0.49	1.631	197.08
0.35	0.49	1.993	204.92
0.40	0.49	2.368	206.37

a=100, $U_\infty = at$

t	x_c	y_c	ω
0.10	0.49	0.262	247.43
0.15	0.49	0.645	209.10
0.20	0.49	1.156	222.45
0.25	0.49	1.555	240.40
0.30	0.49	2.000	250.51
0.35	0.49	2.435	253.50
0.40	0.49	2.893	249.50

Table 6.3: The trajectory (x_c, y_c) and values ω_c of the vortex core for a = 10, 25, 50, 75 and 100, ν=0.025.

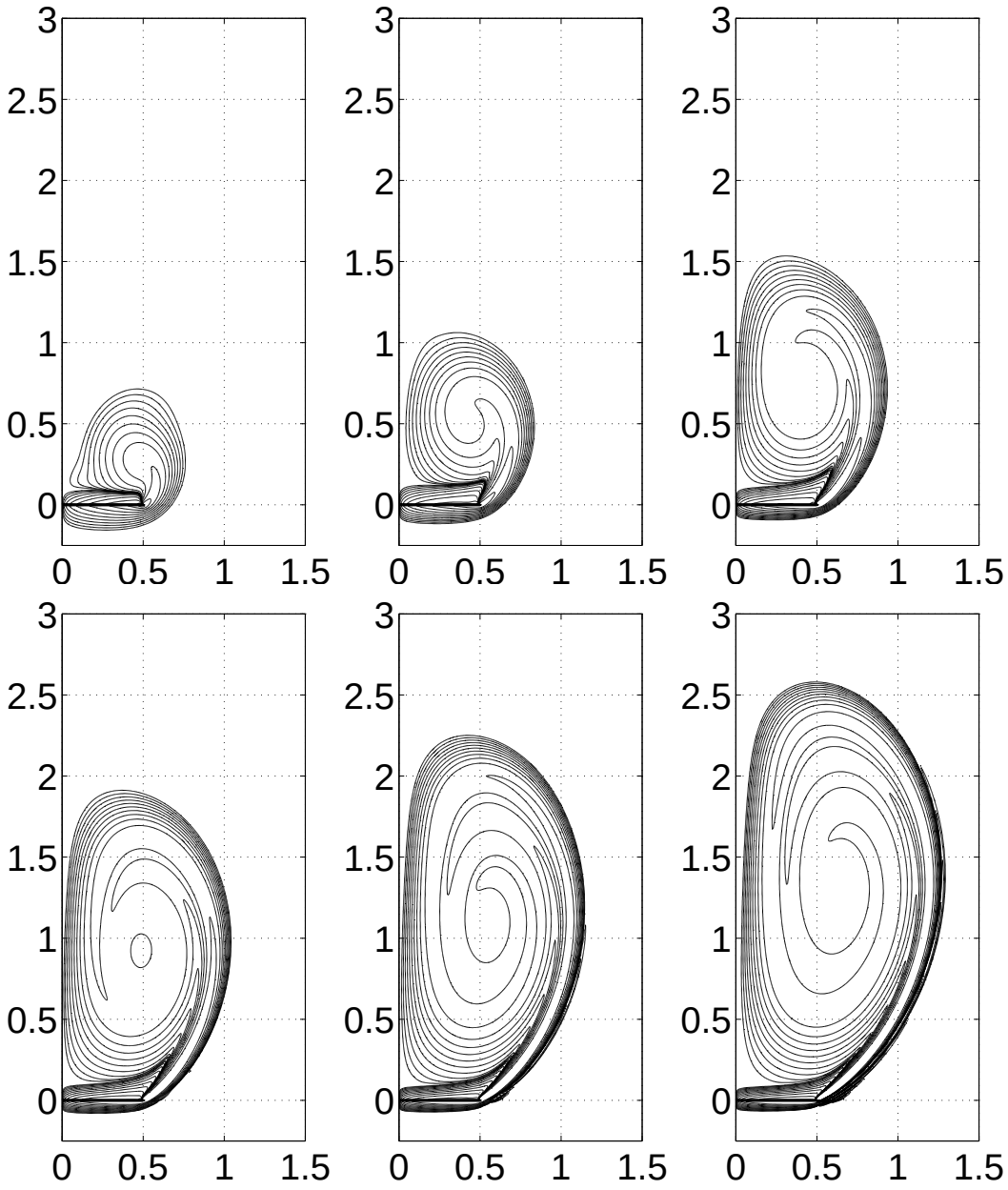

Figure 6.22: Vorticity contours at t=0.3 for a=10, 25 ,50, 75, 100 and 125, ν=0.025. The contour levels are $\pm 2^{[-2:8]}$.

6.2.4 Vortex size

The vortex size is defined in the same way as in section 6.1. In the same work of Taneda and Honji (1970) [44], they proposed that the scaled vortex size $\frac{s}{L}$, in the uniformly accelerated flow case, is proportional to the acceleration a in the form of

$$\frac{s}{L} \sim (\frac{at^2}{L})^{2/3} \tag{6.8}$$

when $\tau < 0.1$, where $\tau = \frac{\nu t}{L^2}$. The plate length is $L = 1$. Both $\frac{s}{L}$ and $\frac{at^2}{L}$ are dimensionless.

Figure 6.23 shows $\frac{s}{L}$ vs. $\frac{at^2}{L}$ for $a = 10, 25, 50, 75$ and 100. For all these data, τ is less that 0.1. These curves in figure 6.23 increase rapidly initially, and later approach a straight line of slope 2/3. Using a least square fit of these data with a radical function of order 2/3 (dashed line in figure 6.23) to yield

$$\frac{s}{L} = 0.519(\frac{at^2}{L})^{2/3} \tag{6.9}$$

in the region where $\frac{at^2}{L} \geq 1$. Taneda and Honji has $\frac{s}{L} = 0.48(\frac{at^2}{L})^{2/3}$. The two coefficients are close.

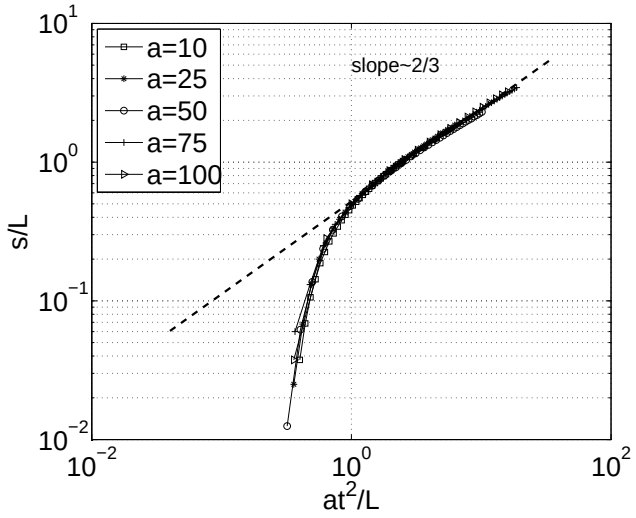

Figure 6.23: The scaled vortex size $\frac{s}{L}$ vs. $\frac{at^2}{L}$.

6.2.5 Dimensionless variables

The governing equation NSE (3.1) for the accelerated flow can be non-dimensional using the characteristic length L as the length of the plate, the characteristic time T as

$$T = \sqrt{\frac{L}{a}}. \tag{6.10}$$

the dimensionless variables are

$$x^* = \frac{x}{L}, \quad y^* = \frac{y}{L}, \quad t^* = \sqrt{\frac{a}{L}}t, \tag{6.11}$$

$$u^* = \frac{u}{\sqrt{aL}}, \quad \omega^* = \omega\sqrt{L/a}, \quad \psi^* = \frac{\psi}{L^{3/2}a^{1/2}} \tag{6.12}$$

and the dimensionless form of NSE

$$\frac{\partial\omega^*}{\partial t^*} + u^* \cdot \nabla^*\omega^* = \frac{\nu}{L^{3/2}a^{1/2}}\Delta^*\omega^* \tag{6.13}$$

$$\Delta^*\psi^* = \omega^*. \tag{6.14}$$

The far field background flow

$$U^*_\infty = t^*. \tag{6.15}$$

The dimensionless parameter of the flow is

$$Re_a = \frac{L^{3/2}a^{1/2}}{\nu}. \tag{6.16}$$

For reference of the following sections,

$$\Gamma^* = \frac{\Gamma}{L^{3/2}a^{1/2}}. \tag{6.17}$$

According to the dimensional analysis, the results shown in figure 6.20 6.21 correspond to Re_a = 400a at a sequence of times t^* = 0.2, 0.4, 0.6, 0.8, 1.0, 2.0, 3.0 and 4.0.

6.2.6 Dependence on Re_a

Next, we present the dependence on Re_a at a fixed time t^* for a sequence values of Re_a. Figure 6.24 shows contours of ω^* at t^*=1.2 for a sequence of Re_a = 126.49,

200.00, 282.84, 346.41, 400.00 and 447.21. The size of the vortex is smaller for a large Re_a. The region of negative vorticity is more entrained by the leading vortex for a large Re_a, it is reminiscence of dependence on Re for the impulsively started case. Also, the thickness of the negative vorticity region decreases as Re_a increases.

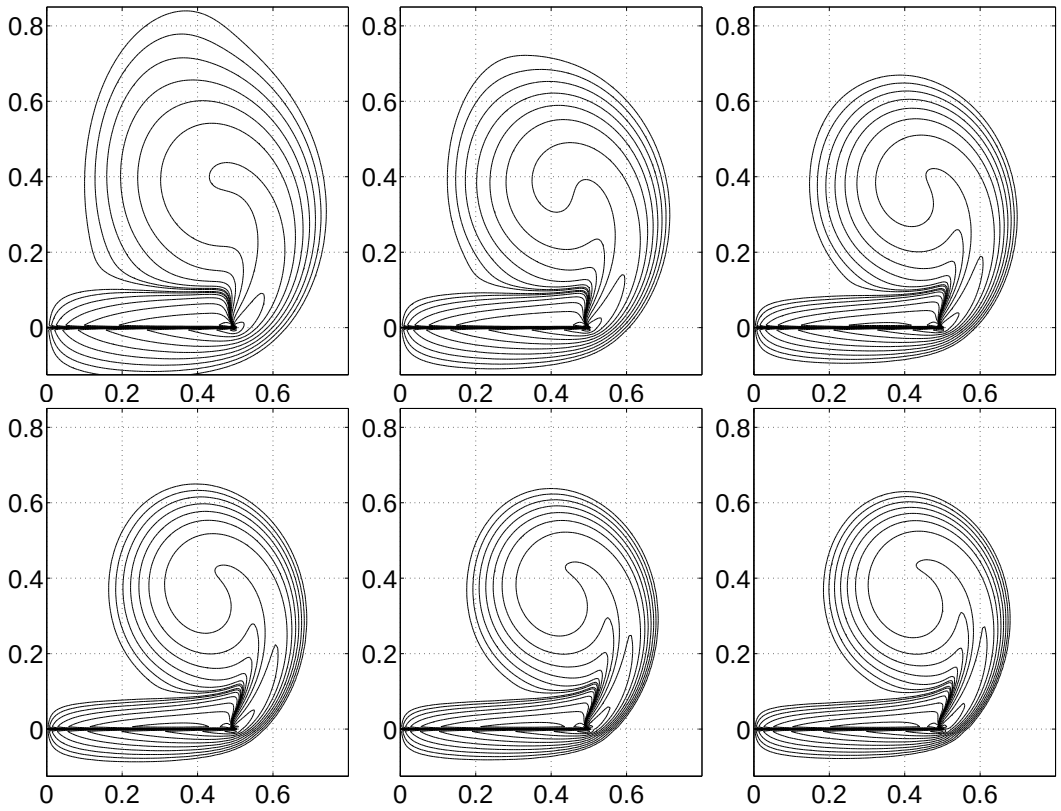

Figure 6.24: Vorticity contours at $t^* = 1.2$ for $Re_a = 126.49$, 200.00, 282.84, 346.41, 400.00, 447.21. The contour levels are $\omega^* = \pm 2^{[-2:8]}$.

6.2.7 Circulation

The circulation shed from the plate tip is calculated in a way similar to that in section 6.1, figure 6.17. Figure 6.25 shows the circulation Γ^* vs.t^* for Re_a = 126.49, 200.00, 282.84, 346.41, 400.00. It is stressed that there is no apparent dependence on Re_a. The circulation Γ increases with time in a way faster than linear behavior. The circulation shedding rate $d\Gamma^*/dt^*$ is computed using the central finite difference method. Figure 6.25 shows the $d\Gamma^*/dt^*$vs.t^*. The rate $d\Gamma^*/dt^*$ increases with time as well, and no apparent dependence on Re_a is observed. Note that $d\Gamma^*/dt^*$ is not zero when $t*$ approaches to zero. The figure looks noisy around t^*=0.4, this is due the integration region D that I used, figure 6.17. The region D does not give a good approximation of the circulation Γ^* during an early time stage.

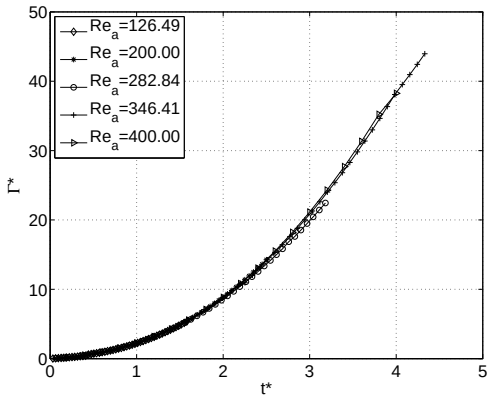

Figure 6.25: Circulation shed from the tip Γ^* vs. t^* for Re_a = 126.49, 200.00, 282.84, 346.41, 400.00.

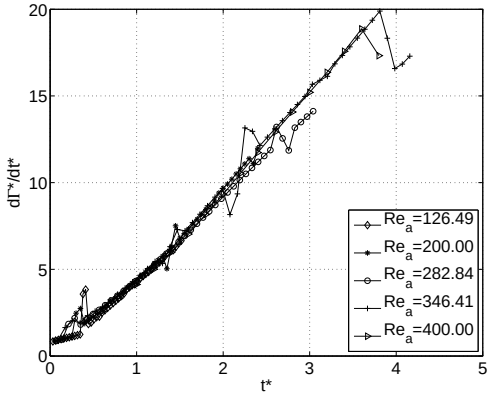

Figure 6.26: Circulation shedding rate $d\Gamma^*/dt^*$ vs. t^* for Re_a =126.49, 200.00, 282.84, 346.41, 400.00.

6.3 Oscillatory

Vortex generation due to periodic motion happens in many real-life situations. Biological rythms are periodic, swimming motions are periodic, forces of sloshing waves hitting a pillar are periodic. For these reasons the periodic case is of interest in itself. The oscillatory flow past a plate is also a classic test case for vortex sheet separation algorithms. Several algorithms are used in practice, and yield slightly different results. Having results from a fully resolved direct numerical simulation available helps to evaluate these algorithms and potentially mimic the viscous separation process better. This is further motivation for studying this case. For reference, we present vortex sheet simulations of the oscillating flow in next to the viscous simulations. Detailed comparisons and analysis remain to be performed. This is work in progress.

This section presents results of flow past a finite plate with an oscillatory flow. The background flow is

$$U_\infty(t) = \sin(\frac{\pi t}{\mathrm{KC}}), \quad \mathrm{KC} = 3.8. \tag{6.18}$$

The characteristic length L is the length of the plate, and the characteristic velocity U is the maximum of the background flow. The following section 6.3.1 presents the evolution of the vorticity contours. Section 6.3.2 concerns the instability. Section 6.3.3 to section 6.3.5 provide results for some global quantities such as the vortex core, circulation and vortex width. Section 6.3.6 shows approximation of the shear layer strength.

6.3.1 Evolution

Figure 6.27 shows the vorticity contours and instantaneous streamlines of Re=2000, at a sequence of times t=0.5, 1, 2, 3, 3.5 and 3.8. The starting vortex grows initially, in a similar way as that of the impulsively started flow case, but it has a new feature related to the secondary vortex of negative sign at the plate tip. This behavior is related to the changing velocity of the background flow. For simplicity, I switch the reference frame in the flow: the flow is stationary and the plate is moving in an oscillatory manner. When the plate accelerates, the starting vortex gains velocity and moves in the same direction with the plate. As the plate slows down, the distance between the starting vortex and the plate is decreasing, the large velocity of the leading vortex induces a secondary vortex to form at the tip. The zero level streamline looks quite different from that of the impulsively started flow case. At

t=3.8, a small vortex bubble is attached to the plate tip. This is also related to the formation of the secondary vortex. Note that there is a hump on the top of the outer turn at t=2. This hump actually occurs at t=1.9, when the acceleration changes sign. The hump migrates downwards along the outer turn and becomes invisible in the end.

Figure 6.28 shows vortex sheet and instantaneous streamlines at the same times as figure 6.27, using the vortex sheet method for δ=0.05. Results of the vortex sheet method are provided to compare to those of the viscous simulations using FDMHS. In figure 6.28, the evolution of the vortex sheet is similar to the shear layer evolution in figure 6.27. The vortex sheet grows downstream at the beginning and then tends to wrap the plate tip in the end. The vortex size is similar to that of FDMHS at t=0.5, but is smaller at other times. The vortex cores location is below y=1 at t=3, 3.5 in figure 6.28 while it is above y=1 in figure 6.27. At t=3.8, the vortex core is around $(1.2, 0.9)$ in both figures 6.28 and 6.27. The vortex sheet method reproduces the general shape of the starting vortex fairly well, though the viscous simulations give more details such as the secondary vortex, and the behavior of the negative vorticity region.

Figure 6.29 compares results of FDMHS at various Reynolds numbers and the vortex sheet method using various values of δ. Figure 6.29(the left column) shows the vorticity contours and instantaneous streamlines at t=3.8 for Re=500, 1000 and 2000. For a large Reynolds number, the boundary layer is more tight and the separated shear layer is more compact. The region of negative and positive vorticity is more clearly separated for larger Reynolds number as well. The vortex core location at these three Reynolds numbers is approximately at the same place, around $(1.2, 0.9)$. Figure 6.29(the right column) shows locations of the vortex sheet and instantaneous streamlines at t = 3.8 for δ = 0.2, 0.1 and 0.05. Here δ can be viewed as the artificial smoothing parameter introduced in the vortex sheet method. As δ decreases, the vortex sheet reveals more details. The secondary vortex sheet roll-up near the tip becomes tight as δ decreases. The vortex core location with these three values of δ remains approximately the same, and it seems lower than that of the viscous results.

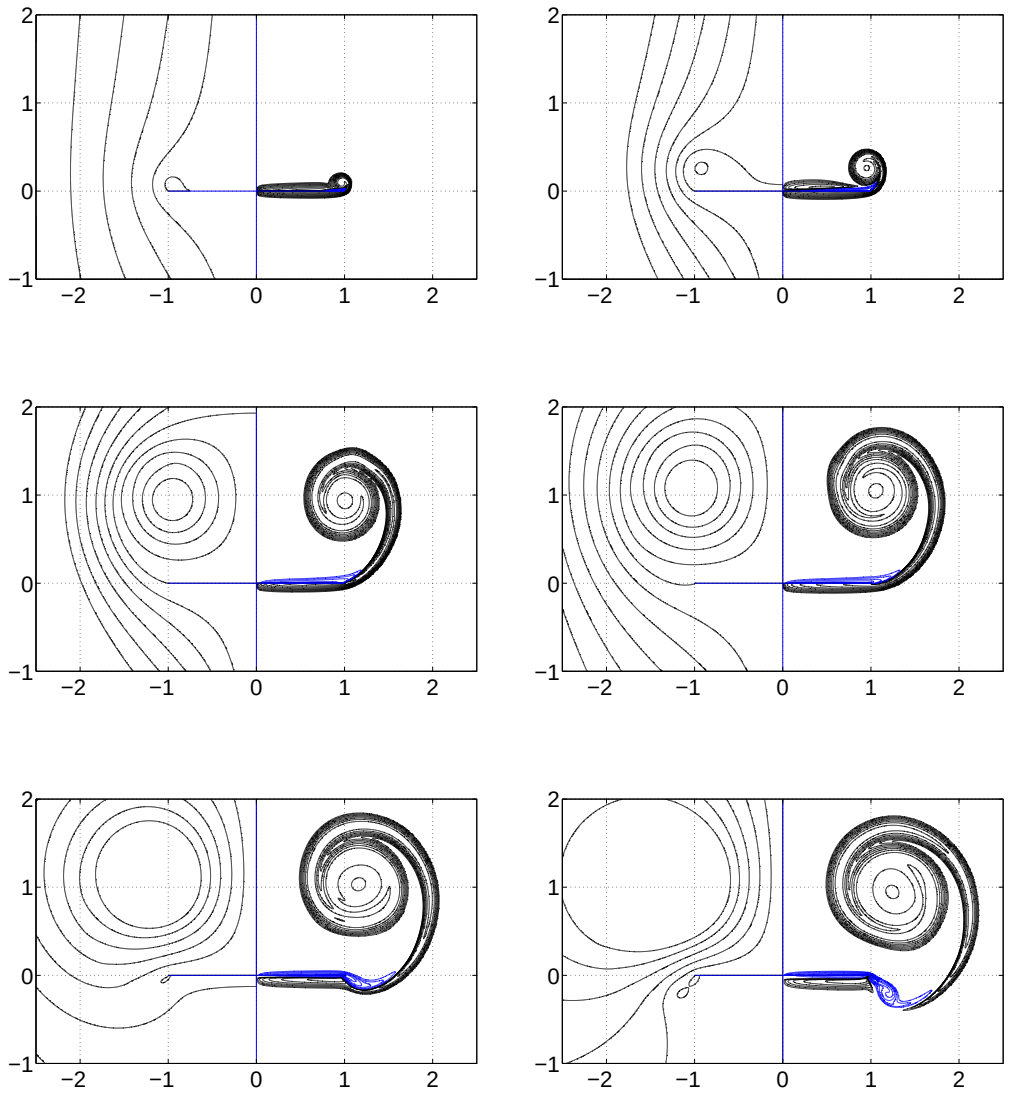

Figure 6.27: Vorticity contours and instantaneous streamlines for Re=2000 at t=0.5, 1, 2, 3, 3.5 and 3.8. The contour levels of the vorticity are $2^{[-5:10]}$ and $-2^{[1:8]}$ and the contour levels of the stream function are $[-1 : 0.2 : 1]$.

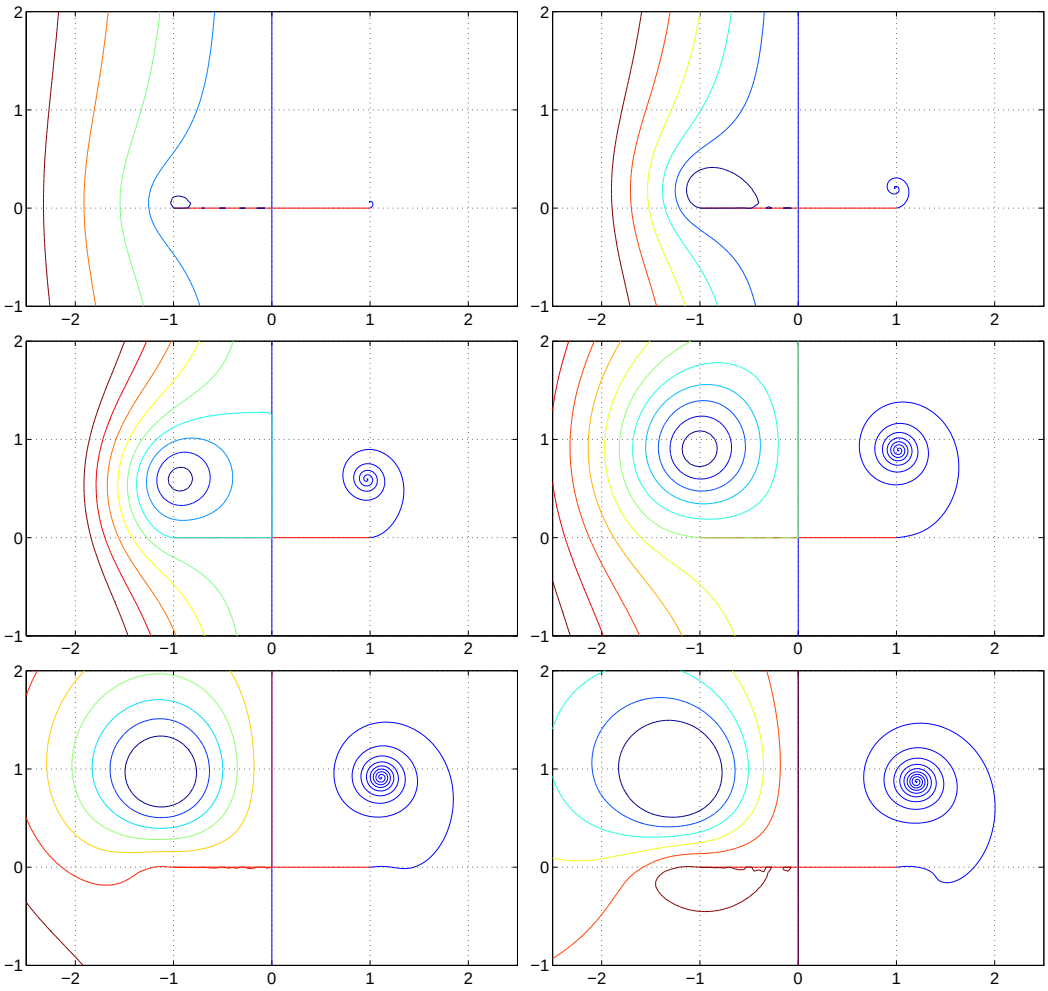

Figure 6.28: Locations of the vortex sheet and instantaneous streamlines for δ=0.1 at t=0.5, 1, 2, 3, 3.5 and 3.8, using vortex sheet method (all the results using vortex sheet method hereinafter are courtesy of Monika Nitsche). The contour levels of the stream function are $[-1 : 0.2 : 1]$.

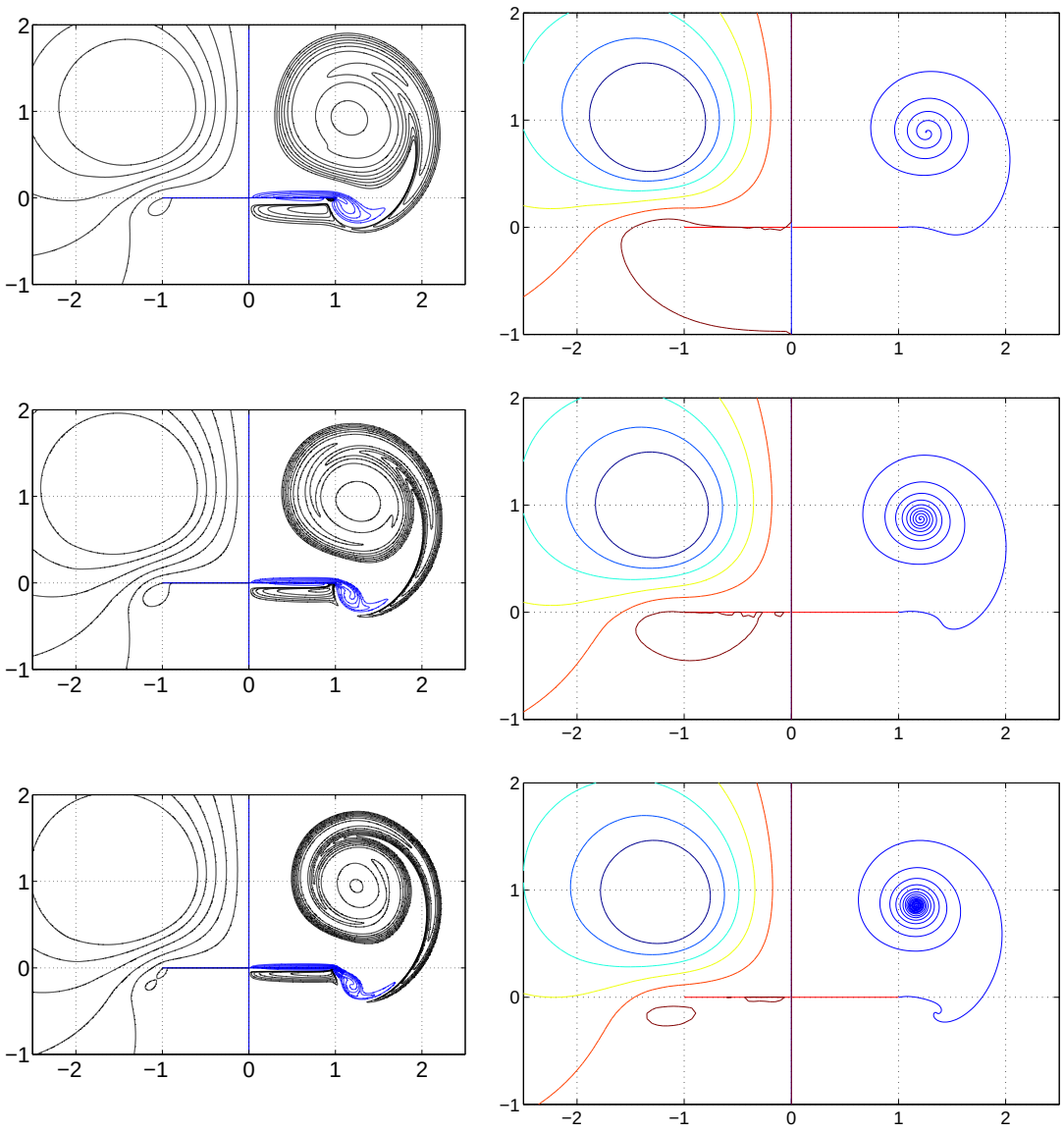

Figure 6.29: *Left column*: vorticity contours and instantaneous streamlines at $t = 3.8$. $Re = 500$, 1000 and 2000 (top to bottom), using FDMHS. The contour levels of the vorticity are $2^{[-5:10]}$ and $-2^{[1:8]}$. *Right column*: locations of the vortex sheet and instantaneous streamlines at $t = 3.8$ for $\delta = 0.2$, 0.1 and 0.05 (top to bottom), using vortex sheet method. The contour levels of the stream function are $[-1 : 0.2 : 1]$.

6.3.2 Instability

Instability is seen in the computational results for Re=4000. Figure 6.30 and figure 6.31 show the evolution of vorticity and stream function for Re = 4000. Instability occurs around t = 1.5 but it does vanish if I halve the mesh size. Therefore, it is the effect of the resolution.

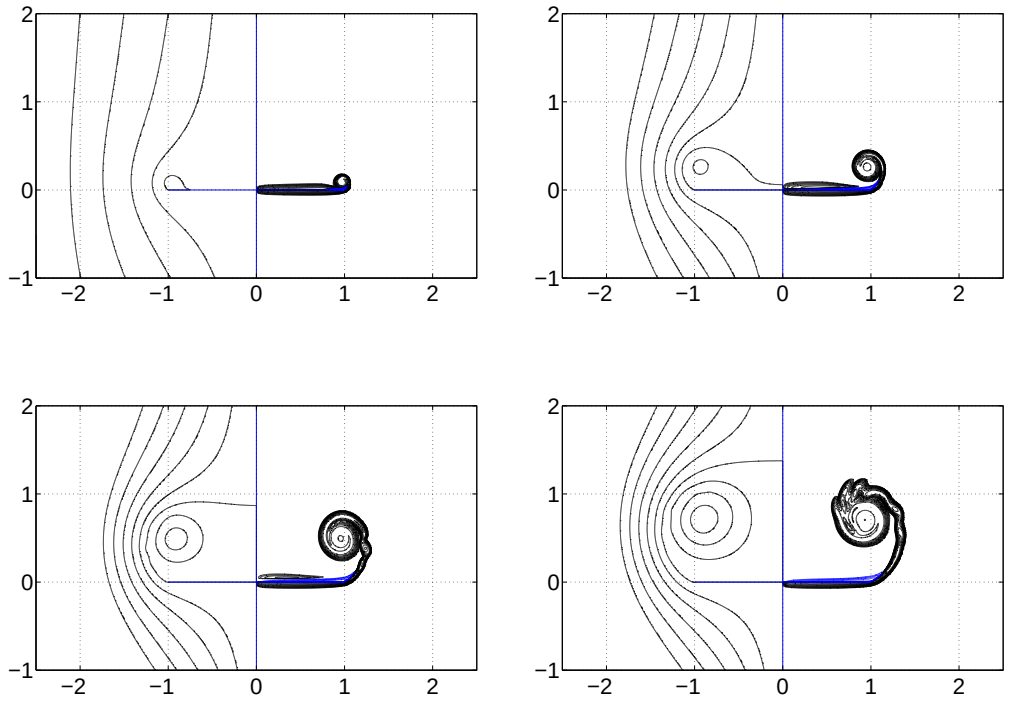

Figure 6.30: Vorticity contours and instantaneous streamlines for Re=4000 at t=0.5, 1, 1.5 and 2. The contour levels of the vorticity are $2^{[-5:10]}$ and $-2^{[1:8]}$. The contour levels of the stream function are = $[-1 : 0.2 : 1]$.

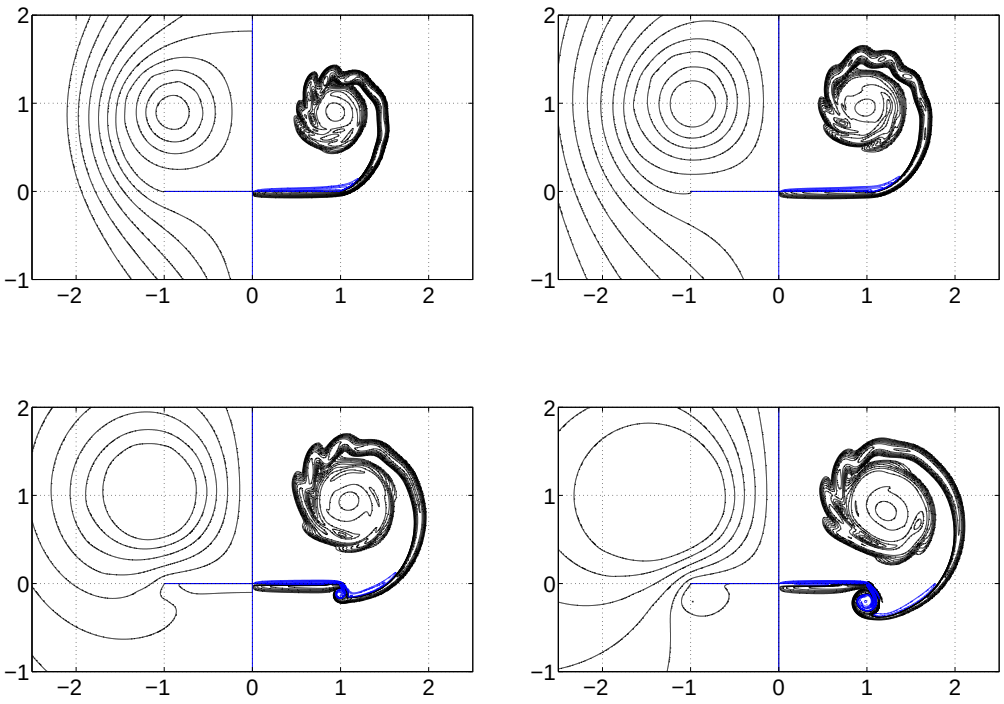

Figure 6.31: Continuation of figure 6.30. Vorticity contours and instantaneous streamlines for Re=4000 at t=2.5, 3, 3.5 and 3.8.

6.3.3 Vortex core

Table 6.4 shows the trajectory of the vortex core for Re=2000. In the x direction, the core moves back and forth from left to right. In the y direction, the core moves monotonically upwards for some time and then moves downwards. This is due to the deceleration of the background flow. The downward movement and the decrease in velocity do not happen at the same time, actually the downward movement has a time delay.

$Re = 2000$		
t	(x_c, y_c)	ω_c
0.1	(0.99, 0.01)	94.10
0.5	(0.96, 0.08)	50.03
1.0	(0.94, 0.25)	35.24
1.5	(0.95, 0.48)	28.92
2.0	(0.96, 0.72)	24.89
2.5	(0.93, 0.93)	22.02
3.0	(1.05, 1.04)	17.70
3.5	(1.25, 1.02)	11.38
3.8	(1.21, 0.95)	7.32

Table 6.4: The trajectory (xc, yc) and values ω_c of the vortex core for Re=2000.

6.3.4 Circulation

The circulation shed from the plate tip is calculated in a similar way to that in section 6.1, figure 6.17. A convergence study is performed first at $Re = 1000$ in figure 6.32. The figure plots Γ vs.t using two different mesh sizes of $h = 0.00625$ and 0.003125. One can see that Γ increases all the time until t=2.85, which is exactly 3/4 of the period KC. The maximum value of Γ is 6.39. After that, Γ starts to decrease. Values of Γ using these two mesh sizes agree pretty well everywhere though they are slightly different at t=3.8.

Figure 6.33 shows shed circulation Γ vs.t. Figure 6.33a is Γ vs. t using FDMHS for Re= 500, 1000 and 2000. $h = 0.003125$ for all computations, and $\Delta t = 4 \times 10^{-4}$, 2.5×10^{-4}, 2×10^{-4}, respectively. At an early time stage, the amount of circulation shed from the plate tip is close for all three Reynolds numbers. After $t = 2$, the differences in Γ start to show. More circulation is shed for larger Reynolds number. The maximum value of Γ for $Re = 2000$ is about 6.5, it is reached at $t = 2.9$. After that time Γ starts to decrease.

Figure 6.33b is Γ vs.t using the vortex sheet method for δ=0.2, 0.1 and 0.05. More circulation sheds from the tip for larger δ at early times ($t < 3$). The maximum value Γ for δ=0.05 is about 5.5, it is reached at $t = 2.8$. The difference between FDMHS and the vortex sheet method becomes more clear if you look at the circulation shedding rate, which is given below.

Figure 6.34 shows the circulation shedding rate $d\Gamma/dt$ vs. t. Figure 6.34a is $d\Gamma/dt$ vs. t using FDMHS for Re=500, 1000 and 2000. $d\Gamma/dt$ is computed using a second order central difference method in time. The general shape of the three curves is similar. $d\Gamma/dt$ increases fast initially with a extrema of 3.5 at t =1.3, then decreases. The curve of Re=2000 is relatively higher than the other two after t =1.3, this is consistent with a relative larger value in Γ for Re=2000 in figure 6.33a.

Figure 6.34b is $d\Gamma/dt$ vs.t using the vortex sheet method for δ=0.2, 0.1 and 0.05. The shedding rate past an initial time period depends little on δ. Initially, it varies with δ, but appears to converge to a curve in fairly good agreement with the viscous simulations. The maximum value of the shedding rate is slightly smaller than that in the viscous simulations. At larger time ($t > 2.5$), the values computed with the vortex sheet method decrease faster than in the viscous case. This remains to be studied further.

The viscous simulations using FDMHS show no difference in shed circulation

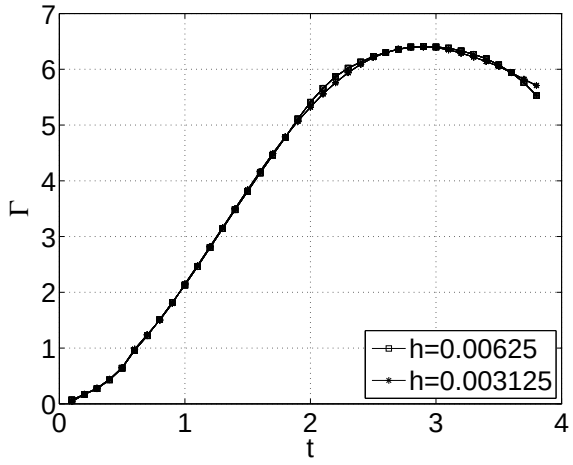

Figure 6.32: The circulation shed from plate tip Γ vs.t for Re = 1000. Two mesh sizes are used.

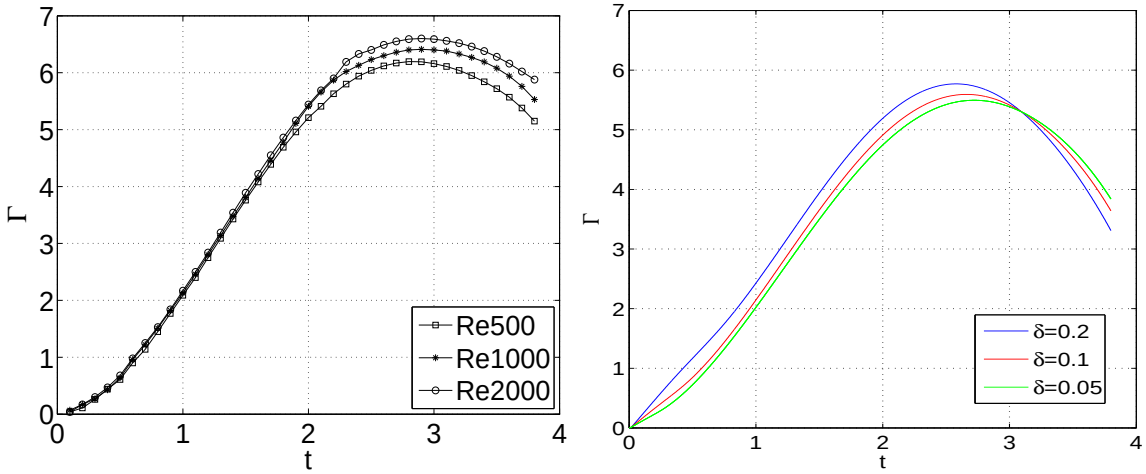

(a) (b)

Figure 6.33: The shed circulation Γ vs.t *(a)* using FDMHS for Re = 500, 1000 and 2000, and *(b)* using vortex sheet method for δ=0.2, 0.1 and 0.05.

and its rate for different Reynolds numbers at the early time stage. Therefore, one can see that the results are independent of viscosity, at least in the planar flow case. Furthermore, this conclusion also holds true for the cases of impulsively started flow and uniformly accelerated flow. The reason which causes the discrepancy in the axial symmetric case, observed by Nitsche and Krasny [31] might have something to do with the inner and outer approximations of the circulation shedding rate.

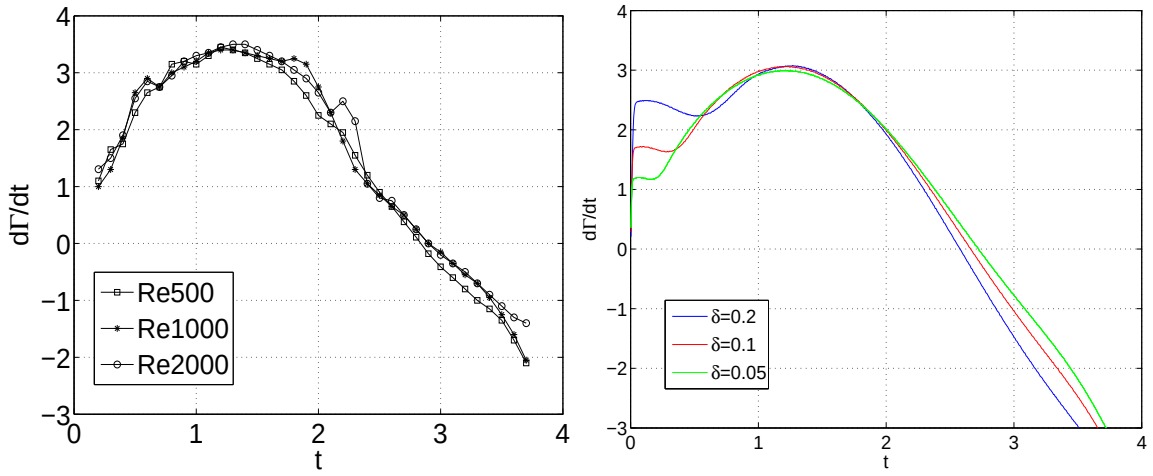

(a) (b)

Figure 6.34: The circulation shedding rate $d\Gamma/dt$ vs.t *(a)* using FDMHS for Re = 500, 1000 and 2000, and *(b)* using vortex sheet method for δ=0.2, 0.1 and 0.05.

6.3.5 Vortex width

The vortex width is defined in the same way as that in section 6.1. Figure 6.35 shows the vortex width Lvs.t for Re=1000. Three Ls are plotted, and they are determined by the contour lines of $\omega = 1$, $\omega = 0.1$ and $\omega = 0.01$. The width L is larger if one uses a contour line at a smaller level.

Figure 6.36 compare the vortex widths of FDMHS and the vortex sheet method. Figure 6.36a shows the width L vs.t for Re=500, 1000 and 2000, using FDMHS. The level of the contour line is $\omega = 1$. The width is larger at smaller Reynolds numbers since the diffusion is larger. The width is about 2.1 for Re=2000 at t=3.8. Figure 6.36b shows the vortex width at $\delta = 0.05$, 0.1 and 0.2, using the vortex sheet method. The width is larger for smaller values of δ. The width is also about 2.1 for δ=0.05 at t=3.8.

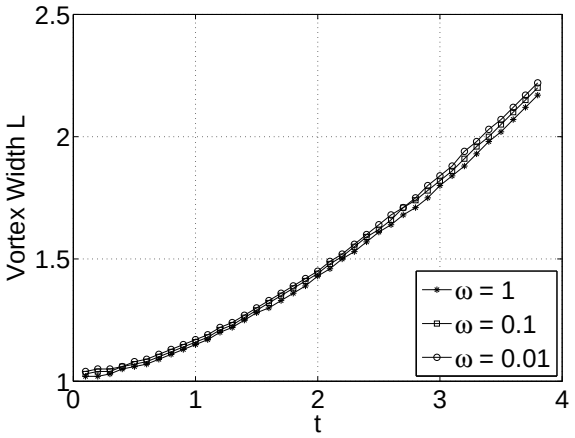

Figure 6.35: The vortex width L vs. t for $Re = 2000$. Three contour levels are chosen $\omega = 1$, 0.1 and 0.01.

6.3.6 Shear layer strength

Figure 6.37 shows the horizontal velocity u profiles along five lines, $x = 0$, $x = 0.5$, $x = 0.75$ and $x = 1$ at t=3.8. The Reynolds numbers are Re=500, 1000 and 2000. Remember that the plate tip is at $(1, 0)$ here. The horizontal velocity u is always zero on the plate, and it is below the plate when $y < 0$ while it is above the plate when $y > 0$. In general, the horizontal velocity changes sign across the plate. The horizontal velocity is both positive above and below the plate along the line $x = 1$. The largest gradient in u occurs near the plate, and u changes more rapidly as the

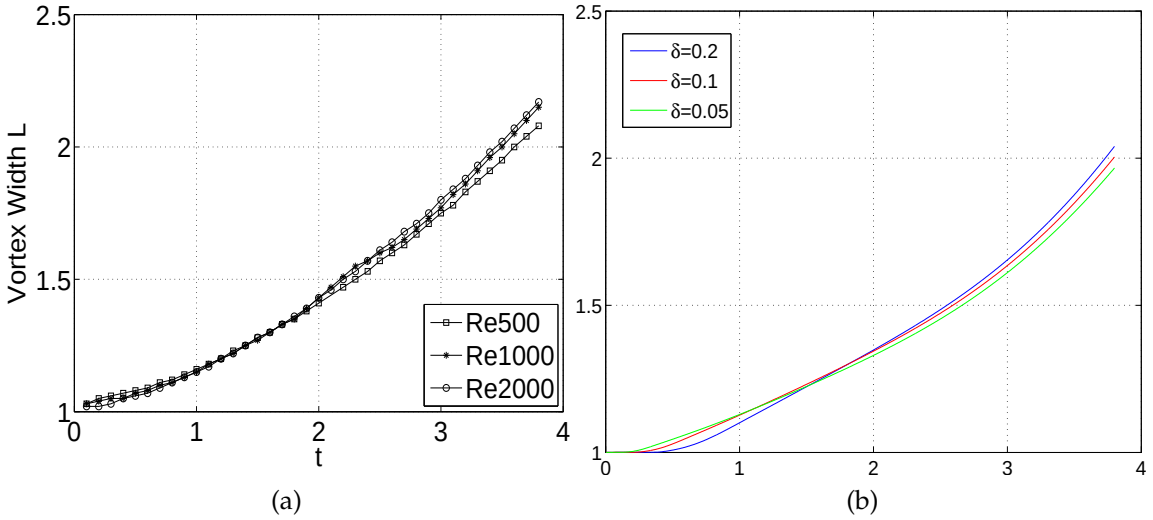

Figure 6.36: *(a)* The vortex width L ($\omega = 1$) vs.t for $Re = 500$, 1000 and 2000. *(b)* The vortex width L vs.t for $\delta = 0.05$, 0.1 and 0.2 using vortex sheet method.

Reynolds number gets large. The magnitude of u is bigger as the Reynolds number gets large as well.

One quantity of interest is the tangential velocity jump δu. Define the shear layer strength to be δu, and ultimately, we want to compare the shear layer strength with the sheet strength in the vortex sheet model. Figure 6.38 illustrates three scenarios to compute the δu. Figure 6.39 shows the evolution of the horizontal velocity u along five lines x=0, x=0.25, x=0.5, x=0.75 and x=1 for Re=2000. The five figures are snapshots at t=0.5, 1, 2, 3 and 3.5. The corresponding vorticity contours are in figure 6.27abcde. Find the first local extrema of the horizontal velocity u above and below the plate, respectively, then compute the difference in the value of u to yield the shear layer strength. Figure 6.40 shows the shear layer strength along the plate at the same five times t=0.5, 1, 2, 3 and 3.5. Just focus on the portion at $x \in [0, 0.8]$, the evolution of the shear strength is quite clear. The shear layer strength at $x \in [0.8, 1]$ is irregular because it is hard to determine δu there due to the effect of the starting vortex. The starting vortex is close to the tip and the horizontal velocity profiles look like spikes, therefore, my search algorithm does not pick the extremum that we want.

Table 6.5 gives the shear layer strength at three locations along $x \in [0, 1]$. The data is taken for Re=2000, t=3.8. The location of the first local extremum below the plate is *y below* while *y above* is the one above. Figure 6.41 shows the shear layer strength δuvs.x at t=3.8 for Re=500, 1000 and 2000. A total number of 320 locations

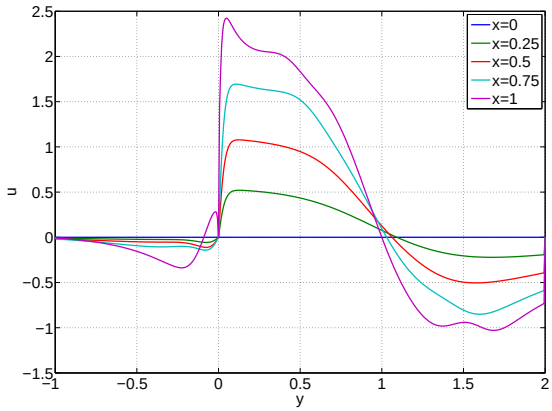

(a)

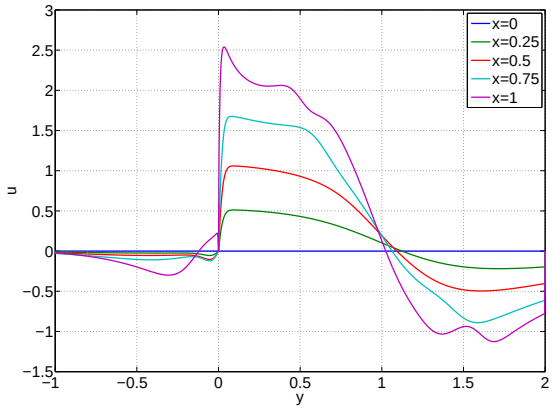

(b)

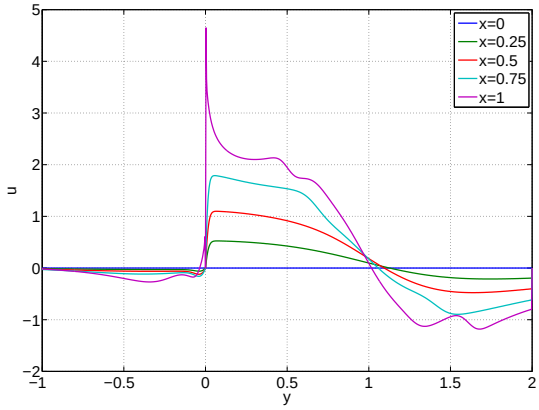

(c)

Figure 6.37: Plots of horizontal velocity u along five lines x=0, 0.25, 0.5, 0.75 and 1. t=3.8 and Re=500, 1000 and 2000.

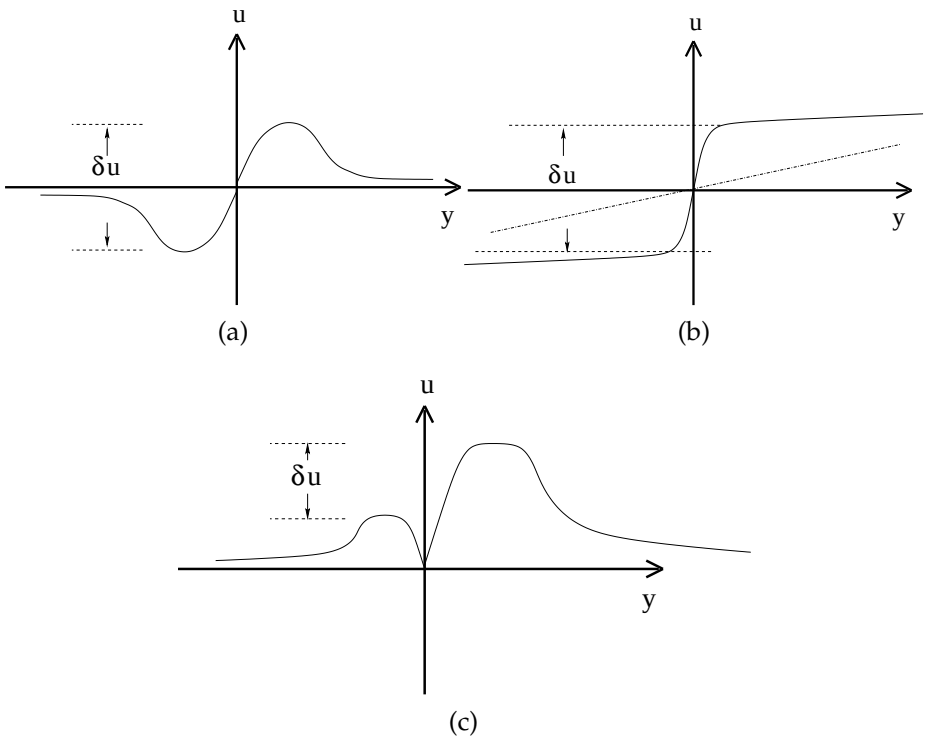

Figure 6.38: Three scenarios to compute the horizontal velocity jump δu due to (a) zero flow at infinity , (b) linear flow at infinity, and (c) u is of same sign across y=0.

on the plate are picked for each curve. The strength is generally linear, while it behaves non-linearly near the tip.

Figure 6.42 shows the vortex sheet strength σ along the plate at t=3.8 using vortex sheet method. Figure 6.42b is a closeup of figure 6.42a. The curves from bottom to top are for δ=0.05, 0.1 and 0.2, respectively. The vortex sheet strength seems be to linear for $x \leq 0.6$. All three curves shoot up near the x=1. The overall magnitude of the vortex sheet strength is smaller than that using FDMHS. However, it is not whether these quantities are comparable. In the viscous case, we are computing the an jump in the velocity at a finite distance from the plate, and it is not clear if this is an appropriate approximation of the vortex sheet strength.

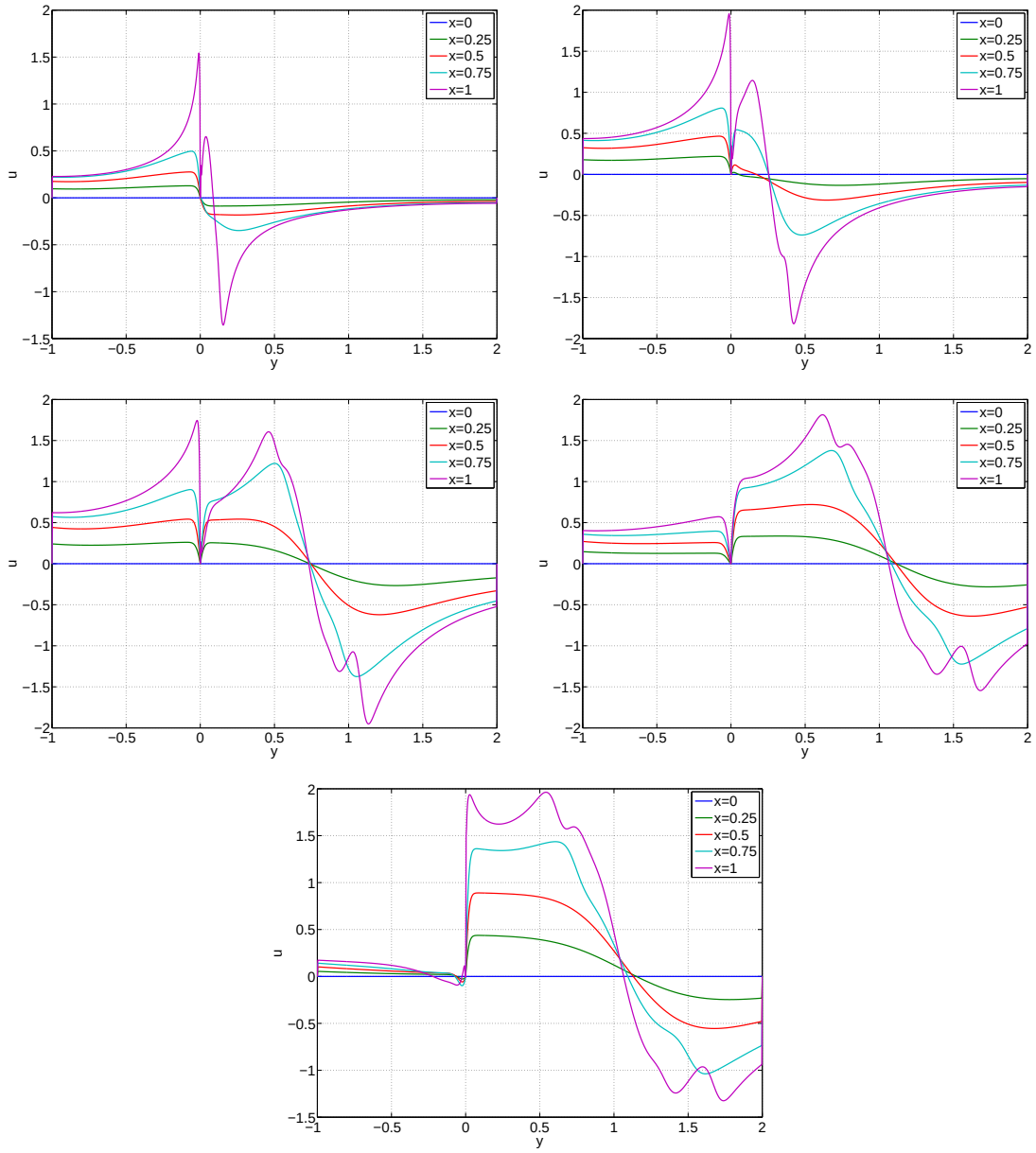

Figure 6.39: Plots of horizontal velocity u along five lines x=0, 0.25, 0.5, 0.75 and 1. t=0.5, 1, 2, 3 and 3.5, Re=2000.

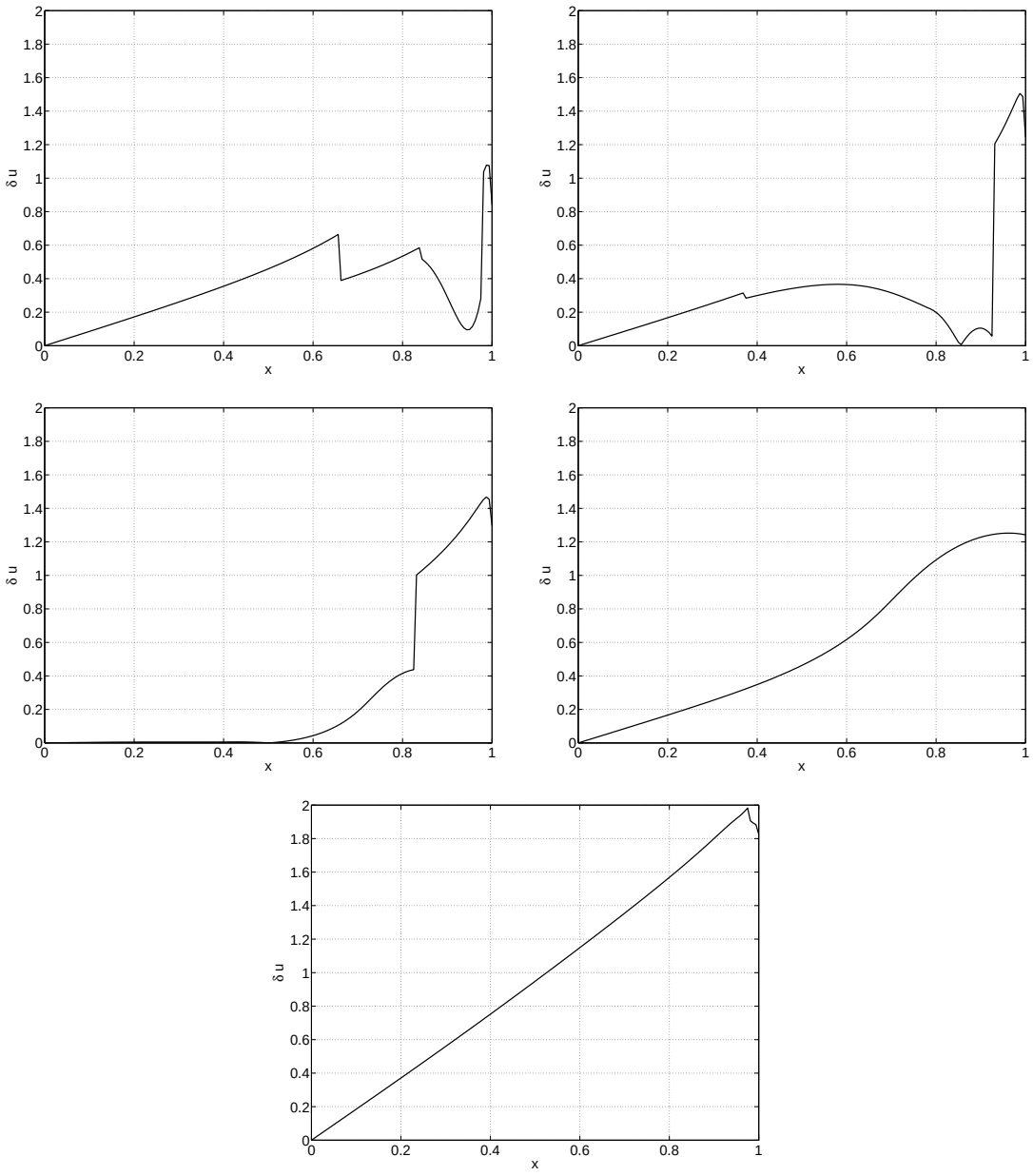

Figure 6.40: The shear layer strength δu along the plate for Re=2000 at t=0.5, 1, 2, 3 and 3.5.

Re = 2000, t = 3.8			
x	y below	y above	δu
0.25000	-0.05000	0.09688	0.56
0.75000	-0.05313	0.08125	1.79

Table 6.5: The shear layer strength δu and the coordinates of the local extrema of u above and below the plate. t=3.8 and Re=2000. The location of the first local extrema below the plate is referred to as *y below* while the one above is referred to as *y above*.

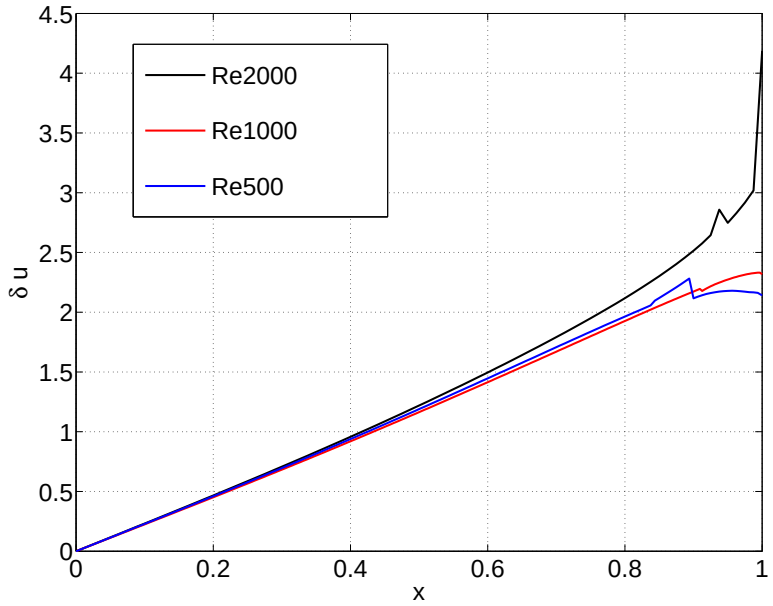

Figure 6.41: The shear layer strength δu along the plate for Re = 500, 1000 and 2000 at t=3.8.

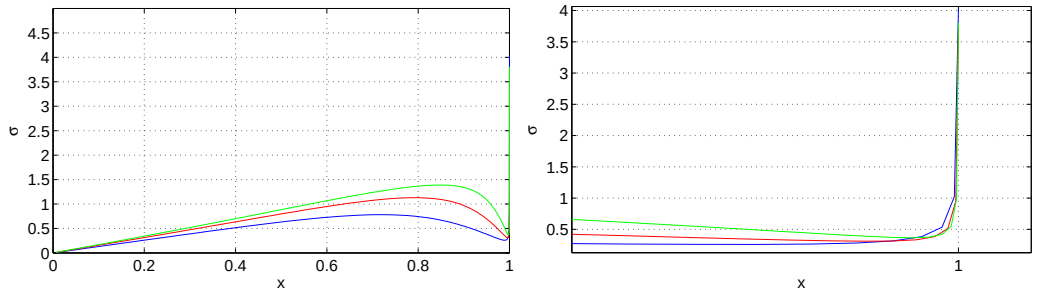

(a) (b)

Figure 6.42: *(a)* The vortex sheet strength σ along the plate at t=3.8 for δ=0.05, 0.1 and 0.2 using the vortex sheet method. *(b)* a closeup of *(a)* near the plate tip.

7 Viscous flow past a semi-infinite plate

Here we consider flow past a semi-infinite plate driven by the far field potential with the stream function in the form of

$$\psi_\infty(\mathbf{z}) = Ur^{1/2}\cos\left(\frac{\tan^{-1}(y/x)}{2}\right), \tag{7.1}$$

where $r = \sqrt{x^2+y^2}$, and $U = 1$. Because of the absence of the length scale, there exists a scaling rule which relates the length, time and the kinematic viscosity.

In the following, I will derive the scaling rule, and then verify the rule numerically. As for the previously considered flow, the flow is hard to resolve initially due the singularity at the tip, and the large velocity gradients within a thin boundary layer at an early stage of the evolution. Artificial small scales, or instability, would appear if the flow is under resolved. I will clarify the effects of under resolution by looking at a sequence of results based on different resolutions in time and space. The results apply to the finite plate case as well.

7.1 Derivation of the scaling rule

For the potential flow past a semi-infinite plate, a vortex sheet could be formulated as the semi-infinite plate being dissolved at $t = 0$. This vortex sheet is placed at $z = x + i0, \quad x \le 0$, with a complex potential W in the form of

$$W = \phi + i\psi = -iUz^{1/2} = -iUr^{1/2}e^{i\theta/2} \tag{7.2}$$

where ϕ is the velocity potential, ψ is the stream function, θ is the argument of the complex number $z = x+iy$ and $r = \sqrt{x^2+y^2}$. U is a real positive number indicating fluid velocity at a far field. Since the velocity potential is expressed as

$$\phi = U(x^2+y^2)^{1/4}\sin\left(\frac{\tan^{-1}\frac{y}{x}}{2}\right), \tag{7.3}$$

for the potential flow, and the velocity is defined as $\mathbf{u} = \langle u, v\rangle = \langle\frac{\partial\phi}{\partial x}, \frac{\partial\phi}{\partial y}\rangle = \langle -\frac{\partial\psi}{\partial y}, \frac{\partial\psi}{\partial x}\rangle$, the velocity on the plate is

$$\mathbf{u} = \nabla\phi = \pm U|x|^{1/2}, \quad y = \pm 0. \tag{7.4}$$

Note that **u** is discontinuous across the sheet. The bold line in figure 7.1 represents the vortex sheet, A' is the starting point of the closed loop around the tip while A is the ending point. The circulation Γ around this closed loop from A to A' is

$$\Gamma = \oint_A^{A'} \mathbf{u} \cdot ds = \phi(A') - \phi(A) \tag{7.5}$$

$$= 2U|x|^{1/2}. \tag{7.6}$$

Therefore, the circulation at the position $(x, 0)$ on the sheet is $2U|x|^{1/2}$, and the strength κ at $(x, 0)$ is $\kappa = U|x|^{-1/2}$. One would see that a singularity exists at the tip of the sheet. This does not violate the Helmholtz-Kevin laws, which is that the total circulation is zero along a closed loop fully immersed in the fluid, because the contour A to A' is not a closed loop lying entirely within the fluid but it intersects the plate.

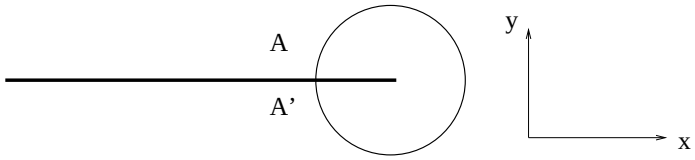

Figure 7.1

The initial condition of z is obtained by considering $\Gamma = 2U|x|^{1/2}$ or $\Gamma = 2U|z|^{1/2}$ since $y = 0$ on the sheet. Solving for z, one has

$$z(\Gamma, 0) = -\frac{1}{4}\Gamma^2/U^2. \tag{7.7}$$

It is equivalent to apply ψ_∞ at t=0. Denoting L to be a length scale, and T to be a time scale, introducing non-dimensional variables

$$x' = \frac{x}{L}, \quad [t'] = \frac{t}{T}, \quad \Gamma' = \Gamma\frac{T}{L^2}, \quad \omega' = \omega T, \quad \mathbf{u}' = \mathbf{u}T/L \tag{7.8}$$

(7.7) becomes

$$Lz' = -\frac{1}{4}\left(\frac{L^2\Gamma'}{T}\right)^2 \frac{1}{U^2} \tag{7.9}$$

$$z' = -\frac{1}{4}\frac{L^3}{T^2}\Gamma'^2\frac{1}{U^2}. \tag{7.10}$$

Similarly, the NSE (3.1) becomes

$$\text{(a)} \quad \frac{\partial\omega'}{\partial t'} + \mathbf{u}' \cdot \nabla\omega' = \frac{T}{L^2}\nu\nabla^2\omega', \quad \text{(b)} \quad \nabla^2\psi' = \omega', \quad \text{(c)} \quad \mathbf{u}' = \nabla^\perp\psi'. \tag{7.11}$$

Let U=1, and $L^3/T^2 = 1$, (7.11) becomes

$$\text{(a)} \quad \frac{\partial \omega^{'}}{\partial t^{'}} + \mathbf{u}^{'} \cdot \nabla \omega^{'} = \nu' \nabla^2 \omega^{'}, \quad \text{(b)} \quad \nabla^2 \psi^{'} = \omega^{'}, \quad \text{(c)} \quad \mathbf{u}' = \nabla^{\perp} \psi' \tag{7.12}$$

where

$$\nu^{'} = \nu T/L^2 = \nu T/T^{4/3} = \nu T^{-1/3}, \tag{7.13}$$

and (7.10) becomes

$$z' \quad = \quad -\frac{1}{4}\Gamma'^2. \tag{7.14}$$

The equation

$$L = T^{2/3}. \tag{7.15}$$

is the scaling rule, it indicates that solutions with ν at time t are the same as solutions with $\nu^{'}$ at time $t^{'}$ with a scale.

7.2 Numerical verification of the scaling rule

A baseline simulation of viscous flow past a semi-infinite plate is run at ν=0.01. The parameters that are used in the computation are given in table 7.1. Figure 7.2a is the vorticity contours at t=0.25 and this result is used to compare with that at other viscosities. A sequence of computations are run at $\nu' = 0.005, 0.0025, 0.002, 0.00125$ with a scaled time step, a mesh size and a domain, respectively. The corresponding scale in length and time at these viscosities are given in table 7.2. According to the scaling rule, it is believed that the vorticity at $t = 0.25$, $\nu = 0.01$ should be exactly the same as the vorticity at $t = 0.002$, ν=0.002 with a scale of $\frac{1}{T}$, where $T = 125$. The evidence is shown in figure 7.2b, which plots the vorticity contours at ν=0.002, t=0.002 with the values of vorticity scaled by T=125. One can see that figure 7.2ab are identical. The same comparisons is done at ν=0.005, 0.0025 and 0.00125, and their plots are not shown since they are the same as figure 7.2a.

ν	Δt	h	Domain	t
0.01	0.00025	0.003125	$[-3, 1.5] \times [-1, 2.5]$	0.25

Table 7.1: Parameters used in the computation for ν=0.01. The time step is Δt, the mesh size is h, and t is the terminal time.

ν'	$\frac{\nu}{\nu'}$	T	L	t'
0.005	2	8	2	0.3125
0.0025	4	64	4	0.00390625
0.002	5	125	16	0.002
0.00125	8	512	64	0.00048828125

Table 7.2: The scaling in time and length at ν = 0.005, 0.0025, 0.002 and 0.00125 based on ν=0.01. The time scale is T, a length scale is L, and t' is the terminal time.

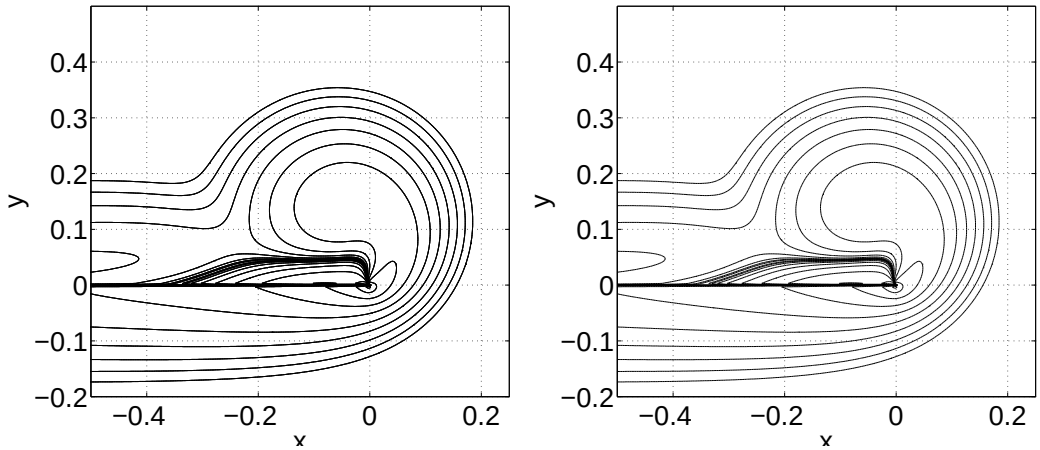

Figure 7.2: (a)Vorticity contours for ν=0.01 at t=0.25. (b) Scaled vorticity contours for ν=0.002 at t=0.002 in a scaled domain. The contour levels of the vorticity are $\pm 2^{[-2:8]}$.

Another quantity that I studied for the scaling rule verification is the trajectory of the vorticity centroid $(x_{\text{centroid}}, y_{\text{centroid}})$. The coordinates of the centroid are computed by

$$x_{\text{centroid}} = \int\int_{\Omega} \omega x d\mathbf{z} \tag{7.16}$$

$$y_{\text{centroid}} = \int\int_{\Omega} \omega y d\mathbf{z} \tag{7.17}$$

$$\tag{7.18}$$

where Ω is the whole computational domain. The predictions of the trajectories at ν=0.005, 0.0025, 0.002 and 0.00125 based on one computation at ν=0.01 are shown figure 7.3a. In this figure, only the centroid at ν=0.01 is numerically computed, and others are predictions. Figure 7.3b shows the verification. The actual centroids of ν=0.005, 0.0025, 0.002 and 0.00125 are plotted in cyan in figure 7.3b. The predictions and the the numerical results match exactly.

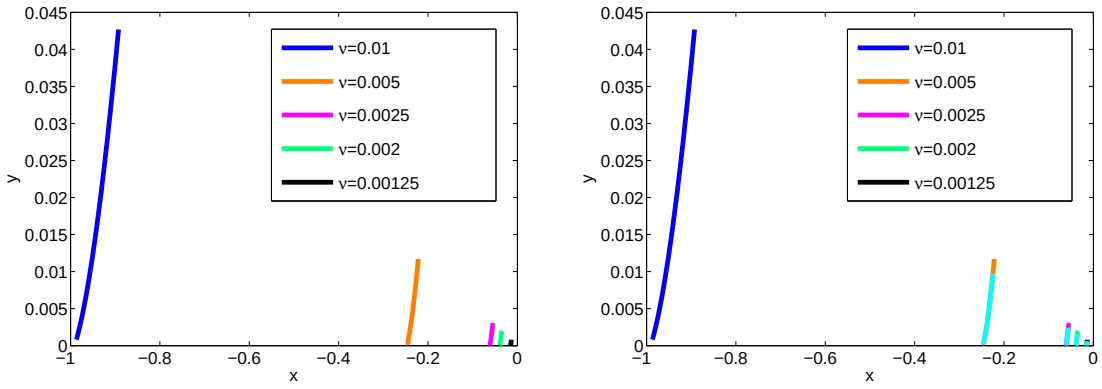

(a) (b)

Figure 7.3: (a) Predictions of the trajectories of the centroid for ν=0.005, 0.0025, 0.002 and 0.00125 based on one computation at ν=0.01. (b) The actual trajectories of the centroid at ν=0.005, 0.0025, 0.002 and 0.00125 based on the computations (cyan).

8 Summary

The main goal of this thesis was to use numerical simulatons to study a fundamental problem in fluid dynamics, namely, flow past sharp edges. Some experimental and numerical results are available in the literature, but much remains to be explored.

To that effect, a finite difference method of high order in space (FDMHS) has been developed to study the boundary layer separation at sharp edges of flat plates. The method solves the incompressible Navier-Stokes equations with constant density in a rectangular domain with a slit in place of the plate. It is also implemented to solve the driven cavity problem as a test case. The method uses a rectangular mesh and the time-dependent variables, velocity, stream function and vorticity, are evaluated at the grid points. Important features of FDMHS include the following. (a) FDMHS uses compact fourth order finite differences in space. (b) FDMHS is implicit in time, which is necessary because of the highly singular nature of the flow. (c) It is a splitting method which treats the convection with a semi-Lagrangian method, and the diffusion with a three-level Crank-Nicolson scheme of fourth order in space. The three-level method was found to be more stable than a corresponding two-level method. (d) FDMHS is fourth order in space and first order in time in the driven cavity problem with a smooth top lid velocity. FDMHS is between first and second order in space in the problem of impulsively started flow past a finite plate. Evidence that FDMHS is an improvement over a second order finite difference method has been shown. FDMHS also shows agreement with EC4 [8] in the driven cavity problem. (e) FDMHS is parallelized using the MPI interface, and shows good performance in strong and weak scalability on the multi-cluster platform available to me.

This method has been implemented to simulate the flow induced by a finite plate moving in direction normal to itself, and the flow past a semi-infinite plate. In the finite plate case, three plate velocities are considered: impulsively started, uniformly accelerated, and oscillating. We show that FDMHS resolves the detailed structure of the flow. The main results of the simulation are the following, all of which add to what is currently known about this basic flow.

(a) We resolve the boundary layer separation and roll-up from very early times to relatively large times, $t \in [0.00025, 5]$.

(b) We resolve details of the vorticity structure in the boundary layer at early times that have not been studied before, in particular.

(i) The region of negative vorticity along the plate induced by and entrained into the leading vortex is resolved. It forms immediately after the flow starts. The evolution of its height and length, and the vorticity along and across the plate, are recorded.

(ii) A secondary entrainment of positive vorticity into the region of negative vorticity was found. It is small and does not grow much.

(iii) For the impulsively started finite plate case, the maximum velocity, which is initially unbounded, is found to decay as $t^{-1/4}$ over a large initial time interval.

(c) We resolve flow quantities such as the vortex core trajectory and vorticity, vortex size, circulation and circulation shedding rate, and find the apparent scaling behavior for the circulation.

(d) The effect of viscosity on the vorticity evolution and on quantities such as the shed circulation from the plate tip, core trajectory, vortex width are presented. In particular, the shed circulation Γ is independent of viscosity initially for all three far field flows

(e) In the uniformly accelerated case, we show the evolution in the appropriate non-dimensional variables, and find agreement with scaling laws observed experimentally.

(f) We resolve flow past oscillating plate and compare with vortex sheet results. For the planar case considered here, the circulation and the circulation shedding rate at early times are in excellent agreement. There are difference at later times most likely caused by wall vorticity which is not accounted for by the vortex sheet model.

The problem of flow past a semi-infinite plate is still on-going. In the thesis, the derivation of the scaling rule is presented which establishes the dependence of the solution on the viscosity and time. The scaling rule is verified numerically in terms of the vortex centroid trajectory and contours of vorticity. In future, I will compute the flow of ν=0.002 to a time t=128, and the result will be used to investigate the flow behavior at other viscosities.

The vortex sheet model for boundary layer separation used in section 6.3 approximates the circulation shed from each side of the edge separately. Further work regarding the applicability of this model must include computing these quantities in the viscous case. Furthermore, the present computations need to be extended

to axisymmetric flow to better evaluate axisymmetric vortex sheet models. Axisymmetric separation is also quite interesting in itself, as it commonly occurs, for example in bio-locomotion and in engineering technology.

Finally, we intend to broaden this work and apply it to wedges with finite nonzero angles.

Appendix

I Satisfying the far field velocity

Here we present the construction of the vortex sheet that induces the far field velocity U_∞ for the problem of flow past a finite plate. The vortex sheet is discrete and approximated by a set of point vortices. The stream function and the vertical velocity induced by a point vortex with a strength κ are

$$\psi(\mathbf{z}) = -\frac{\kappa}{2\pi}\log|\mathbf{z}-\mathbf{z}_o|, \quad v(\mathbf{z}) = -\frac{\kappa}{2\pi}\frac{(x-x_o)}{(x-x_o)^2+(y-y_o)^2} \tag{8.1}$$

where $\mathbf{z}_o$ is the location of the point vortex and $\mathbf{z}$ is where ψ and v are evaluated. The vortex sheet overlaps the finite plate. , and due to the symmetry, only half sheet is considered. Point vortices on the vortex sheet have Chebyshev positions on the sheet

$$x_k = \cos(k\Delta\alpha), \quad y_k = 0, \quad k = 0, 1, \cdots, n. \tag{8.2}$$

where $\Delta\alpha = \pi/2n$ and n is the number of point vortices assigned. A set of test points is also established at the Chebyshev middle positions, see Figure 8.1.

$$x_k^{\text{test}} = \cos(k\Delta\alpha + \frac{\Delta\alpha}{2}), \quad y_k^{\text{test}} = 0, \quad k = 0, \cdots, n. \tag{8.3}$$

Remember that the background flow is $v = U_\infty = 1$, therefore, the vertical velocity

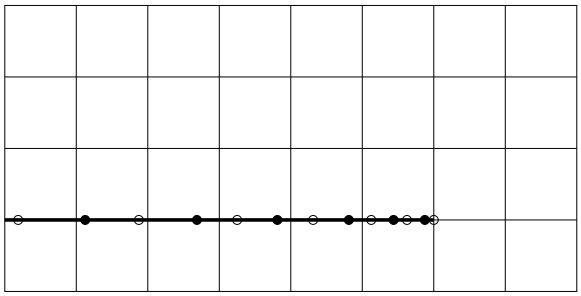

Figure 8.1: Location of point vortices and test points on half of the vortex sheet. Solid line: vortex sheet, white dots: point vortices, dark dots: test points.

at each test point is

$$v_j = -\frac{1}{2\pi}\sum_k \left[\frac{\kappa_k}{2\pi}\frac{x_j^{\text{test}}-x_k}{(x_j^{\text{test}}-x_k)^2+(y_j^{\text{test}}-y_k)^2} - \frac{\kappa_k}{2\pi}\frac{x_j^{\text{test}}+x_k}{(x_j^{\text{test}}+x_k)^2+(y_j^{\text{test}}-y_k)^2}\right] + U_\infty \tag{8.4}$$

where $j = 0, \cdots, n$. The formulation contains contributions from point vortices and the background flow. The second term in the square bracket is the vertical velocity induced by the other half of the vortex sheet. The vortex sheet mimics the finite plate and therefore, all v_j=0. Solving for the strength of the discrete vortex sheet κ_k by setting (8.4) equals zero, one can compute the far field stream function by

$$\psi_\infty(\mathbf{z}) = -\frac{1}{2\pi} \sum_k \kappa_k \log |\mathbf{z} - \mathbf{z}_k|. \tag{8.5}$$

References

[1] S. Alben, 2010, Regularizing a vortex sheet near a separation point, *J. Comput. Phys.*, **229**, 879-9071.

[2] S. Alben, 2010, Passive and active bodies in vortex-street wakes, *J. Fluid Mech.* **642**, 92-125.

[3] S. Alben and M. Shelley, 2005, Coherent locomotion as an attracting state for a free flapping body, *PNAS*, **102**, 11163-11166.

[4] J. T. Beale, A. Majda, 1982, Vortex methods II: higher order accuracy in two and three dimensions, *Math. Comput.* **39**, 29-52.

[5] A. J. Chorin. 1989, Computational fluid mechanics: selected papers, *Academic Press, INC.*.

[6] L. Cortelezzi and A. Leonard, 1993, Point vortex model of the undsteady separated flow past a semi-infinted plate with transverse motion, *Fluid Dyn. Res.* , **11**, 264-295.

[7] P. Degond, S. Mas-Gallic, 1989, The weighted particle method for convection-diffusion equations,Part 1: The case of an isotropic viscosity *Math. Comp.*, **53**, 485-507.

[8] W. E. J. G. Liu, 1996, Essentially compact schemes for unsteady viscous incompressible flows, *J. Comput. Phys.*, **126**, 122-138.

[9] W. E. J. G. Liu, 1996, Vorticity boundary condition and related issues for finite difference schemes, *J. Comput. Phys.*, **124**, 368-382.

[10] J. D. Eldredge, 2005, Efficient tools for the simulation of flapping wing flows, *AIAA* **2005-0085**, 1-11.

[11] J. D. Eldredge, 2007, Numerical simulation of the fluid dynamics of 2D rigid body motion with the vortex particle method, *J. Comput. Phys.*, **221**, 626-648.

[12] J. D. Eldredge and C. Wang, 2010 High-fidelity simulations and low-order modeling of a rapidly pitching plate, *AIAA*, **2010-4281**, 1-19.

[13] M. Falcone, R. Ferretti 1998, Convergence analysis for a class of high-order semi-Lagrangian advection schemes, *J. NUMER. ANAL.* **35**(3) 909-940.

[14] C. A. J. Fletcher, 1991, Computational techniques for fluid dynamics, Vol.1, *Springer*

[15] V. Frayssé, L. Giraud, S. Gratton, and J. Langou, July 2007, *A Set of GMRES Routines for Real and Complex Arithmetics on High Performance Computers*, CERFACS Technical Report TR/PA/03/3.

[16] J. D. Hudson, Dennis, S. C. R. , 1985, The flow pf a viscous incompressible fluid past a normal flat plate at low and intermediate Reynolds numbers: the wake, *J.Fluid Mech*, **160**, 369-383.

[17] H. E. Johnston, 1999, Efficient computation of viscous incompressible flow, *thesis*,

[18] M. Jones, 2003, The separated flow of an inviscid fluid around a moving flat plate, *J. Fluid Mech.*, **496**, 405-441.

[19] M. A. Jones and M. J. Shelley, 2005, Falling cards, *J. Fluid Mech.*, **540**, 393-425.

[20] S. Kern and P. Koumoutsakos, 2006, Simulations of optimized anguilliform swimming, *J. Exp. Biology*, **209**, 4841-4857.

[21] P. Koumoutsakos, 2005, Multiscale flow simulations using particles, *Ann. Rev. Fluid Mech.*, **37**, 457-487.

[22] P. Koumoutsakos, A. Leonaro, 1995, High Resolution simulations of the flow around an impulsively started cylinder using vortex methods, *J.Fluid Mech*, **296**, 1-38.

[23] P. Koumoutsakos, D. Shiels, 1996, Simulation of the viscous flow normal to an impulsively started and uniformly accelerated flat plate, *J.Fluid Mech*, **328**, 177-277.

[24] P. Koumoutsakos, A. Leonard, F. Pepin, 1994, Boundary conditions for viscous vortex methods, *J.Comput. Phys*, **113**, 52-61.

[25] R. Krasny, 1986, A study of singularity formation in a vortex sheet by the point vortex approximation, *J.Fluid Mech*, **167**, 65-93.

[26] R. Krasny, 1988, A vortex-dipole sheet model for a wake, *Phys.Fluids*, **31**, 173-175.

[27] R. Krasny, 1989, Desingularization of periodic vortex sheet roll-up, *J. Comput. Phys.* **65**, 292-313.

[28] Q. X. Lian, Z. Huang, 1989, Starting flow and structure of the starting vortex behind bluff bodies with sharp edges, *Exp Fluids*, **8**, 95-103.

[29] P. Luchini, R. Tognaccini, 2002, The Start-up vortex issuing from a semi-infinite flat plate, *J.Fluid Mech*, **455**, 175-193.

[30] S. Michelin and S. G. Llewellyn Smith, 2009, An unsteady point vortex method for coupled fluid-solid problems, *Theor. Comput.Fluid Dyn.*, **23**, 127-153.

[31] M. Nitsche, R. Krasny, 1994, A numerical study of vortex ring formation at the edge of a circular tube, *J. Fluid Mech*, **276** 139-161.

[32] M. Nitsche, 1996, Scaling properties of vortex ring formation at a circular tube opening, *Phys. Fluids*, **8** 1848-1855.

[33] M. Nitsche, M. A. Taylor, R. Krasny, 2003, *Computational Fluid and Solid Mechanics*, Computational Fluid and Solid Mechanics 2003, K. J. Bathe (Editor).

[34] D. Pierce, 1961, Photographic evidence of the formation and growth of vorticity behind plates accelerated from rest in still air, *J. Fluid Mech.*, **11**, 460-464.

[35] D. I. Pullin, 1978, The large-scale structure of unsteady self-similar rolled-up vortex sheets, *J. Fluid Mech*, **88**, 401-430.

[36] D. I. Pullin, A. E. Perry, 1980, Some flow visualization experiments on the starting vortex, *J. Fluid Mech*, **97**, 239-255.

[37] D. I. Pullin and Z. J. Wang, 2004, Unsteady forces on an accelerating plate and appli-cations to hovering insect flight, *J. Fluid Mech.*, **509**, 1-21.

[38] P. G. Saffman, 1992, Vortex Dynamics, *Cambridge University Press*.

[39] M. Seaid, 2002, Semi-Lagrangian integration schemes for viscous incompressible flows, *CMAM*, **2**, 392-409.

[40] M. Shelley and S. Alben, 2008, Flapping States of a Flag in an Inviscid Fluid: Bistability and the Transition to Chaos, *Phys. Rev. Lett.*, 074301.

[41] R. K. Shukla, J. D. Eldredge, 2007, An inviscid model for vortex shedding from a deforming body, *Theor. Comput. Fluid Dyn.*, **21**, 343-368.

[42] A. Staniforth, J. Cote, 1991, Semi-Lagrangian integration schemes for atmospheric models-a review, *Monthly Weather Review*, **119**, 2206-2223.

[43] J. C. Strikwerda, 1989, Finite difference schemes and partial differential equations, *Wadsworth & Brooks/Coles*.

[44] S. Taneda, H. Honji, 1971, Unsteady flow past a flat plate normal to the direction of motion, *Journal of the Physical Society of Japan*, **30**, 262-272.

[45] C. Temperton, A. Staniforth, 1987, An efficient two-time-level semi-Lagrangian semi-implicit integration scheme, *Quart. J. Roy. Meteor. Soc.* , **113**, 1025-1039.

[46] G. Tryggvason, W. J. A. Dahm and K. Sbeih, 1991, Fine Structure of Vortex Sheet Rollup by Viscous and Inviscid Simulation, *Journal of fluids engineering*, **113**, 31-36.

[47] Z. J. Wang, J. G. Liu, S. Childress, 1999, Connection between corner vortices and shear layer instability in flow past an ellipse, *Phys.Fluids*, **11**, 2446-2448.

[48] A. Ysasi, E. Kanso, and P. K. Newton, 2011, Wake structure of a deformable Joukowski airfoil, *Fluid Dynamics: From Theory to Experiment*, **240**, 1574-1582.

[49] Z. J. Wang, 2000, Vortex shedding and frequency selection in flapping flight, *J. Fluid Mech.*, **410**, 323-341.

[50] Z. J. Wang, 2000, Two-dimensional mechanism for insect hovering, *Phys. Rev. Lett.*, **85**, 2216-2219.